

The electron cyclotron maser

K. R. Chu*

Department of Physics, National Tsing Hua University, Hsinchu 300, Taiwan

(Published 4 May 2004)

The electron cyclotron maser (ECM) is based on a stimulated cyclotron emission process involving energetic electrons in gyration motion. It constitutes a cornerstone of relativistic electronics, a discipline that has emerged from our understanding and utilization of relativistic effects for the generation of coherent radiation from free electrons. Over a span of four decades, the ECM has undergone a remarkably successful evolution from basic research to device implementation while continuously being enriched by new physical insights. By delivering unprecedented power levels, ECM-based devices have occupied a unique position in the millimeter and submillimeter regions of the electromagnetic spectrum, and find use in numerous applications such as fusion plasma heating, advanced radars, industrial processing, materials characterization, particle acceleration, and tracking of space objects. This article presents a comprehensive review of the fundamental principles of the ECM and their embodiment in practical devices.

CONTENTS

I. Introduction	490	A. Relativistic dispersion relation of right-hand circularly polarized waves	507
A. Bunching and synchronism	490	B. Dispersive properties and growth rate	508
B. Significance of cyclotron interactions	491	C. Physical interpretation	508
C. Discovery of the electron cyclotron maser	492	D. Criterion for mechanism identification	509
D. Physics of cyclotron interactions and article outline	492	E. An experimental verification	510
II. Electron Cyclotron Interactions—Basic Theory	493	F. Phase bunching and spatial bunching	510
A. Basic model	493	G. Related plasma instabilities	511
B. Effective cyclotron phase angle	494	H. Summary and discussion	511
C. Graphic representation	494	V. The Electron Cyclotron Maser as a Coherent Radiation Source	511
D. Azimuthal and axial bunching—A qualitative discussion	495	A. Gyrotron modeling	512
1. Azimuthal bunching	495	B. The gyrotron traveling-wave amplifier	512
2. Axial bunching	496	1. Principle of operation—Convective instability	512
E. Linear analysis	496	2. Backward-wave oscillations—Absolute instability	513
1. Equations of motion	496	3. Status and applications	514
2. Linear solutions	497	C. The gyrokystron amplifier	515
3. Energy-transfer mechanisms	497	1. Principle of operation—Ballistic bunching and distributed interaction	515
4. Cyclotron emission and absorption	499	2. A design example	515
a. Short time scale	500	3. Status and applications	516
b. Synchronous time scale	500	D. The gyromonotron oscillator	516
c. Long time scale	501	1. Principle of operation—Reflective feedback	516
F. Nonlinear behavior	501	2. Power balance, oscillation threshold, and equilibrium field	517
1. Normalized equations	501	3. Status and applications	518
2. Nonlinear interaction	501	E. The gyrotron backward-wave oscillator	519
3. Saturated efficiency and its limitations	502	1. Principle of operation—Internal feedback	519
G. Harmonic interaction	504	2. Axial modes of the gyro-BWO	519
1. Harmonic fields	504	3. Nonlinear properties	520
2. Physical interpretation and significance of harmonic interaction	504	4. Status and applications	520
3. Optimum conditions for harmonic interaction	505	F. Efficiency considerations	520
H. Summary and discussion	505	G. Summary and discussion	521
III. Early Fast-Wave Experiments	506	VI. Gyrotron Traveling-Wave Amplifier—A Study of Mode Competition	521
A. Survey of early fast-wave experiments	506	A. Sources of self-oscillations in the gyro-TWT	521
B. Summary and discussion	507	B. Competition between convective and absolute instabilities	521
IV. The Electron Cyclotron Maser as a Plasma Instability	507	C. Simulation analysis and physical interpretation	523
		D. Stabilization of reflective oscillations and absolute instabilities	525
		1. Stabilization with a sever	525
		2. Stabilization with distributed wall losses	525

*Electronic address: krchu@phys.nthu.edu.tw

E. An ultrahigh-gain scheme	526
F. Harmonic multiplying amplification	527
G. Summary and discussion	527
VII. Nonlinear Field Contraction in Backward-Wave Oscillations	528
A. Modeling of backward-wave oscillations	528
B. Nonlinear field contraction	528
C. Summary and discussion	529
VIII. Nonstationary Oscillations	530
A. Single-mode nonstationary behavior	530
B. Experimental observations	531
C. Theoretical interpretation	533
D. Time-dependent simulation of the gyro-BWO	533
E. Summary and discussion	534
Acknowledgments	534
References	535

I. INTRODUCTION

The field of vacuum electronics deals with the use of streaming electrons in a vacuum for the generation of electromagnetic radiation. The advent of microwave tubes in the 1930s and 1940s represented a milestone of far-reaching consequences in the long history of vacuum electronics. Magnetrons, klystrons, and traveling-wave tubes (TWT's) are among the familiar members of the microwave tube family that better our lives as well as influence the outcomes of wars and the advancement of science. They are a long way from the glass radio and TV tubes of the past. Microwave tubes developed for radar during World War II have, for example, found wide-ranging applications in fundamental physics research (Forman, 1995), including, most notably, the particle accelerator. At the same time, the quest for still greater powers and higher frequencies continues to stimulate dramatic advances in the field. Modern vacuum-electronics research features a strong emphasis on novel mechanisms based on relativistic effects (Granatstein, Parker, and Armstrong, 1999). The electron cyclotron maser and free-electron laser are two prominent examples in this category commonly referred to as relativistic electronics.

The microwave band nominally extends from 0.3 to 300 GHz (wavelengths of 1 m down to 1 mm in free space). The performance of early gridded tubes degraded sharply at microwave frequencies, principally because of the transit-time limitation associated with the gridded structure. In order to maintain a unidirectional energy transfer, an electron must complete its traversal through the space between grids before the wave electric field reverses its direction. By comparison, microwave tubes employ metallic interaction structures of complex shapes. By confining the electromagnetic fields (also referred to as the *rf fields*) within or around such structures, it is possible to control the phase velocity and field profile through appropriate tailoring of the structure. This in turn brings about a variety of mechanisms (and hence devices) by which the electrons transfer energy to the rf fields at higher frequencies. On the one hand, the phase velocity of the wave can be slowed down to synchronize with the electron motion, as in the

TWT and in the magnetron. On the other hand, the rf electric field can be made to concentrate around a narrow gap within the cavity (Slater, 1950, p. 232), as in the klystron, thereby substantially reducing the effective electron transit time. Thus the spectrum of high-power electromagnetic radiation was extended deep into the microwave band up to the borderline of millimeter wavelengths.

Traditionally, microwaves at frequencies above the upper reaches of the classical tubes are referred to as millimeter waves. Modern technologies have long enabled these tubes to cross the millimeter-wave boundary. However, the complex rf structure responsible for the dramatic increase in centimeter-wave power levels also imposes severe limitations with regard to physical size and output power as one further pushes up the frequency. Consequently, new approaches are required for the realization of powerful sources in the millimeter-wave region and beyond.

This review addresses the physics of the electron cyclotron maser (ECM) interaction and the continued, and equally significant, advance of the power spectrum into the millimeter- and submillimeter-wave regions made possible by the interaction. In essence, a new dimension in the interaction mechanism—cyclotron resonance—provides the physics underpinning and permits wave generation in simple and large-size structures.

Sections I–V are intended for readers with little prior knowledge of the subject, while the other sections treat more specialized topics. This section begins with a discussion of the physical conditions for wave generation in vacuum-electronic devices, the significance of cyclotron interactions, and the discovery of the electron cyclotron maser. Topics to be covered in the remainder of the article are outlined at the end of Sec. I. The Gaussian system of units is employed throughout.

A. Bunching and synchronism

Generation of electromagnetic radiation by a dc electron beam requires a bunching mechanism to impart an ac component to the beam current. In order for the bunches to build up, and to allow sustained energy transfer, the electrons must remain in close synchronism with the wave. Bunching and synchronism are two fundamental conditions for the generation of coherent radiation in vacuum-electronic devices. Indeed, different classes of devices are distinguishable by their characteristic bunching and synchronism mechanisms. The history, operating principles, and current development trends of a broad range of vacuum-electronic devices can be found in the review articles of Granatstein, Parker, and Armstrong (1999) and Luhmann, Nusinovich, and Goebel (2004).

Radiation generation in vacuum-electronic devices is a *stimulated* process because electron bunching is caused by the action of an electromagnetic wave. For purposes of illustration and later reference, we first consider the conventional traveling-wave tube (TWT) amplifier commonly employed in radar and communication systems.

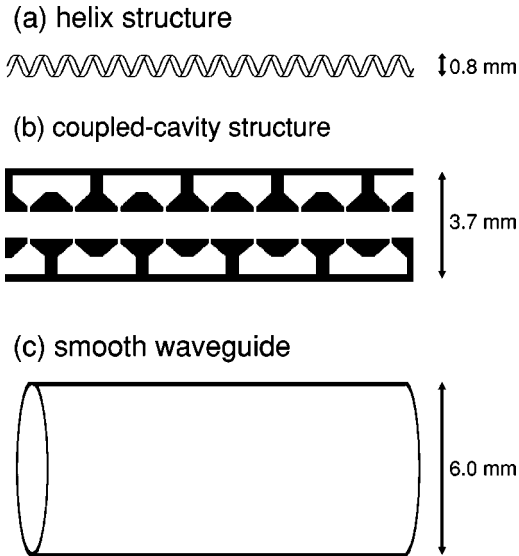


FIG. 1. Comparison of the shapes and transverse dimensions of three types of interaction structures: (a) a helix traveling-wave tube (TWT) structure; (b) a coupled-cavity TWT structure; and (c) a smooth waveguide, all at the operating frequency of 30 GHz in the lowest-order mode. From Chu, 2002.

The TWT is a linear beam device (see, for example, Gilmour, 1986, Chap. 10), in which the electrons move rectilinearly along the axis of a periodic structure [Figs. 1(a) and (b)]. By Floquet's theorem, a normal mode of the periodic structure (also called the circuit wave) can be decomposed into an infinite number of traveling-wave components, each having the same frequency ω but a different propagation constant k_z given by $k_z = \beta_0 + 2\pi n/L$, where β_0 is a constant, L is the period of the structure, and n is an arbitrary integer (Slater, 1950, Chap. 8; Gewartowski and Watson, 1965, Chap. 8). Slow waves ($\omega/k_z < c$) are thus formed because most of the components will have a sufficiently large k_z . Synchronism requires that the electrons, at velocity v_z , travel approximately at the phase velocity of a specific component of the circuit wave,

$$\omega - k_z v_z \cong 0, \quad (1)$$

so that they are acted upon by a quasistatic electric field. Over the distance of every guide wavelength, half of the electrons are accelerated and the other half decelerated. In the process, electron bunches are formed. As shown in Fig. 2(a), the electrons tend to bunch toward a field null, which still does not lead to a net energy transfer. In actual operation, however, the electron beam enters the circuit at a velocity slightly greater than the phase velocity of the synchronized component. Moving slightly faster than the wave, centers of electron bunches will gradually advance into the decelerating phases while the bunches are being formed [Fig. 2(b)]. This results in a net transfer of the beam energy to the wave. A static magnetic field is commonly present in the TWT but exists only to prevent the electrons from radially dispersing under the repulsive electrostatic forces.

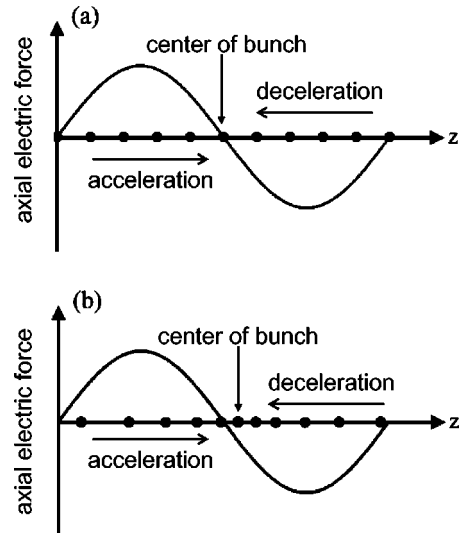


FIG. 2. Bunching of a dc electron beam in the TWT by the axial electric field of a synchronized traveling-wave component, plotted in the reference frame moving with the wave at its phase velocity: (a) Initially, the electric forces bunch the electrons about a field null; (b) since the average electron velocity is slightly greater than the phase velocity, the center of the bunch gradually advances into the decelerating phase of the wave, while the bunch is being formed: This results in a net energy transfer to the wave.

B. Significance of cyclotron interactions

Condition (1) indicates that only a slow wave can participate in the synchronous beam-wave interaction. Slow waves in a periodic structure tend to concentrate around the periodic loading (see Figs. 8.7-2 and 8.7-5 in Gewartowski and Watson, 1965). When the interaction space diminishes at short wavelengths, the structural complexity and surface field concentration present fabrication difficulties as well as power-handling problems, such as wall heating and voltage breakdown. By comparison, the interaction space for optical radiation by lasers is not restricted in size. However, an atom upon each excitation emits only a single photon of the desired energy. This accounts for the decreasing power output of lasers with decreasing photon energy, so that lasers are most often employed in the infrared and shorter-wavelength region. Such opposing limitations of classical and quantum-mechanical sources result in the long-recognized millimeter and submillimeter “gap” (Fig. 3) in the electromagnetic spectrum where the achievable power falls to low levels from both the long- and short-wavelength regions.

The very reasons for the power gap suggest the need for a radiation mechanism that combines the advantages of multiple photon emission of the free electron and the multiwavelength interaction space of the laser. Electron cyclotron interactions provide the solution. When the interaction involves the gyration of electrons in a static magnetic field B_0 , synchronism requires (see Sec. II.A)

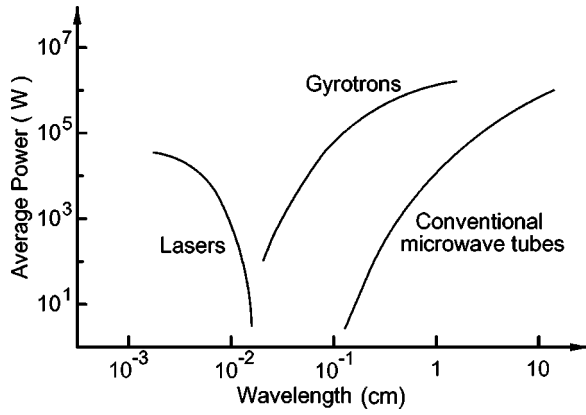


FIG. 3. Average power capabilities of lasers, conventional microwave tubes, and gyrotrons.

$$\omega - k_z v_z - \frac{\Omega_e}{\gamma} \cong 0, \quad (2)$$

where $\Omega_e (= eB_0/m_e c)$, a positive quantity, is the rest-mass (m_e) electron cyclotron frequency and γ is the relativistic factor of the electron. We have explicitly expressed the γ dependence of the electron cyclotron frequency because it plays the central role in cyclotron interactions.

Condition (2) is qualitatively different from condition (1) in two important respects. First, it permits a simple fast-wave ($\omega/k_z > c$) interaction structure, such as a smooth waveguide, in which the rf fields peak away from the wall. In addition, the electrons now possess an inherent frequency, Ω_e/γ . A high-order mode may therefore be resonantly excited in a manner analogous to high-order mode excitation by photons in the laser resonator. Thus the structural simplicity, the distributed rf fields, and particularly the over-moded interaction space have afforded cyclotron-resonance devices the capability to close the power gap in the region of millimeter and sub-millimeter waves (Fig. 3).

Figure 1 compares the shapes and transverse dimensions of three interaction structures: a helix structure, a coupled-cavity structure, and a smooth waveguide, all at the operating frequency of 30 GHz in the lowest-order mode. The high-power capability of the smooth waveguide [Fig. 1(c)] is evident in this figure. It has both greater structural simplicity and greater transverse dimension than those of the slow-wave structures [Figs. 1(a) and (b)]. The possibility of high-order mode excitation provides additional interaction space of even greater significance. Fast waves have been generated in cavities in such high-order modes (Felch *et al.*, 1999) that, when scaled to 30 GHz, the cross-sectional areas are three orders of magnitude greater than that shown in Fig. 1(c).

The advantages of cyclotron interactions, however, come with the requirement of a relatively high static magnetic field. For example, in the millimeter-wave region (30–300 GHz), the required magnetic-field strength ranges from 11 to 110 kG. This requirement can be alleviated by operating at a harmonic cyclotron frequency.

Harmonic interactions and the additional advantages (and limitations) that accrue from their utilization will be discussed in Sec. II.G.

C. Discovery of the electron cyclotron maser

For fast-wave generation, a new bunching mechanism is required, and in order to maintain synchronism it must involve the cyclotron motion. However, until most of the slow-wave tube types had been invented and successfully implemented, fast-wave devices were not part of the mainstream tube activities. Then, in the late 1950s, fast-wave emission mechanisms were discovered almost simultaneously by Twiss (1958), Gaponov (1959a, 1959b), and Schneider (1959) in theory and by Pantell (1959) in experiment. These discoveries sparked research and development activities that continue unabated even after four decades and that have resulted in the most successful fast-wave device to date—the gyrotron.

The radiation mechanisms proposed by the above-mentioned authors fall into two basic types: relativistic and nonrelativistic. The relativistic mechanism was analyzed both classically (Twiss, 1958; Gaponov, 1959a, 1959b) and quantum mechanically (Schneider, 1959). In the classical picture, it is due to azimuthal phase bunching by rf electric forces, which modulate the electron cyclotron frequency. This is inherently a relativistic effect since the rest-mass cyclotron frequency is independent of the electron energy. The nonrelativistic mechanism, by contrast, originates from axial phase bunching by rf magnetic forces. As will be extensively discussed in Secs. II–IV, both mechanisms are present in cyclotron interactions, and each dominates in a different regime of the phase velocity. The name “electron cyclotron maser” commonly refers to fast-wave generation, for which the relativistic mechanism plays the dominant role.

D. Physics of cyclotron interactions and article outline

The basic physics, although not the entire picture, of electron bunching in linear beam devices can be described by a one-dimensional model; however, it is complicated by the inevitable ac space-charge effects (Gewartowski and Watson, 1965, Chaps. 9 and 10). In dramatic contrast, bunching in cyclotron interactions takes place in both azimuthal and axial phase angles with the electrons in three-dimensional motion, but it exhibits much reduced, if any, ac space-charge effects.

New physics issues arise from the increased complexity of the physical mechanisms, the multidimensionality of phase and real spaces, and the relativistic nature of electron dynamics. The first portion of this review, Secs. II–IV, addresses the fundamental physics of electron cyclotron interactions with a circularly polarized electromagnetic wave. In Sec. II, we study a basic model consisting of a ring of uniformly distributed electrons circulating in a static magnetic field. Driven by the rf forces, azimuthal and axial phase bunching are shown to be intimately related in the emission process. There are

also two absorption mechanisms, important on the short time scale and at low electron energies, that transfer the wave energy to the electrons. Interestingly, the two emission mechanisms are inseparable and mutually competitive, whereas the two absorption mechanisms act in concert independently. These emission and absorption processes are analyzed linearly and nonlinearly in Sec. II, followed by an examination of the harmonic interaction.

Early observations of stimulated cyclotron emission in fast-wave structures are discussed in Sec. III, where uncertainties regarding the interpretation of the observed emission are noted. A plasma-physics treatment in Sec. IV provides the definitive clarification. It is shown that azimuthal and axial bunching each drive a different instability in the plasma medium, with one serving as a debunching mechanism to the other in either instability. Azimuthal bunching is established to be the driving mechanism for stimulated cyclotron emission in fast-wave structures.

Another basic issue considered in Sec. IV is the relationship between phase bunching and spatial bunching. Self-consistent solutions indicate that phase bunching, whether azimuthal or axial, results in complete cancellation of ac space charges in a uniform electron medium. Furthermore, axial bunching is not accompanied by any axial current. These rather surprising consequences underline the basic differences between linear beam and cyclotron-resonance interactions.

The second portion of the review, Secs. V–VIII, addresses the embodiment of the ECM instability in practical devices for the generation of high-power coherent radiation. Such devices, under the general name of gyrotron, assume a number of forms. The configurations, operating principles, status, and applications of four basic types of gyrotrons are discussed in Sec. V. Sections VI–VIII address important nonlinear effects in both amplifier and oscillator configurations. With the electrons simultaneously in resonance with a multitude of modes, an amplifier can readily break into oscillations. Section VI examines the competition between the forward-wave amplification and the backward-wave oscillation. Investigation of this and other types of oscillations and methods for their stabilization leads to the demonstration of an ultrahigh-gain scheme. The principle of harmonic multiplying amplification in multistage structures is also discussed.

Section VII examines nonlinear ECM interactions in oscillators. Backward-wave oscillations build up in an internal feedback loop and are characterized by highly current-sensitive field profiles. The rf fields contract nonlinearly, which results in sharply contrasting linear and nonlinear behavior. Implications of this effect are further examined in Sec. VIII, where nonstationary oscillations in resonant and nonresonant structures are compared. As the beam current increases, cavity oscillations transition from the stationary state to a sequence of self-modulation states, and eventually they turn stochastic. By contrast, backward-wave oscillations in the waveguide remain stable at a beam current far in excess

of the conventional nonstationary threshold. This fundamental difference is physically interpreted in terms of the field-shaping processes in these two types of oscillations.

There are also critical technologies that must be, and to a large extent have been, developed for high average-power operation, such as electron guns, depressed collectors, mode converters, and microwave windows. However, these topics are beyond the purview of the current article. Readers are referred to Felch *et al.* (1999) and Thumm and Kasperek (2002) for an extensive review of the requisite technology development.

II. ELECTRON CYCLOTRON INTERACTIONS—BASIC THEORY

Cyclotron-resonance devices employ an electron beam consisting of helically moving electrons with free energy residing in the gyration motion. Energy transfer is effected through electron interactions with the transverse electric field. This brings into play the transverse motion of electrons and hence the cyclotron resonance. In this section, we examine the fundamental processes through a model incorporating only the essential elements of cyclotron interactions.

A. Basic model

There are a number of different, but equivalent, ways of representing electrons with random cyclotron phase angles. We adopt the model shown in real space in Fig. 4(a). In the presence of a static magnetic field B_0 oriented along the positive z axis, an ensemble of electrons with identical axial and transverse velocities are uniformly distributed in a common cyclotron orbit in the $z=0$ plane. Velocity-space representation of the ensemble is shown in Fig. 4(b). An electron with velocity polar angle ϕ in Fig. 4(b) corresponds to the electron with position polar angle $\theta = \phi - \pi/2$ in Fig. 4(a).

Initially, the electrons are rotating about the origin in both spaces, and either θ or ϕ represents the cyclotron phase angle. As the electron orbits are perturbed by the rf fields, centers of rotation will spread radially from the origin in real space. The polar angle θ , in reference to the origin, no longer represents the exact cyclotron phase angle. However, ϕ always specifies the orientation of the transverse velocity and hence the exact cyclotron phase angle. Consequently, subsequent dynamical behavior will be illustrated in velocity space only.

The electrons are assumed to be in the presence of a constant-amplitude, circularly polarized electromagnetic wave propagating in the positive or negative z direction. The rf fields \mathbf{E}_\perp and \mathbf{B}_\perp are given by

$$\mathbf{E}_\perp = E_0[\cos(\omega t - k_z z)\mathbf{e}_x + \sin(\omega t - k_z z)\mathbf{e}_y], \quad (3)$$

$$\mathbf{B}_\perp = \frac{k_z c}{\omega} \mathbf{e}_z \times \mathbf{E}_\perp = \frac{k_z c}{\omega} E_0[-\sin(\omega t - k_z z)\mathbf{e}_x + \cos(\omega t - k_z z)\mathbf{e}_y], \quad (4)$$

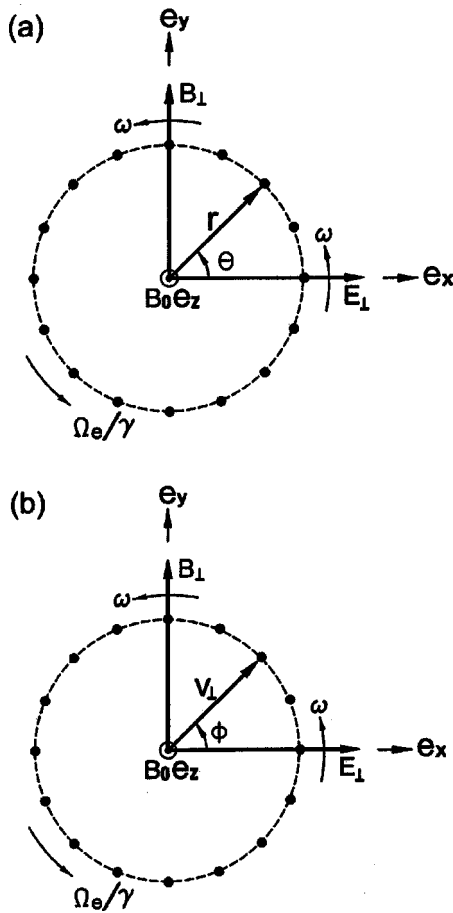


FIG. 4. Model of electron cyclotron interactions with a circularly polarized electromagnetic wave (E_{\perp} and B_{\perp}): (a) initial distribution of an ensemble of electrons gyrating about the z axis under the influence of a uniform magnetic field $B_0 e_z$; (b) the same model represented in the velocity space. In both figures, e_x , e_y , and e_z are fixed unit vectors in the laboratory frame in which the electrons and the rf fields rotate at the frequency of Ω_e/γ and ω , respectively.

where E_0 is the field amplitude and e_x , e_y , and e_z are fixed unit vectors in the laboratory frame. The wave frequency ω is assumed to be positive. The rf fields, illustrated in Fig. 4 at $t=z=0$ for a positive k_z , are transversely uniform in any cross-sectional plane. The fields rotate as a whole, with the amplitude unchanged, both in time (in any fixed cross-sectional plane) and along the z axis (at any fixed time). For the study of cyclotron interactions, it is convenient to define the wave polarization with respect to the direction of the static magnetic field B_0 . For B_0 aligned along the positive z direction, the wave represented by Eqs. (3) and (4) is right-hand circularly polarized, rotating in the same sense as the electrons, regardless of the sign of k_z .

The principal quantity of interest is the rate of change of the electron kinetic energy $W[(\gamma-1)m_e c^2]$,

$$\frac{d}{dt}W = -e\mathbf{v}_{\perp} \cdot \mathbf{E}_{\perp}. \tag{5}$$

Substituting Eq. (3) for \mathbf{E}_{\perp} and writing $\mathbf{v}_{\perp} = v_{\perp}(\cos\phi e_x + \sin\phi e_y)$, we obtain

$$\frac{d}{dt}W = -eE_0 v_{\perp} \cos(\omega t - k_z z - \phi). \tag{6}$$

The rf magnetic field is much smaller than the static magnetic field under conditions of practical interest. Thus ϕ advances at approximately the electron cyclotron frequency,

$$\frac{d\phi}{dt} \cong \frac{\Omega_e}{\gamma}. \tag{7}$$

Resonance takes place when the electron remains in phase with the wave. This requires

$$\frac{d}{dt}(\omega t - k_z z - \phi) \cong \omega - k_z v_z - \frac{\Omega_e}{\gamma} \cong 0. \tag{8}$$

Equation (8) reproduces the synchronism condition in Eq. (2). A left-hand circularly polarized wave, if present, would rotate in the opposite sense from the electron and thus would play a negligible role. It would merely add a rapid and small-amplitude fluctuation to the electron energy.

B. Effective cyclotron phase angle

In Eq. (6), there are three phase angles (ωt , $k_z z$, and ϕ), which determine the rate of change of the electron energy. The last two angles may be regarded as electron phase angles because they depend upon the electron coordinates z and ϕ . These two phase angles are indistinguishable in that only their algebraic sum enters into Eq. (6). We may therefore define an effective cyclotron phase angle ϕ_{eff} as

$$\phi_{\text{eff}} = k_z z + \phi, \tag{9}$$

and rewrite Eq. (6) as

$$\frac{d}{dt}W = -eE_0 v_{\perp} \cos(\omega t - \phi_{\text{eff}}). \tag{10}$$

The effective cyclotron phase angle advances at the rate of the effective cyclotron frequency Ω_{eff} , given by

$$\Omega_{\text{eff}} = \frac{d}{dt}\phi_{\text{eff}} \cong k_z v_z + \frac{\Omega_e}{\gamma}. \tag{11}$$

With all of the phase information of the electron included in ϕ_{eff} , the synchronism condition is now represented by

$$\omega \cong \Omega_{\text{eff}}. \tag{12}$$

The effective cyclotron phase angle will provide a convenient framework for the graphic representation and physical interpretation of the two-phase-angle interaction processes under consideration.

C. Graphic representation

Since the electrons and the wave are phase synchronized, resonant interactions can in principle be represented in a quasistationary plot, as in the one-dimensional example shown in Fig. 2. However, there

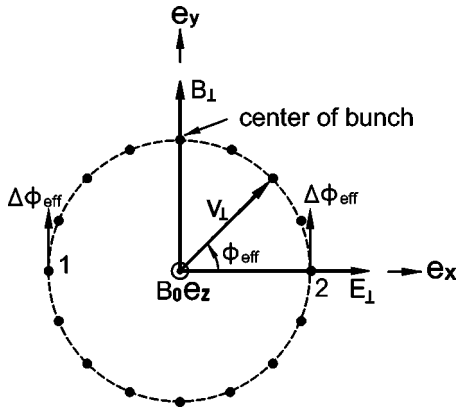


FIG. 5. Bunching in the effective cyclotron phase space due to rf electric forces. Electrons on the left half-circle ($\mathbf{v}_\perp \cdot \mathbf{E}_\perp < 0$) gain energy, while those on the right half-circle ($\mathbf{v}_\perp \cdot \mathbf{E}_\perp > 0$) lose energy. The increased relativistic mass of electrons on the left results in decreased $\Omega_{\text{eff}} (=k_z v_z + \Omega_e/\gamma)$, whereas decreased relativistic mass of electrons on the right results in an increase in Ω_{eff} . Hence the electrons tend to form a bunch by moving toward the point marked as “center of bunch.”

are two difficulties in representing cyclotron-resonance interactions in Figs. 4(a) and (b), which exhibit only the cyclotron phase angle. First, under the synchronism condition ($\omega \cong \Omega_{\text{eff}}$), the rotating frequency of the wave and the gyrating frequency of electrons differ by approximately $k_z v_z$, a difference that can be significant. Second, and more serious, phase variations due to the axial motion of the electrons cannot be represented. The cyclotron phase angle alone does not correctly represent the relative orientation of the electron velocity vector and the rf field vectors.

These difficulties are removed by displaying the electrons in the effective cyclotron phase space (Figs. 5 and 6), in which the polar angle is designated to be the effective cyclotron phase angle. The effective cyclotron phase space is readily constructed by adding $k_z z$ to the phase angle ϕ in Fig. 4(b), with other quantities unchanged. Each electron now rotates at its effective cyclotron frequency Ω_{eff} . This results in near co-rotation of the electron with the wave when $\omega \cong \Omega_{\text{eff}}$. In addition, the electron velocity vector is now correctly oriented relative to the rf field vectors. Note that only the Ω_e/γ portion of Ω_{eff} represents the actual cyclotron rotation frequency. The $k_z v_z$ portion is an adjustment to account for the axial phase variation.

D. Azimuthal and axial bunching—A qualitative discussion

The electrons are displaced by rf forces from their zero-order orbits in the effective cyclotron phase space. Here, we consider two primary bunching processes that result from the angular displacement $\Delta\phi_{\text{eff}}$. For a qualitative discussion, variations of v_\perp may be neglected. For simplicity, we assume that initially $v_z=0$ for all electrons.

In the effective cyclotron phase space, the electrons are in slow motion relative to one another as well as to

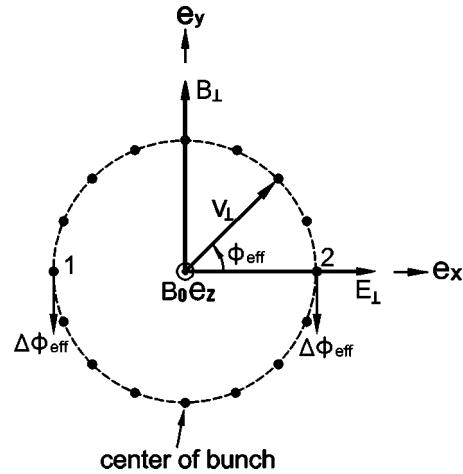


FIG. 6. Bunching in effective cyclotron phase space due to $\mathbf{v}_\perp \times \mathbf{B}_\perp$ magnetic forces. Electrons on the left half-circle and right half-circle experience, respectively, accelerating and decelerating $\mathbf{v}_\perp \times \mathbf{B}_\perp$ forces in the axial direction. This results in increased $\Omega_{\text{eff}} (=k_z v_z + \Omega_e/\gamma)$ for electrons on the left and reduced Ω_{eff} for electrons on the right, both through the $k_z v_z$ term. Hence the electrons tend to form a bunch by moving toward the point marked as “center of bunch.”

the fields. It is therefore convenient to visualize the bunching processes in a sequence of “snapshots” taken at integer multiples of the wave period. In these snapshots, the rf fields are in fixed orientations, as in Figs. 5 and 6. Only a departure from exact synchronism, due to initial detuning or subsequent electron-wave interactions, will result in angular displacements of the electrons relative to the fields. The two bunching effects are considered separately below with the understanding that they can be linearly superposed.

1. Azimuthal bunching

In Figs. 5 and 6, electrons 1 and 2 represent, respectively, electrons on the left half-circle ($\mathbf{v}_\perp \cdot \mathbf{E}_\perp < 0$, energy-gaining phase) and right half-circle ($\mathbf{v}_\perp \cdot \mathbf{E}_\perp > 0$, energy-losing phase). The effect of the electric force is shown in Fig. 5. Electron 1 gains energy, becomes heavier in relativistic mass (γm_e), rotates at a reduced¹ Ω_e/γ , and thus acquires a phase lag ($\Delta\phi_{\text{eff}} < 0$). For the opposite reason, electron 2 will lose energy and acquire a phase advance ($\Delta\phi_{\text{eff}} > 0$). The electrons thus tend to bunch toward the phase angle marked as “center of bunch” in Fig. 5, at which $\mathbf{v}_\perp \cdot \mathbf{E}_\perp = 0$ and there is no net energy transfer. If the static magnetic field is initially detuned from exact synchronism so that $\Omega_{\text{eff}} \lesssim \omega$, the electrons will rotate as a whole in the clockwise sense while the bunch is being formed. Hence the center of the bunch will gradually slip into the right half-circle, resulting in a net energy transfer to the wave. For the opposite

¹The reduction in cyclotron frequency at a faster speed is due to the increased Larmor radius.

detuning, the direction of energy flow will be reversed. The trend for azimuthal bunching can be summarized as

$$\Omega_{\text{eff}} \lesssim \omega, \quad \text{positive emission}, \quad (13a)$$

$$\Omega_{\text{eff}} \gtrsim \omega, \quad \text{negative emission}. \quad (13b)$$

In the discussion above, it is instructive to distinguish two aspects of the relativistic effects: The *absolute magnitude* of γ determines the zero-order electron cyclotron frequency, whereas *phase-dependent variations* of γ cause azimuthal bunching (discussed further in Sec. IV.D).

2. Axial bunching

Figure 6 illustrates how axial forces also lead to electron bunching in the effective cyclotron phase space. Electron 1, acted upon by a positive $\mathbf{v}_\perp \times \mathbf{B}_\perp$ force, gains a positive incremental velocity Δv_z . Because $k_z > 0$, Ω_{eff} increases by $k_z \Delta v_z$, which results in a phase advance. For the opposite reason, electron 2 slips back in phase. Again, bunching occurs, now with the center of the bunch on the opposite side of that shown in Fig. 5. For the center of the bunch to advance to the right half-space (energy-losing phases), the static magnetic field must be initially detuned, so that $\Omega_{\text{eff}} \gtrsim \omega$. With the opposite detuning, the electrons absorb energy from the wave. As in the case of azimuthal bunching, the energy transfer is effected through the cyclotron motion; however, the trend for axial bunching is reversed:

$$\Omega_{\text{eff}} \gtrsim \omega, \quad \text{positive emission}, \quad (14a)$$

$$\Omega_{\text{eff}} \lesssim \omega, \quad \text{negative emission}. \quad (14b)$$

The opposing trends of Eqs. (13) and (14) permit an experimental identification of either bunching mechanism (discussed in Sec. III.A) and also suggest a competitive relationship between the two bunching mechanisms (discussed further in Sec. IV.C). In the beam reference frame ($v_z = 0$ initially), Ω_{eff} in Eqs. (13) and (14) equals Ω_e / γ .

E. Linear analysis

1. Equations of motion

Linear analyses of cyclotron interactions in fixed rf fields can be found in many early papers.² In the linear theory, rf forces on the electrons are approximately evaluated along the zero-order orbits. Orbital perturbations due to the rf forces are then calculated, and they result in electron bunching and consequently an analytical expression for the energy transfer. The electrons are each governed by the relativistic equation of motion,

$$\frac{d}{dt}(\gamma m_e \mathbf{v}) = -e \mathbf{E}_\perp - \frac{e}{c} \mathbf{v} \times (B_0 \mathbf{e}_z + \mathbf{B}_\perp), \quad (15)$$

where \mathbf{E}_\perp and \mathbf{B}_\perp are given by Eqs. (3) and (4). The position vector of the electron can be written as

$$\mathbf{x} = \int_0^t \mathbf{v} dt + \mathbf{x}_0, \quad (16)$$

where \mathbf{x}_0 is the initial value. Equation (6), rewritten here in terms of γ , serves as a convenient auxiliary equation,

$$\frac{d}{dt} \gamma = -\frac{e E_0 v_\perp}{m_e c^2} \cos(\omega t - k_z z - \phi). \quad (17)$$

Because bunching occurs in azimuthal and axial phase angles, the processes are more transparent in polar coordinates than in Cartesian coordinates. Thus, writing $\mathbf{v} = v_\perp (\cos \phi \mathbf{e}_x + \sin \phi \mathbf{e}_y) + v_z \mathbf{e}_z$, taking the dot product of Eq. (15) separately with $\cos \phi \mathbf{e}_x + \sin \phi \mathbf{e}_y$, $-\sin \phi \mathbf{e}_x + \cos \phi \mathbf{e}_y$, and \mathbf{e}_z , and substituting Eqs. (3), (4), and (17) into the resulting equations, we obtain exactly

$$\frac{d}{dt} v_\perp = -\frac{e E_0}{\gamma m_e} \left(1 - \frac{v_\perp^2}{c^2} - \frac{k_z v_z}{\omega} \right) \cos(\omega t - k_z z - \phi), \quad (18)$$

$$\frac{d}{dt} \phi = \frac{\Omega_e}{\gamma} - \frac{e E_0}{\gamma m_e v_\perp} \left(1 - \frac{k_z v_z}{\omega} \right) \sin(\omega t - k_z z - \phi), \quad (19)$$

$$\frac{d}{dt} v_z = -\frac{e E_0 v_\perp}{\gamma m_e} \left(\frac{k_z}{\omega} - \frac{v_z}{c^2} \right) \cos(\omega t - k_z z - \phi). \quad (20)$$

On the right-hand sides of Eqs. (17)–(20), the Ω_e / γ term is due to the static magnetic force [see Eq. (4)]; terms proportional to k_z / ω are due to rf magnetic forces; and the other terms are due to rf electric forces. The rf forces on the electrons vary slowly under the synchronism condition. The \mathbf{E}_\perp electric force and the $\mathbf{v}_z \times \mathbf{B}_\perp$ magnetic force are both in the transverse direction. Components of these two forces tangential³ to \mathbf{v}_\perp cause magnitude variations of v_\perp through Eq. (18). Relativistically, a force aligned tangential to the particle velocity (\mathbf{v}) produces a tangential acceleration γ^2 times smaller than the normal acceleration it would produce when aligned normal to \mathbf{v} (Alonso and Finn, 1970). This accounts for the reduction factor, $1 - v_\perp^2 / c^2$, on the E_\perp force tangential to \mathbf{v}_\perp in Eq. (18). If v_z vanishes, \mathbf{v}_\perp equals the total velocity \mathbf{v} and the reduction factor becomes $1 / \gamma^2$, as expected. Note that the magnetic force is always normal to the total velocity.

Equation (19) governs the rotational motion. The electron rotational frequency is primarily determined by the Ω_e / γ term due to the static magnetic field. Phase-dependent perturbations of γ modulate the electron ro-

²See, for example, Gaponov (1959a, 1959b); Hirshfield, Bernstein, and J. M. Wachtel (1965); Hsu and Robson (1965); Lindsay (1972); Chu (1978); Mourier (1980); Bratman *et al.* (1981); Lindsay, Jones, and Lumsden (1984).

³Here and below, “tangential” and “normal” are in reference to the instantaneous direction of either \mathbf{v}_\perp or \mathbf{v} , while “transverse” and “axial” are in reference to the z direction.

tational frequencies through this term, which results in azimuthal bunching (Sec. II.D.1). In addition, components of the \mathbf{E}_\perp and $\mathbf{v}_z \times \mathbf{B}_\perp$ forces normal to \mathbf{v}_\perp will also modulate the rotational frequencies and bunch the electrons through the remaining terms on the right-hand side of Eq. (19). This results in an additional energy-transfer mechanism to be discussed in Sec. II.E.3.

The $\mathbf{v}_\perp \times \mathbf{B}_\perp$ force accelerates or decelerates v_z through the term proportional to k_z/ω in Eq. (20). This is the force responsible for axial bunching (Sec. II.D.2). The term proportional to v_z/c^2 in Eq. (20), which originates from the time derivative of γ , accounts for the relativistic coupling of transverse and axial motions. The axial momentum is conserved when the electron is acted upon by a transverse force. To conserve axial momentum ($\gamma m_e v_z$), a variation of γ due to the transverse E_\perp force [Eq. (17)] must be accompanied by a variation of v_z , provided v_z is a nonvanishing quantity.⁴

2. Linear solutions

Equations (17)–(20) can be solved by the method of iteration under the assumption of weak rf fields ($E_0 \rightarrow 0$). To avoid complications from the $\mathbf{v}_z \times \mathbf{B}_\perp$ force while still retaining the essential physics, we shall work in the electron reference frame by assuming that initially v_z vanishes for all electrons. Setting $E_0=0$ in Eqs. (17)–(20), we obtain the zero-order electron orbit,

$$\gamma = \gamma_0, \quad v_\perp = v_{\perp 0}, \quad \phi = (\Omega_e/\gamma_0)t + \phi_0, \quad (21)$$

and

$$v_z = z = 0,$$

where quantities with subscript “0” denote initial values and we have assumed that all electrons are initially at $z=0$. The electrons are distinguished by their initial cyclotron phase angles ϕ_0 . The circularly polarized electromagnetic wave has the same amplitude at any z position, and only its field orientation depends on z (see Sec. II.A). Thus, when we assume a random distribution in ϕ_0 , the electron ensemble in the $z=0$ plane is representative of the electrons in any other plane. The transverse position coordinates (neglected) are irrelevant to the energy transfer because the rf fields depend only on z .

Substitution of Eq. (21) into Eqs. (17), (18), and (20) yields

$$\frac{d}{dt} \gamma = -\frac{eE_0 v_{\perp 0}}{m_e c^2} \cos(\varepsilon t - \phi_0), \quad (22)$$

$$\frac{d}{dt} v_\perp = -\frac{eE_0}{\gamma_0 m_e} \left(1 - \frac{v_{\perp 0}^2}{c^2}\right) \cos(\varepsilon t - \phi_0), \quad (23)$$

⁴Consequently, azimuthal bunching due to modulation of γ is always accompanied by axial bunching unless v_z vanishes. The overall phenomenon can nevertheless be regarded as an azimuthal bunching effect, since the accompanied axial bunching disappears when viewed in the reference frame where $v_z=0$.

$$\frac{d}{dt} v_z = -\frac{eE_0 v_{\perp 0} k_z}{\gamma_0 m_e \omega} \cos(\varepsilon t - \phi_0), \quad (24)$$

where ε is given by

$$\varepsilon = \omega - \Omega_e/\gamma_0 \quad (25a)$$

under the present assumption of $v_{z0}=0$. In general, it is defined as

$$\varepsilon = \omega - k_z v_{z0} - \Omega_e/\gamma_0. \quad (25b)$$

The quantity ε is the detuned frequency from exact synchronism and will be referred to as *the detuning factor*. As seen in Eqs. (22)–(24), it is the frequency at which the rf forces act upon the electrons (in the linear approximation). Equations (22)–(24) are readily integrated to yield solutions to first order in E_0 ,

$$\gamma = \gamma_0 - \frac{eE_0 v_{\perp 0}}{m_e c^2 \varepsilon} [\sin(\varepsilon t - \phi_0) + \sin \phi_0], \quad (26)$$

$$v_\perp = v_{\perp 0} - \frac{eE_0}{\gamma_0 m_e \varepsilon} \left(1 - \frac{v_{\perp 0}^2}{c^2}\right) [\sin(\varepsilon t - \phi_0) + \sin \phi_0], \quad (27)$$

$$v_z = -\frac{eE_0 v_{\perp 0} k_z}{\gamma_0 m_e \omega \varepsilon} [\sin(\varepsilon t - \phi_0) + \sin \phi_0]. \quad (28)$$

Integrating Eq. (28), we obtain

$$z = \frac{eE_0 v_{\perp 0} k_z}{\gamma_0 m_e \omega} \left(\frac{1}{\varepsilon^2} [\cos(\varepsilon t - \phi_0) - \cos \phi_0] - \frac{t}{\varepsilon} \sin \phi_0 \right). \quad (29)$$

On the right-hand side of Eq. (19), we substitute the first-order solution for γ [Eq. (26)] into the zero-order term and the zero-order solutions [Eq. (21)] in the first-order term. This results in

$$\begin{aligned} \frac{d}{dt} \phi = & \frac{\Omega_e}{\gamma_0} \left(1 + \frac{eE_0 v_{\perp 0}}{\gamma_0 m_e c^2 \varepsilon} [\sin(\varepsilon t - \phi_0) + \sin \phi_0] \right) \\ & - \frac{eE_0}{\gamma_0 m_e v_{\perp 0}} \sin(\varepsilon t - \phi_0). \end{aligned} \quad (30)$$

Thus

$$\begin{aligned} \phi = & \frac{\Omega_e}{\gamma_0} t + \phi_0 - \frac{eE_0 v_{\perp 0} \Omega_e}{\gamma_0^2 m_e c^2} \left(\frac{1}{\varepsilon^2} [\cos(\varepsilon t - \phi_0) \right. \\ & \left. - \cos \phi_0] - \frac{t}{\varepsilon} \sin \phi_0 \right) + \frac{eE_0}{\gamma_0 m_e v_{\perp 0} \varepsilon} [\cos(\varepsilon t - \phi_0) \\ & \left. - \cos \phi_0 \right]. \end{aligned} \quad (31)$$

3. Energy-transfer mechanisms

The first-order terms in Eqs. (29) and (31) are ϕ_0 -dependent perturbations. For any electron pair separated by 180° in ϕ_0 , the perturbations have the same magnitude but opposite signs. Hence perturbations of z and ϕ lead to axial and azimuthal electron bunching, respectively. All of these perturbations affect energy transfer through their algebraic sum in the effective cyclotron phase angle,

TABLE I. Summary of energy-transfer mechanisms, assuming initial v_z vanishes for all electrons. With a finite initial v_z , the $\mathbf{v}_z \times \mathbf{B}_\perp$ force will contribute to mechanisms 3 and 4.

Mechanism	Driving force	Relevant equation	Modulated quantity	Phase bunching	Physical nature ^a	Effect on energy transfer
1	\mathbf{E}_\perp force tangential to \mathbf{v}_\perp	Eq. (17)	γ	azimuthal	relativistic; inertial bunching	stimulated cyclotron emission; ^b dominant mechanism for fast-wave generation
2	$\mathbf{v}_\perp \times \mathbf{B}_\perp$ force	Eq. (20)	v_z	axial	nonrelativistic; inertial bunching	stimulated cyclotron emission; ^b dominant mechanism for slow-wave generation
3	\mathbf{E}_\perp force normal to \mathbf{v}_\perp	Eq. (19)	centripetal acceleration	azimuthal	nonrelativistic; force bunching	cyclotron-resonance absorption; ^c significant on short time scale and at low electron energies
4	\mathbf{E}_\perp force tangential to \mathbf{v}_\perp	Eq. (18)	v_\perp	none	nonrelativistic	cyclotron-resonance absorption; ^c significant on short time scale and at low electron energies

^aOnly the effect that is absent from the nonrelativistic formalism is labeled “relativistic.”

^bUnder condition (39a).

^cUnder all conditions.

$$\begin{aligned} \phi_{\text{eff}} = \phi + k_z z = & \frac{\Omega_e t}{\gamma_0} + \phi_0 - \frac{e E_0 v_{\perp 0}}{\gamma_0 m_e \omega} \left(\frac{\omega \Omega_e}{\gamma_0 c^2} - k_z^2 \right) \\ & \times \left(\frac{1}{\varepsilon^2} [\cos(\varepsilon t - \phi_0) - \cos \phi_0] - \frac{t}{\varepsilon} \sin \phi_0 \right) \\ & + \frac{e E_0}{\gamma_0 m_e v_{\perp 0} \varepsilon} [\cos(\varepsilon t - \phi_0) - \cos \phi_0], \end{aligned} \quad (32)$$

where the first two terms on the right-hand side represent the zero-order phase advance, on which the perturbations are independently superposed.

In terms of the driving force, each phase perturbation in Eq. (32) can be traced to a different rf force. The term proportional to $\omega \Omega_e$ is due to the \mathbf{E}_\perp force tangential to \mathbf{v}_\perp , and the term proportional to k_z^2 is due to the axial $\mathbf{v}_\perp \times \mathbf{B}_\perp$ force. Their bunching effects are shown in Figs. 5 and 6. The last term is due to the \mathbf{E}_\perp force normal to \mathbf{v}_\perp , a centripetal force. Referring to Fig. 4(a), rotating frequencies of electrons on the left half-circle are reduced by this force, while those on the right half-circle are increased by it. Electrons are thus bunched azimuthally toward the maximum accelerating phase of the \mathbf{E}_\perp force [$\theta=90^\circ$ in Fig. 4(a)], and this always results in net energy absorption by the electrons. Bunching mechanisms associated with these three forces have been summarized in Table I.

In terms of the electron responses, the three bunching mechanisms can be divided into two types, referred to as “inertial bunching” and “force bunching” (see, for example, Bratman *et al.*, 1981). In *inertial bunching* (mechanisms 1 and 2 in Table I), the phase perturbation results indirectly from the driving force in that the force must first generate a perturbation on either γ or v_z . Once γ or v_z has been perturbed, the resultant perturbation of ϕ or $k_z z$ continues to grow even after the force is terminated (an initial effect). Consider Eqs. (26) and

(28), for example. The perturbation of γ or v_z by the sinusoidal rf forces, when averaged over time, has a finite value unless $\phi_0=0$ or π . This results in the term in Eq. (32) which grows linearly in time. In *force bunching* (mechanism 3 in Table I), the phase perturbation results directly from the action of the driving force. The perturbation varies only in the presence of the force and will be “frozen” as soon as the force is terminated.

On the long time scale ($|\varepsilon|t \gg 1$), inertial bunching obviously dominates over force bunching. On the short time scale ($|\varepsilon|t \ll 1$), however, all perturbations are of comparable magnitudes. Expanding⁵ Eq. (32) in εt , we obtain the combined effect,

$$\begin{aligned} \phi_{\text{eff}} \cong & \frac{\Omega_e t}{\gamma_0} + \phi_0 + \frac{e E_0 v_{\perp 0} t^2}{\gamma_0 m_e \omega} \left(\frac{\omega \Omega_e}{\gamma_0 c^2} - k_z^2 \right) \cos \phi_0 \\ & + \frac{e E_0 t}{\gamma_0 m_e v_{\perp 0}} \sin \phi_0, \quad |\varepsilon|t \ll 1. \end{aligned} \quad (33)$$

It can be seen that inertial bunching strengthens with quadratic time dependence, whereas force bunching grows linearly in time.⁶ Thus force bunching is an effect of short-term significance—it dominates initially before being overtaken by inertial bunching.

There is one additional energy-transfer mechanism due to the v_\perp modulation. Apply Eq. (27) to any electron pair with the same initial velocity $v_{\perp 0}$ but a 180° difference in cyclotron phase angle ϕ_0 . Acted upon by the rf electric force over an infinitesimal duration, the incremental velocity (Δv_\perp) of the two electrons will be equal in magnitude but opposite in sign [see Eq. (27)]. However, the sum of their kinetic energies, expressed nonrelativistically for simplicity, $\frac{1}{2} m_e (v_{\perp 0} \pm \Delta v_\perp)^2$, represents a net increase over the initial sum. The variation

⁵The expansion is exact when $\varepsilon=0$.

⁶Hence inertial bunching and force bunching are also referred to, respectively, as “quadratic bunching” and “linear bunching” (Gaponov, Petelin, and Yulpatov, 1967).

of v_{\perp} is a direct response to the driving force and thus involves no inertial effect. Similar to force bunching, this is an absorption mechanism of short-term significance (mechanism 4 in Table I).

4. Cyclotron emission and absorption

Substituting Eqs. (27) and (32) into Eq. (17) and keeping terms up to second order in E_0 through Taylor expansion of the cosine function in Eq. (17), we obtain

$$\begin{aligned} \frac{d}{dt} \gamma = & \frac{e^2 E_0^2 v_{\perp 0}^2}{\gamma_0 m_e^2 c^2 \omega} \left(\frac{\omega \Omega_e}{\gamma_0 c^2} - k_z^2 \right) \left(\frac{1}{2 \varepsilon^2} \sin 2(\varepsilon t - \phi_0) \right. \\ & - \frac{1}{\varepsilon^2} \sin(\varepsilon t - \phi_0) \cos \phi_0 - \frac{t}{\varepsilon} \sin(\varepsilon t \\ & - \phi_0) \sin \phi_0 \left. \right) - \frac{e^2 E_0^2}{\gamma_0 m_e^2 c^2 \varepsilon} \left(\frac{1}{2} \sin 2(\varepsilon t - \phi_0) \right. \\ & - \sin(\varepsilon t - \phi_0) \cos \phi_0 \left. \right) - \frac{e E_0 v_{\perp 0}}{m_e c^2} \cos(\varepsilon t - \phi_0) \\ & + \frac{e^2 E_0^2}{\gamma_0 m_e^2 c^2 \varepsilon} \left(1 - \frac{v_{\perp 0}^2}{c^2} \right) \left(\frac{1}{2} \sin 2(\varepsilon t - \phi_0) \right. \\ & \left. + \cos(\varepsilon t - \phi_0) \sin \phi_0 \right). \end{aligned} \quad (34)$$

Equation (34) applies to a single electron. The electron may gain or lose energy depending upon its initial phase angle ϕ_0 . Integrating over ϕ_0 gives the average rate of change of the relativistic factor,

$$\begin{aligned} \left\langle \frac{d}{dt} \gamma \right\rangle_{\phi_0} = & \frac{1}{2\pi} \int_0^{2\pi} \left(\frac{d}{dt} \gamma \right) d\phi_0 \\ = & - \frac{e^2 E_0^2 v_{\perp 0}^2}{2 \gamma_0 m_e^2 c^2 \omega} \left(\frac{\omega \Omega_e}{\gamma_0 c^2} - k_z^2 \right) \\ & \times \left(\frac{\sin \varepsilon t}{\varepsilon^2} - \frac{t \cos \varepsilon t}{\varepsilon} \right) + \frac{e^2 E_0^2}{\gamma_0 m_e^2 c^2} \\ & \times \left(1 - \frac{v_{\perp 0}^2}{2c^2} \right) \frac{\sin \varepsilon t}{\varepsilon}. \end{aligned} \quad (35)$$

To be consistent with subsequent nonlinear studies, we define a figure of merit—the *interaction efficiency* (η)—in terms of the time-integrated electron energy loss divided by the total kinetic energy,

$$\eta = \frac{-1}{\gamma_0 - 1} \int_0^t \left\langle \frac{d}{dt} \gamma \right\rangle_{\phi_0} dt, \quad (36)$$

where a positive value of η implies net energy transfer to the wave. Substituting Eq. (35) into Eq. (36) and carrying out the time integration yields the linear interaction efficiency,

$$\begin{aligned} \eta_{lin} = & \frac{e^2 E_0^2}{\gamma_0 (\gamma_0 - 1) m_e^2 c^2} \left[\frac{v_{\perp 0}^2}{\omega} \left(\frac{\omega \Omega_e}{\gamma_0 c^2} - k_z^2 \right) \right. \\ & \times \left(\frac{2 \sin^2 \frac{\varepsilon t}{2}}{\varepsilon^3} - \frac{t \sin \varepsilon t}{2 \varepsilon^2} \right) - 2 \left(1 - \frac{v_{\perp 0}^2}{2c^2} \right) \frac{\sin^2 \frac{\varepsilon t}{2}}{\varepsilon^2} \left. \right] \\ \cong & \frac{e^2 E_0^2}{\gamma_0 (\gamma_0 - 1) m_e^2 c^2} \left[\frac{v_{\perp 0}^2}{\omega} \left(\frac{\omega^2}{c^2} - k_z^2 \right) \right. \\ & \times \left(\frac{2 \sin^2 \frac{\varepsilon t}{2}}{\varepsilon^3} - \frac{t \sin \varepsilon t}{2 \varepsilon^2} \right) - 2 \left(1 - \frac{v_{\perp 0}^2}{2c^2} \right) \frac{\sin^2 \frac{\varepsilon t}{2}}{\varepsilon^2} \left. \right]. \end{aligned} \quad (37)$$

The first expression on the right-hand side of Eq. (37) is an exact linear solution of Eqs. (17)–(20). The second expression is valid under the synchronism condition ($\omega \cong \Omega_e / \gamma_0$). Expanding the sinusoidal functions in the limit $|\varepsilon| t \ll 1$, we obtain the short-time behavior for synchronous interaction,

$$\begin{aligned} \eta_{lin} \cong & \frac{e^2 E_0^2}{\gamma_0 (\gamma_0 - 1) m_e^2 c^2} \left[\frac{1}{24} \left(\frac{\omega^2}{c^2} - k_z^2 \right) \frac{v_{\perp 0}^2 \varepsilon}{\omega} t^4 \right. \\ & \left. - \frac{1}{2} \left(1 - \frac{v_{\perp 0}^2}{2c^2} \right) t^2 \right], \quad |\varepsilon| t \ll 1. \end{aligned} \quad (38)$$

In Eqs. (37) and (38), terms proportional to ω^2/c^2 and k_z^2 are due to inertial bunching in the azimuthal and axial phase angles, respectively. The two bunching mechanisms are responsible for the stimulated cyclotron emission. However, they work in opposite senses in such a way (cf. Figs. 5 and 6) that their effects tend to cancel. Azimuthal bunching dominates in the fast-wave regime, whereas axial bunching dominates in the slow-wave regime. There is no emission when the two bunching effects cancel ($\omega^2/c^2 = k_z^2$) or when the center of the bunch remains in the phase of zero tangential force ($\varepsilon = 0$). Otherwise, the sum of the two “emission” terms oscillates in time between positive and negative values at the frequency ε [on a long time scale, see Eq. (37)]. Equation (38) indicates that the sum assumes a positive value in the first half-cycle when

$$\varepsilon(\omega^2 - k_z^2 c^2) > 0, \quad \text{positive emission.} \quad (39a)$$

Under the opposite condition, the same bunching mechanisms lead to wave absorption by the electrons in the first half-cycle:

$$\varepsilon(\omega^2 - k_z^2 c^2) < 0, \quad \text{negative emission.} \quad (39b)$$

Obviously, condition (39a) is of practical interest and will be assumed in subsequent discussions. Devices based on stimulated cyclotron emission thus far invariably employ the fast-wave interaction, for which azimuthal bunching dominates and condition (39a) re-

quires $\varepsilon > 0$. While an “electron cyclotron maser” is traditionally taken to be the emission in a fast-wave interaction with $\varepsilon > 0$, there is a completely equivalent role for axial bunching in a slow-wave interaction with $\varepsilon < 0$. The latter has not been utilized because of the disadvantages of the slow-wave circuit and the sensitivity to electron velocity spread.

As discussed earlier, there are also two absorption mechanisms at work simultaneously (mechanisms 3 and 4 in Table I). Both force bunching and v_{\perp} modulation lead to energy absorption by the electrons, in the ratio of 1 to $1 - v_{\perp 0}^2/c^2$. [This can be seen by averaging the relevant terms in Eq. (34) over ϕ_0 .] Each makes a negative contribution to the interaction efficiency under all conditions and at all times, and this is referred to as cyclotron-resonance absorption. Their combined effect is represented by the term proportional to $1 - v_{\perp 0}^2/2c^2$ on the right-hand side of Eqs. (37) and (38).

Early papers employed the terms “positive” and “negative” absorption to describe the overall effect as well as to emphasize the novelty of negative absorption (Hirshfield and Wachtel, 1964; Hsu and Robson, 1965). In fine resolution, however, four distinctive mechanisms are involved. For a detailed physics examination, we have classified the mechanisms into two categories: “emission” and “absorption.” The two emission mechanisms are inseparable and mutually competitive, whereas the two absorption mechanisms act in concert independently. In further contrast, the emission rate diminishes with decreasing electron energy, whereas the absorption rate not only persists but maximizes at vanishing electron energies [see Eq. (35)]. Finally, we note that the emission mechanisms are emissive under the restrictive condition 39(a) and for a finite duration only, whereas the absorption mechanisms always absorb the wave energy.

The absolute magnitude of the linear efficiency is of little significance. However, its composition, parametric dependence, and temporary behavior provide a general physical picture. The time dependence of the linear efficiency is illustrated (on a relative scale) in Fig. 7 for three sets of values of ε/ω and V_b (eV_b being the electron energy). A fast wave ($\omega/k_z = 2c$) is assumed for all cases; however, the illustration applies to slow-wave interactions (with $\varepsilon < 0$) as well. The overall efficiency [Eq. (37)] is displayed by solid curves. The portion due to the two emission mechanisms is shown with dashed curves and that due to the two absorption mechanisms is shown with dotted curves. The characteristics are significantly different for different time scales, as discussed below.

a. Short time scale

On the short time scale ($|\varepsilon|t \ll 1$), emitted and absorbed energies scale as follows [see Eq. (38)]:

$$\text{emitted energy} \sim t^4, \quad |\varepsilon|t \ll 1, \quad (40a)$$

$$\text{absorbed energy} \sim t^2, \quad |\varepsilon|t \ll 1. \quad (40b)$$

Thus the interaction will always begin with electrons absorbing the wave energy, which results in an initial dip

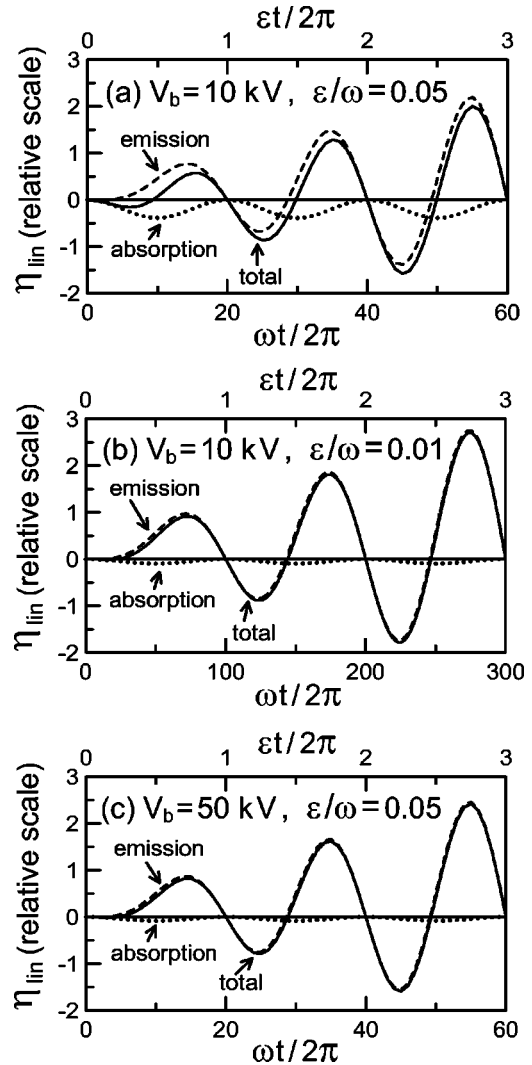


FIG. 7. Time dependence of the analytically evaluated linear efficiency for fast-wave interactions ($\omega/k_z = 2c$). (a) $V_b = 10$ kV, $\varepsilon/\omega = 0.05$, (b) $V_b = 10$ kV, $\varepsilon/\omega = 0.01$, and (c) $V_b = 50$ kV, $\varepsilon/\omega = 0.05$: solid curves, overall efficiency; dashed curves, emission portion; dotted curves, absorption portion. The emission-to-absorption ratio in (a) can be enhanced by either decreasing the detuning factor as in (b) or increasing the electron energy as in (c).

in the overall efficiency. In contrast to force bunching, inertial bunching is a delayed effect; that is, perturbations on z and ϕ first require perturbations on v_z and γ . In further contrast, the electrons are initially bunched toward the phase angle of zero energy transfer (see Figs. 5 and 6). With a frequency detuning factor (ε) of the proper sign, the center of the bunch then gradually slips/advances to the decelerating phase, thus incurring further delay. These two factors account for the dramatic difference in the short-time scaling in favor of absorption. On the other hand, the short-time scaling also indicates that emission grows faster than absorption and thus will be expected to dominate at a later stage.

b. Synchronous time scale

The electron will remain in synchronism with the wave over a duration given by $t \sim \pi/|\varepsilon|$. This is the maxi-

imum span for continuous energy extraction, and thus it is the time scale of practical interest. In device applications, it is important that the emission gain dominates over the absorption loss on this time scale. When $|\varepsilon|t \sim \pi$, the sinusoidal functions in Eq. (37) are of the order of unity. We may therefore write down two scaling laws. In terms of the electron energy, the ratio of emitted energy to absorbed energy scales as

$$\frac{\text{emitted energy}}{\text{absorbed energy}} \sim \frac{v_{\perp 0}^2}{1 - v_{\perp 0}^2/2c^2}, \quad |\varepsilon|t \sim \pi, \quad (41a)$$

and in terms of the frequency detuning factor, it scales as

$$\frac{\text{emitted energy}}{\text{absorbed energy}} \sim \frac{1}{|\varepsilon|}, \quad |\varepsilon|t \sim \pi. \quad (41b)$$

Equation (41a) indicates a decreasing emission-to-absorption ratio at lower electron energies, while Eq. (41b) prescribes a small detuning factor as an effective method of compensation. Thus it is in principle possible for the emission to reach the dominant state on the synchronous time scale at vanishingly small electron energies. Equations (41a) and (41b) provide a useful guide for parameter optimization. As an example, Fig. 7(a) represents a case of marginal interest, in which emission barely exceeds absorption within the synchronous time. This can be remedied by either reducing ε [Fig. 7(b)] or increasing V_b [Fig. 7(c)]. However, the first remedy requires a much longer synchronous time to reach the emission-dominated state [compare the lower time scales of Figs. 7(b) and (c)]. Low electron energy and long interaction time are incompatible with high-power generation. Hence high-power devices always operate at a relatively high electron energy, as in Fig. 7(c).

c. Long time scale

On the long time scale ($|\varepsilon|t \gg \pi$), Eq. (37) is dominated by the emission term that is linearly proportional to time. Emitted and absorbed energies are both oscillatory in time [Eq. (37)]. The emission portion (dashed curves in Fig. 7) oscillates between positive and negative peaks with increasing amplitude. This phenomenon is consistent with the inertial nature of the emissive bunching mechanisms. The bunch becomes increasingly tighter while traversing through the decelerating and accelerating phases of the wave. By comparison, the absorption portion (dots) oscillates with a constant amplitude and never changes sign. Given sufficient time, the emission amplitude will eventually overtake the absorption amplitude, even with a large detuning factor. Long-time behavior is a matter of theoretical interest only, since the maximum interaction efficiency is normally obtained on the synchronous time scale as discussed next.

F. Nonlinear behavior

1. Normalized equations

In the linear approximation, electromagnetic forces on the electrons in Eqs. (22)–(24) are evaluated at the

zero-order electron coordinates [Eq. (21)]. The linear theory breaks down when orbital perturbations become too large, due either to a large rf field amplitude (E_0) or to the continued growth of inertial perturbations. The linear efficiency scales with E_0^2 [Eq. (37)] and oscillates indefinitely with increasing amplitude (Fig. 7). It has no upper bound unless nonlinear effects are taken into consideration. Saturated efficiency must therefore be evaluated by permitting large orbital perturbations. Such an evaluation is normally performed numerically.

For numerical calculations, it is convenient to convert Eqs. (16) and (18)–(20) into dimensionless forms by normalizing the wave frequency to unity. Other variables are normalized accordingly: $\bar{t} = \omega t$, $\bar{\mathbf{v}} = \mathbf{v}/c$, $\bar{\mathbf{x}} = \mathbf{x}/\lambda$, $\bar{k}_z = k_z \lambda$, $\bar{\Omega}_e = \Omega_e/\omega$, $\bar{v}_{ph} = \omega/k_z c$, and $\bar{E}_0 = E_0 e/(m_e \omega c)$, where $\lambda (= 2\pi c/\omega)$ is the free-space wavelength. Dimensionless quantities, such as γ (hence the electron energy) and the interaction efficiency, are not normalized. This procedure results in a set of readily integrable first-order differential equations:

$$\frac{d}{d\bar{t}} \bar{\mathbf{x}} = \frac{\bar{\mathbf{v}}}{2\pi}, \quad (42)$$

$$\frac{d}{d\bar{t}} \bar{v}_{\perp} = -\frac{\bar{E}_0}{\gamma} \left(1 - \bar{v}_{\perp}^2 - \frac{\bar{v}_z}{\bar{v}_{ph}} \right) \cos \left(\bar{t} - \frac{2\pi \bar{z}}{\bar{v}_{ph}} - \phi \right), \quad (43)$$

$$\frac{d}{d\bar{t}} \phi = \frac{\bar{\Omega}_e}{\gamma} - \frac{\bar{E}_0}{\gamma \bar{v}_{\perp}} \left(1 - \frac{\bar{v}_z}{\bar{v}_{ph}} \right) \sin \left(\bar{t} - \frac{2\pi \bar{z}}{\bar{v}_{ph}} - \phi \right), \quad (44)$$

$$\frac{d}{d\bar{t}} \bar{v}_z = -\frac{\bar{E}_0 \bar{v}_{\perp}}{\gamma} \left(\frac{1}{\bar{v}_{ph}} - \bar{v}_z \right) \cos \left(\bar{t} - \frac{2\pi \bar{z}}{\bar{v}_{ph}} - \phi \right). \quad (45)$$

We further reduce the number of parameters by working in the electron reference frame ($v_{z0} = 0$). There are still four free parameters to be specified for each numerical run: the initial electron energy (γ_0), the phase velocity (\bar{v}_{ph}), the static magnetic field ($\bar{\Omega}_e$), and the rf field amplitude (\bar{E}_0). In numerical runs, the static magnetic field is specified through the normalized detuning factor ε/ω . Good convergence is obtained with a 30-electron ensemble.

2. Nonlinear interaction

The numerically evaluated interaction efficiency as a function of time is shown in Fig. 8 in both the small- and large-signal rf fields. Consider first the case of fast-wave interaction ($\omega/k_z = 2c$) in Fig. 8(a). In the large-signal run, the detuning factor ($\varepsilon/\omega = 0.044$) and rf field amplitude ($\bar{E}_0 = 0.005$) were both optimized so that the efficiency saturates at the maximum value with respect to ε and \bar{E}_0 , as given by the first peak of the solid curve. A small-signal run of the same case was made and the results [found to be in precise agreement with Eq. (37)] are plotted here for comparison with the large-signal behavior. As in the small-signal run, the large-signal efficiency begins with an absorption dip, because the linear theory still applies to the very early stage of the interaction. The large-signal efficiency is also characterized by

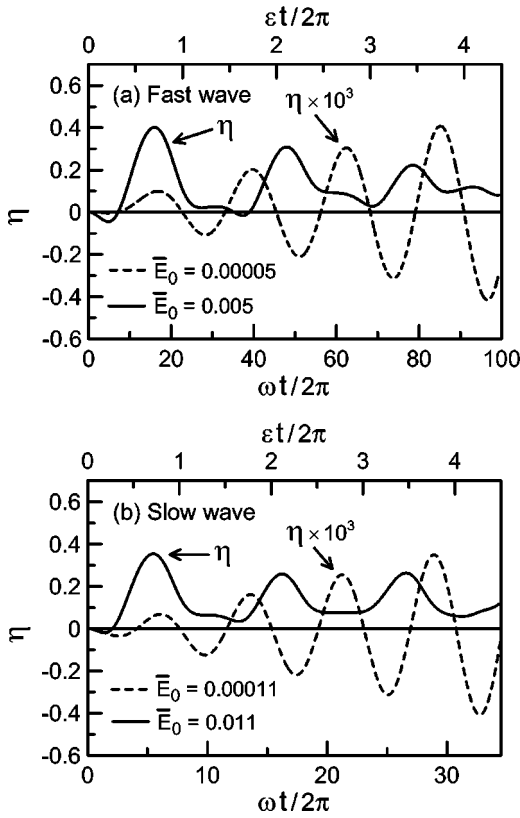


FIG. 8. Numerically evaluated interaction efficiency as a function of time in small-signal (dashed curve) and large-signal (solid curve) rf fields. $V_b=50$ kV for all runs: (a) fast-wave interaction, $\omega/k_z=2c$ and $\epsilon/\omega=0.044$; (b) slow-wave interaction, $\omega/k_z=0.5c$ and $\epsilon/\omega=-0.12$.

multiple peaks, but it reaches the highest value at the first peak on the synchronous time scale. The electrons have developed large orbital perturbations well before the first peak, and subsequent peaks are of decreasing amplitude, indicating a drastic departure from linear behavior. Similar conclusions can be made for the slow-wave interaction [Fig. 8(b)]. In actual device operation, the optimum rf field amplitude is self-consistently generated by an electron beam of properly designed current (see Sec. V.D.2). The electrons are timed to leave the interaction structure at the instant of maximum energy extraction (the first peak), along with the generated power.

Figures 9(a) and (b) show the electron dynamical behavior in the large-signal rf fields of Figs. 8(a) and (b), respectively. The upper portion of each figure reproduces the large-signal efficiency profile in Fig. 8 on the synchronous time scale. The lower portion⁷ displays the corresponding electron distribution in the effective cyclotron phase space at integer multiples of the wave period. Bunch formation is clearly seen at an early stage in each sequence. This is followed by nonlinear energy extraction. The efficiency decreases beyond the saturation

⁷Similar plots are presented in the review article by Baird (1987).

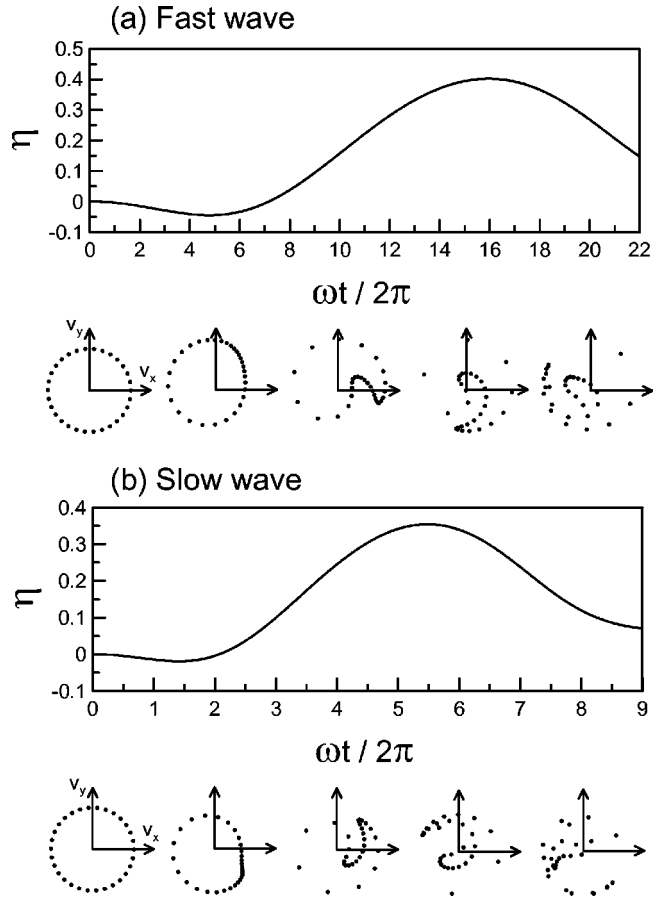


FIG. 9. Electron dynamical behavior in the large-signal rf fields of Figs. 8(a) and (b). The upper portion of each figure displays the temporal profile of the efficiency. The lower portion displays the corresponding electron distribution in the effective cyclotron phase space at integer multiples of the wave period.

point as favorably phased electrons start to move into accelerating phases. The saturation time (τ_{sat}) in both cases corresponds to

$$\tau_{sat} \cong \pi/|\epsilon|, \tag{46}$$

which is on the synchronous time scale as expected.

3. Saturated efficiency and its limitations

Referring to Fig. 8, we take the value at the first peak of the large-signal curve to be the saturated efficiency. Figure 10 presents a general picture of the saturated efficiency (η_{sat}) as a function of V_b . The fast-wave ($\omega/k_z=2c$) and slow-wave ($\omega/k_z=0.5c$) interactions are shown by solid and dashed curves, respectively. The calculation allows sufficient time for the interaction to saturate, and all data points have been maximized with respect to \bar{E}_0 . The saturation time (sample cases shown in Fig. 11) scales inversely with ϵ as in Eq. (46). A larger $|\epsilon|$ thus results in shorter saturation time and hence a broader resonant width. For the wide-ranging electron energies

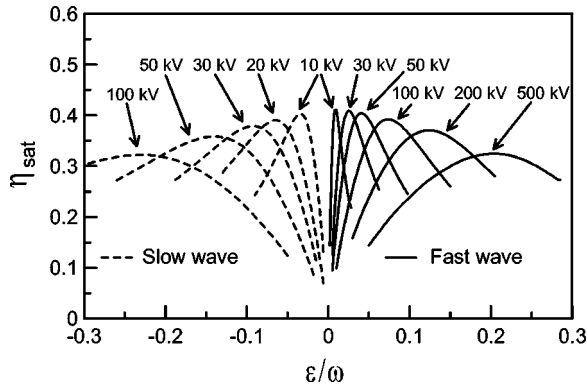


FIG. 10. Saturated efficiency as a function of the normalized detuning factor ϵ/ω for different values of V_b : solid curves, $\omega/k_z=2c$; dashed curves, $\omega/k_z=0.5c$.

shown in Fig. 10, slow-wave and fast-wave efficiencies both reached a sufficiently high level to be of practical interest. The data in Fig. 10, though illustrated at a fixed phase velocity, are representative because the optimized efficiency is not sensitive to the phase velocity.

Figure 10 indicates that the saturated efficiency depends sensitively upon frequency detuning (ϵ/ω) and that, for every electron energy, there is a different optimum detuning value. These features can be explained in light of Fig. 11, which plots the time dependence of the ensemble averages of γ , v_z , and Ω_{eff} ($\cong \Omega_e/\gamma + k_z v_z$) up to the saturation time, for several electron energies at their optimum ϵ/ω shown in Fig. 10. The variation of $\langle \Omega_{\text{eff}} \rangle_{\phi_0}$ is influenced more by the variation of $\langle \gamma \rangle_{\phi_0}$ for the fast-wave interaction and by the variation of $\langle v_z \rangle_{\phi_0}$ for the slow-wave interaction. As a result, $\langle \Omega_{\text{eff}} \rangle_{\phi_0}$ in-

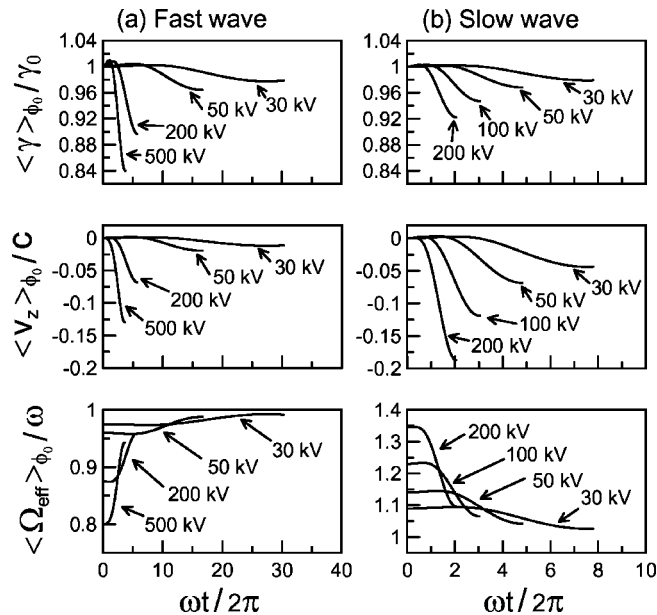


FIG. 11. Time dependence of the ensemble average of γ , v_z , and Ω_{eff} for different electron energies at their respective optimum ϵ/ω shown in Fig. 10. (a) $\omega/k_z=2c$. (b) $\omega/k_z=0.5c$. Each curve is terminated at the saturation time.

creases in the fast-wave interaction, while it decreases in the slow-wave interaction. The frequency should be initially detuned in such a way that $\langle \Omega_{\text{eff}} \rangle_{\phi_0} / \omega$ approaches unity (i.e., better synchronism) in the course of the interaction. Thus, as shown in Figs. 11, $\langle \Omega_{\text{eff}} \rangle_{\phi_0} / \omega$ is initially set to be less than unity for the fast-wave interaction and greater than unity for the slow-wave interaction (corresponding to positive and negative values of ϵ , respectively). Figure 11 also indicates that the fractional change of $\langle \Omega_{\text{eff}} \rangle_{\phi_0}$ increases with the electron energy; hence the efficiency maximizes at larger values of $|\epsilon|$ for higher electron energies (Fig. 10).

As in the conventional TWT, the saturated efficiency is limited by the randomness of the initial electron phase angles. Bunching action puts most, but not all, electrons in favorable phases. Energy is extracted from a majority of electrons, whereas those remaining in the wrong phases end up gaining a substantial amount. Consider Figs. 9(a) and (b) as an example. At saturation, electrons in the core of the bunch lose up to 99% of their energy, while some others gain as much as 50%. Saturation is thus a collective effect of variously behaving electrons. It largely coincides with the state of maximum energy extraction from core electrons in the bunch.

Figure 10 shows the trend of decreasing efficiency with increasing electron energy. At higher electron energies, there is greater fractional change in $\langle \Omega_{\text{eff}} \rangle_{\phi_0}$ in the course of electron-energy depletion (see Fig. 11). As a result, favorably phased electrons are less likely to remain in synchronism with the wave. These electrons tend to advance into accelerating phases⁸ upon losing a smaller fraction of energy than in the weakly relativistic case. This results in a decline in efficiency at high electron energies.

In our prescribed-field model, optimum detuning is achieved by a magnetic-field mismatch. However, the optimum mismatch may not always be realizable in actual devices. For this reason, the saturated efficiency can be significantly lower depending upon the device type and operating parameters (discussed in Sec. V.F).

There are other factors limiting the saturated efficiency. Cyclotron interactions convert the transverse electron energy into radiation. Thus the beam-frame interaction efficiency is reduced when viewed in the laboratory frame, in which the added amount of (axial) electron energy remains almost idle. The electron velocity spread will spoil the synchronism and further degrade the interaction efficiency. The large k_z value associated with the slow wave makes the interaction especially vulnerable to velocity spread. On the other hand, the interaction efficiency can be increased in a number of ways, as will be discussed in Sec. V.F. It is now common to achieve laboratory-frame efficiencies in the neighborhood of 40%.

⁸Some electrons are thus trapped in the phase space. For a detailed description of phase-space trapping, see Sprangle and Drobot (1977).

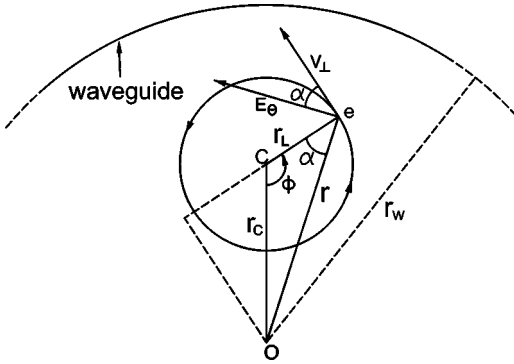


FIG. 12. Model of harmonic cyclotron interactions: E_θ , electric field of the TE_{0n} mode of a circular waveguide; O, center of the waveguide; C, center of electron gyration (guiding center).

G. Harmonic interaction

1. Harmonic fields

The electromagnetic fields are assumed to be transversely uniform in the basic model. If the fields vary in the transverse direction, rf forces experienced by the electrons will no longer be purely sinusoidal due to the finite Larmor radius. As a specific example, we consider the electron interaction with the axisymmetric TE_{0n} mode of a circular waveguide. The rf electric field has only a θ component, which is given by

$$E_\theta = E_0 J_1(k_n r) \cos(\omega t - k_z z), \quad (47)$$

where J_1 is a Bessel function of order 1; $k_n = x_n/r_w$; x_n is the n th nonzero root of $J_1(x) = 0$; r_w is the waveguide radius; and the wave frequency is given by $\omega = (k_n^2 + k_z^2)^{1/2} c$. The electron is assumed to follow a helical orbit in a static magnetic field, with instantaneous phase angle ϕ , radial position r , guiding-center position r_c , Larmor radius r_L , axial velocity v_z , and transverse velocity v_\perp (Fig. 12). The electron energy varies at the rate

$$\begin{aligned} \frac{d}{dt} \gamma &= -\frac{e E_\theta v_\perp}{m_e c^2} \cos \alpha \\ &= -\frac{e E_0 v_\perp}{m_e c^2} J_1(k_n r) \cos(\omega t - k_z z) \cos \alpha, \end{aligned} \quad (48)$$

where α is the angle between v_\perp and E_θ . As shown geometrically in Fig. 12, we may express r and α in terms of r_c , r_L , and ϕ as

$$r = (r_c^2 + r_L^2 - 2r_c r_L \cos \phi)^{1/2}, \quad (49)$$

$$\cos \alpha = (r_L - r_c \cos \phi) / (r_c^2 + r_L^2 - 2r_c r_L \cos \phi)^{1/2}. \quad (50)$$

The electric field tangential to v_\perp may be written as

$$\begin{aligned} E_0 J_1(k_n r) \cos \alpha &= -\frac{E_0}{k_n} \frac{\partial}{\partial r_L} J_0[k_n(r_c^2 + r_L^2 \\ &\quad - 2r_c r_L \cos \phi)^{1/2}], \end{aligned} \quad (51)$$

and Fourier expanded into an infinite number of sinusoidal harmonics of the cyclotron phase angle ϕ ,

$$E_0 J_1(k_n r) \cos \alpha = \sum_{s=0}^{\infty} E_{0s} \cos s \phi, \quad (52)$$

where the coefficient E_{0s} is in the form of a standard integral (Bateman, 1954):

$$\begin{aligned} E_{0s} &= -\Gamma \frac{E_0}{k_n \pi} \frac{\partial}{\partial r_L} \int_0^\pi d\phi J_0[k_n(r_c^2 + r_L^2 \\ &\quad - 2r_c r_L \cos \phi)^{1/2}] \cos s \phi \\ &= -\Gamma E_0 J_s(k_n r_c) J'_s(k_n r_L), \end{aligned} \quad (53)$$

$$\Gamma = \begin{cases} 1, & s=0 \\ 2, & s \neq 0. \end{cases} \quad (54)$$

Substituting Eq. (52) into Eq. (48) yields the rate of change of the electron energy,

$$\begin{aligned} \frac{d}{dt} \gamma &= \frac{-e v_\perp}{m_e c^2} \cos(\omega t - k_z z) \sum_{s=0}^{\infty} E_{0s} \cos s \phi \\ &\cong \frac{-e v_\perp}{2m_e c^2} \sum_{s=0}^{\infty} E_{0s} \cos(\omega t - k_z z - s \phi), \end{aligned} \quad (55)$$

where we have neglected the counter-rotating components $\cos(\omega t - k_z z + s \phi)$, none of which involves cyclotron resonant interaction. Assuming that ϕ advances at the electron cyclotron frequency [Eq. (7)] and z increases at the speed v_z , the electron will be in resonance with the s th harmonic component if

$$\omega - k_z v_z - \frac{s \Omega_e}{\gamma} \cong 0. \quad (56)$$

Equation (56) gives the synchronism condition for the harmonic interaction ($s > 1$), through which more modes can resonantly interact with the electrons. Retaining only the synchronous component on the right-hand side, we see that Eq. (55) is similar in form to Eq. (17) except that the field amplitude is reduced to the effective value E_{0s} .

2. Physical interpretation and significance of harmonic interaction

Calculation of the energy-transfer rate in the full fields of the TE_{01} mode is a complicated exercise (Chu, 1978). However, similarities between Eqs. (55) and (17) suggest that the linear rate will be proportional to the square of E_{0s} , as in Eq. (37). We may therefore define the following coupling coefficient (H_s) as a measure of the interaction strength:

$$H_s(k_n r_c, k_n r_L) = J_s^2(k_n r_c) J_s'^2(k_n r_L). \quad (57)$$

Figure 13 displays H_s as a function of $k_n r_c$ and $k_n r_L$ for the first four harmonics. In the limit $r_L \rightarrow 0$, all of the coupling coefficients vanish except for $s=1$. This verifies that the harmonic fields ($s > 1$) are due to the finite Larmor radius, which allows the electron to experience the transverse field variation. A large Larmor radius (due to high electron energy) will strengthen the $s > 1$ coupling coefficients while reducing the $s=1$ coupling coefficient

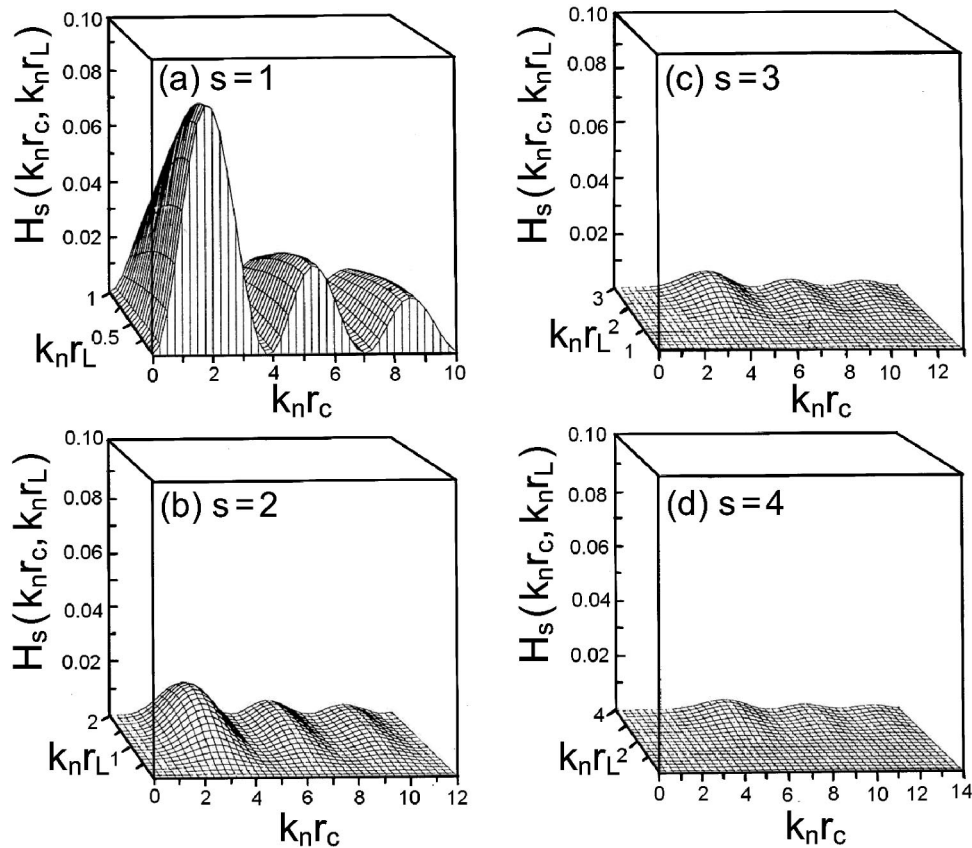


FIG. 13. Dependence of the coupling coefficient for the TE_{on} mode on $k_n r_c$ and $k_n r_L$. From Chu, 1978.

(Fig. 13). Radial periodicity of the electric field results in the periodic dependence of H_s on $k_n r_c$. The peaks of H_s do not in general coincide with those of the actual field except for $s=1$. Note that here the appearance of cyclotron harmonics is not a nonlinear effect, as is clear from the linear dependence of the harmonic field amplitude (E_{0s}) on E_0 [see Eq. (53)].

As can be seen in Eq. (56), harmonic cyclotron interaction can alleviate the magnetic-field requirement by a factor of s . The harmonic coupling coefficient decreases with s and increases with r_L , which suggests that greater beam power and higher electron energy are required to generate the required field strength for efficient harmonic interaction. This trend may be exploited for the generation of high peak power beyond that obtainable in the fundamental harmonic interaction (Kou *et al.*, 1992; Lin *et al.*, 1992; Wang *et al.*, 1992; Wang, McDermott, and Luhmann, 1995, 1996).

3. Optimum conditions for harmonic interaction

The coupling coefficient in Eq. (57) can be generalized to the TE_{mn} modes, where m is the azimuthal mode index. The generalized coupling coefficient assumes the form (Chu and Lin, 1988)

$$H_{sm}(k_{mn}r_c, k_{mn}r_L) = J_{s-m}^2(k_{mn}r_c) J_s'^2(k_{mn}r_L), \quad (58)$$

where $J_m(x)$ is a Bessel function of order m , $x_{mn} = k_{mn}/r_w$, and x_{mn} is the n th nonzero root of $J_m'(x) = 0$. Cyclotron harmonic interactions are subject to, and

also the cause of, mode competition problems. An optimum choice of r_c can boost the desired interaction as well as reduce a large number of competing modes. Equation (58) prescribes a favorable condition for cyclotron harmonic interaction by employing an axis-encircling electron beam ($r_c=0$). In this case, mode competition is least serious, since only the $m=s$ modes have nonvanishing coupling coefficients. In addition, the coupling coefficient with $m=s$ has the maximum value at $r_c=0$.

An axis-encircling electron beam can be generated by gyro-resonant rf acceleration in a cavity (Jory and Trivelpiece, 1968; McDermott, Furuno, and Luhmann, 1985). This process was employed for a demonstration of the TE_{81} -wave amplification at the eighth harmonic interaction (Furuno *et al.*, 1989). At the operating frequency of 16.1 GHz, the required magnetic field was only 1.1 kG. A kicker magnet can also set a linear electron beam into axis-encircling motion. Harmonic radiation up to $s=5$ was generated with a 300-keV electron beam under such an arrangement (Bratman *et al.*, 1999).

H. Summary and discussion

We have presented the basic theory for electron cyclotron interactions with an electromagnetic wave. In the simple model with prescribed field amplitude and detuning factor, the bunching mechanisms and emission/absorption processes are elucidated. Macroscopic prop-

erties of the electrons (such as ac current and charge densities) as well as self-consistent responses of the wave (such as variation of the wave amplitude) have been neglected. These and other overlooked issues (including the wave medium) will be addressed in Sec. IV with a fully self-consistent formalism.

The nonlinear studies in Sec. II.F are based on a single-frequency, steady-state interaction, as is desirable for practical device operation. Saturated behavior (particularly the efficiency levels and limitations), together with the linear theory, provides the physics basis for subsequent device studies. To ensure stable device operation, other nonlinear effects must also be addressed, such as mode competition and nonstationary oscillations. These effects will be examined in Secs. VI–VIII.

Analysis has thus far been conducted in the beam reference frame. It provides an adequate physical picture for the prevailing types of ECM devices to be discussed in Sec. V. The axial velocity will later be incorporated into device studies. In the so-called cyclotron autoresonance maser (CARM) regime, the interaction involves highly relativistic electrons with an axial velocity approaching the speed of light. Both the axial velocity and the associated Doppler shift play important roles in this regime. Extreme sensitivity to electron velocity spread and a high voltage requirement have thus far limited the practical utility of the CARM interaction.⁹

III. EARLY FAST-WAVE EXPERIMENTS

A. Survey of early fast-wave experiments

Studies of cyclotron radiation span over a century and are reviewed by Petelin (1999). Experimental investigations of stimulated cyclotron emission in fast-wave structures began as early as the groundbreaking theories of the late 1950s. Researchers in the U.S. and U.K. performed exploratory fast-wave experiments in small groups (reviewed by Hirshfield and Granatstein, 1977). Although details vary, they were performed under the same set of conditions: stimulated cyclotron emission was generated in a fast-wave structure by a helical electron beam so as to produce electron cyclotron resonance.

Pantell's experiment (1959) is generally regarded as the first in this category. It produced backward-wave oscillations at 2.5–4.0 GHz in a waveguide with an output power of 0.4 W at 0.5% efficiency. Apparently without knowledge of the relativistic bunching mechanism, Chow and Pantell (1960) developed the nonrelativistic axial bunching theory to interpret the observed emission. Subsequently, Bott's experiment (1964) ventured into the submillimeter-wave regime (0.95 mm), achiev-

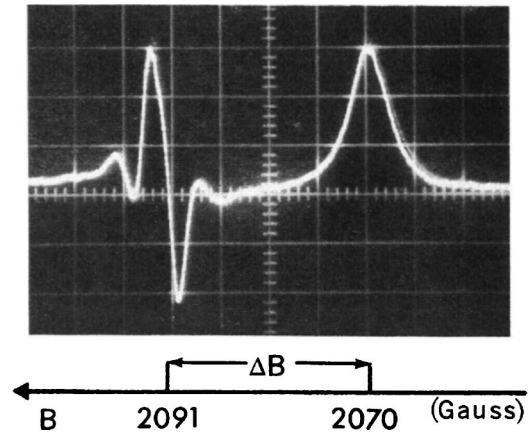


FIG. 14. Measured absorption coefficient vs magnetic field. Resonant magnetic fields for the fast ($\gamma=1.01$) and slow ($\gamma\approx 1$) electrons differ by $\Delta B/B_0 \approx 1\%$, consistent with the 1% difference in electron relativistic masses. From Hirshfield and Wachtel, 1964.

ing cavity oscillations with 1 mW of output power at a low efficiency. Then, Schriever and Johnson (1966; see also Dickerson and Johnson, 1964) demonstrated backward-wave oscillations tunable over a broader band. This was one of the earliest experiments employing a magnetron injection gun (see, for example, Baird and Lawson, 1986), in which the electrons from an annular emitter were accelerated at an angle to the external magnetic field. It achieved an impressive output power of 700 W at 8 GHz with 10% efficiency. Amplification with 20-dB gain was also reported, but no further details were provided. The axial bunching theory was mentioned in both works (Bott, 1964; Schriever and Johnson, 1966) as a possible explanation of the observed radiation.

Hirshfield and Wachtel's experiment (1964) provided the first clear identification of the azimuthal bunching mechanism, and in their paper the emission was named "electron cyclotron maser." The authors injected a 5-kV spiraling electron beam, with the current below the oscillation threshold, into a cavity preexcited by a 5.8-GHz external source. A vivid physical picture emerged from their observations. Figure 14 plots the beam absorption coefficient as a function of the magnetic field, which increases to the left in the trace. As the magnetic field is swept from below to above the resonant value (2091 G for the 5-keV injected electrons), a negative absorption (positive emission) spike transitions to a positive absorption spike. This is precisely the pattern of azimuthal bunching [Eq. (13)]. It is interesting to note that there is also a pure absorption line centered at the resonant magnetic field (2070 G) for slow secondary electrons. This corresponds to the absorption (second) term in Eq. (35), which predicts that cyclotron-resonance absorption persists even at vanishing electron energies. By increasing the beam current in the negative absorption region, Hirshfield and Wachtel were able to observe self-sustaining oscillations at 5.8 GHz, at 10 mW output power and low efficiency. Later, Bott (1965) reported a similar oscillator device producing 2–4 mm radiation at a peak power of 700 mW with efficiency up to 2%. In

⁹Studies of the CARM can be found in Petelin (1974), Bratman *et al.* (1981, 1995), Ginzburg, Zarnitsyna, and Nusinovich (1981), Lin (1984), Fliflet (1986), Lin, Chu, and Bromborsky (1987), Bekefi *et al.* (1989), Chen and Wurtele (1991), and DiRienzo *et al.* (1991).

TABLE II. Early observations of stimulated cyclotron emission in fast-wave devices employing a helical electron beam.

Year	Author(s)	Mechanism attributed to
1959	Pantell	axial bunching
1964	Bott	axial bunching
1964	Hirshfield and Wachtel	azimuthal bunching
1965	Gaponov <i>et al.</i>	azimuthal bunching
1965	Bott	azimuthal bunching
1966	Schrivver and Johnson	axial bunching

this work, the radiation was attributed to the azimuthal bunching mechanism.

By comparison, extensive work by a large group at the Institute of Applied Physics in the former Soviet Union not only was directed toward basic principles (reviewed by Gaponov, Petelin, and Yulpatov, 1967) but also was aimed at the development of practical devices through efficiency and power enhancement (reviewed by Flyagin *et al.*, 1977). Initial experimental results were reported on amplification and oscillations in a crossed-field device called the trochotron (Antakov *et al.*, 1960). In this device, the electrons moved along the waveguide in $\mathbf{E} \times \mathbf{B}$ drift motion under the influence of crossed electric and magnetic fields (both were static). The electron beam interacted with a transverse magnetic wave. As a traveling-wave amplifier, the device produced 750 W of 8-mm radiation with a gain of 10 dB and an efficiency of 25% (Antakov *et al.*, 1966). However, the $\mathbf{E} \times \mathbf{B}$ drift velocity was reduced in high-frequency operation, for which the static B field needed to be increased while the static E field was limited by the breakdown strength (Flyagin *et al.*, 1977). This imposed an unfavorable limit on the beam current at high frequencies.

Emphasis was then shifted to devices driven by helical electron beams moving along the magnetic field. The first attempt (Gaponov *et al.*, 1965) resulted in a prototype gyromonotron complete with the magnetron injection gun and the open cavity (Vlasov *et al.*, 1969). This experiment achieved second-harmonic oscillations at 25 GHz, producing 190 W of output power at $\sim 3\%$ efficiency. It was then followed by rapid development leading to MW-level sources for practical applications (discussed later in Sec. V.D.3).

B. Summary and discussion

Table II classifies the early fast-wave experiments discussed above by the mechanism to which the authors attributed the observation. The experiments were not so different in their actual configuration but were divided in terms of interpretations. Clearly, the existence of two bunching mechanisms made an unequivocal identification of the gain mechanism difficult (Hirshfield and Granatstein, 1977). Hirshfield and Wachtel's experiment (1964) was designed to test the validity of the azimuthal bunching mechanism under conditions of negligible axial bunching. Thus it did not entirely preclude the axial bunching mechanism as a possible explanation of

the results of Pantell (1959) and Bott (1964). On the other hand, Soviet authors recognized the role of azimuthal bunching from the very inception of their research. Axial bunching was regarded as a minor companion in the overall process. The issue raised was the deficiency of the nonrelativistic treatment, which was considered as causing the omission of a significant portion of the induced radiation (Gaponov and Yulpatov, 1967).

Questions remain as to the exact role of the axial bunching mechanism. The answer in large part is implicit in the algebraic expressions for the two bunching effects.¹⁰ Their relative magnitudes suggest the dominance of azimuthal bunching in the fast-wave regime and axial bunching in the slow-wave regime [see Eq. (37)]. The subtraction sign joining the two expressions further suggests an opposing relation between the two mechanisms. However, the physical relation between the two mechanisms still merits a closer examination. A definitive answer, as well as a broader physical picture, lies in a plasma-physics treatment, as is presented in the following section.

IV. THE ELECTRON CYCLOTRON MASER AS A PLASMA INSTABILITY

ECM theories deal mainly with beam-wave interactions in an rf structure. On the other hand, a magnetized plasma is a medium that supports a variety of waves at the electron cyclotron frequency. These waves can also be resonantly destabilized by gyrating electrons and, as will be shown, provide further insight into the ECM interaction. In this section, we analyze the ECM as a plasma instability following Chu and Hirshfield (1978). Other related plasma instabilities will be surveyed at the end.

A. Relativistic dispersion relation of right-hand circularly polarized waves

Consider an infinite plasma of uniform density (n_0) immersed in a uniform magnetic field $B_0 \mathbf{e}_z$. At high frequencies, the plasma ions can be regarded as an immobile, charge-neutralizing background. In the limit of small-amplitude electromagnetic fields ($\mathbf{E}_1, \mathbf{B}_1$), the electron electrodynamics is governed by the linearized relativistic Vlasov equation,

$$\begin{aligned} \frac{\partial}{\partial t} f_1 + \mathbf{v} \cdot \frac{\partial}{\partial \mathbf{x}} f_1 - \frac{e}{c} \mathbf{v} \times \mathbf{B}_0 \cdot \frac{\partial}{\partial \mathbf{p}} f_1 \\ = e \left(\mathbf{E}_1 + \frac{1}{c} \mathbf{v} \times \mathbf{B}_1 \right) \cdot \frac{\partial}{\partial \mathbf{p}} f_0, \end{aligned} \quad (59)$$

and the field equation

¹⁰See, for example, Hirshfield, Bernstein, and Wachtel (1965); Gaponov, Petelin, and Yulpatov (1967); Gaponov and Yulpatov (1967); Sehn and Hayes (1969); Lindsay (1972); and also Eq. (37) in Sec. II.E.

$$\nabla \times \nabla \times \mathbf{E}_1 = -\frac{1}{c^2} \frac{\partial^2}{\partial t^2} \mathbf{E}_1 - \frac{4\pi}{c^2} \frac{\partial}{\partial t} \mathbf{J}_1, \quad (60)$$

where f_0 is the initial distribution function (normalized to unity), f_1 is the perturbation of f_0 , and J_1 is the perturbed current given by

$$\mathbf{J}_1 = -e \int f_1 \mathbf{v} d^3p. \quad (61)$$

Equations (59)–(61) may be solved by the method of characteristics (Krall and Trivelpiece, 1973; Stix, 1992). For waves propagating along the magnetic field, solutions are either electromagnetic ($\nabla \cdot \mathbf{E} = 0$) or electrostatic ($\nabla \times \mathbf{E} = 0$). In particular, we are interested in right-hand circularly polarized electromagnetic waves of the form

$$\mathbf{E}_1 = E_0(\mathbf{e}_x + i\mathbf{e}_y)e^{-i\omega t + ik_z z}, \quad (62)$$

$$\mathbf{B}_1 = \frac{k_z c}{\omega} \mathbf{e}_z \times \mathbf{E}_1. \quad (63)$$

Standard manipulations yield the following dispersion relation:

$$\omega^2 - k_z^2 c^2 = -\pi \omega_{pe}^2 \int_0^\infty p_\perp dp_\perp \int_{-\infty}^\infty dp_z \times \frac{\left(\omega - \frac{k_z p_z}{\gamma m_e} \right) p_\perp \frac{\partial f_0}{\partial p_\perp} + \frac{k_z}{\gamma m_e} p_\perp^2 \frac{\partial f_0}{\partial p_z}}{\gamma \omega - \frac{k_z p_z}{m_e} - \Omega_e}, \quad (64)$$

where $\omega_{pe}^2 = 4\pi n_0 e^2 / m_e$, $\Omega_e = eB_0 / m_e c$, and $\gamma = (1 + p_\perp^2 / m_e^2 c^2 + p_z^2 / m_e^2 c^2)^{1/2}$.

Equation (64) is a special case of the general form of the relativistic dispersion relation for a magnetized plasma (see, for example, Stix, 1992, Sec. 10-6) under assumptions (62) and (63). Integrating Eq. (64) by parts over p_\perp and p_z , we obtain

$$\begin{aligned} \omega^2 - k_z^2 c^2 &= 2\pi \omega_{pe}^2 \int_0^\infty p_\perp dp_\perp \int_{-\infty}^\infty dp_z \frac{f_0}{\gamma} \\ &\times \left[\frac{\omega - \frac{k_z p_z}{\gamma m_e}}{\omega - \frac{k_z p_z}{\gamma m_e} - \frac{\Omega_e}{\gamma}} - \frac{p_\perp^2 (\omega^2 - k_z^2 c^2)}{2\gamma^2 m_e^2 c^2 \left(\omega - \frac{k_z p_z}{\gamma m_e} - \frac{\Omega_e}{\gamma} \right)^2} \right]. \end{aligned} \quad (65)$$

In carrying out the integration by parts, we have differentiated γ with respect to p_\perp and p_z , which brings out the relativistic mass effect. Terms arising from these differentiations can be combined into a single term proportional to ω^2 , as appears on the right-hand side of Eq. (65).

As in Sec. II, we specialize to the initial distribution,

$$f_0 = \frac{1}{2\pi p_\perp} \delta(p_\perp - p_{\perp 0}) \delta(p_z), \quad (66)$$

which represents a uniform distribution of monoenergetic electrons in random gyrotational motion, with $v_z = 0$ for all electrons. Equation (65) then reduces to

$$\omega^2 - k_z^2 c^2 = \frac{\omega_{pe}^2}{\gamma_0} \left[\frac{\omega}{\omega - \Omega_e / \gamma_0} + \frac{k_z^2 v_{\perp 0}^2 (1 - \omega^2 / k_z^2 c^2)}{2(\omega - \Omega_e / \gamma_0)^2} \right], \quad (67)$$

where γ_0 and $v_{\perp 0}$ are initial values of γ and v_\perp , respectively. For comparison, we write down the corresponding nonrelativistic dispersion relation (Schmidt, 1979),

$$\omega^2 - k_z^2 c^2 = \omega_{pe}^2 \left[\frac{\omega}{\omega - \Omega_e} + \frac{k_z^2 v_{\perp 0}^2}{2(\omega - \Omega_e)^2} \right]. \quad (68)$$

Aside from the modification of plasma and cyclotron frequencies by the relativistic factor γ_0 , Eq. (67) differs qualitatively from Eq. (68) by the presence of the ω^2 term on the right-hand side. This term has been shown to be of purely relativistic origin.

B. Dispersive properties and growth rate

Figure 15 displays the solutions for $\omega (= \omega_r + i\omega_i)$ as a function of k_z for a weakly relativistic and tenuous plasma ($\gamma_0 = 1.02$, $\Omega_e / \gamma_0 \omega_{pe} = 10$). Both relativistic and nonrelativistic solutions are plotted. The real part ω_r gives the dispersive properties of the fast-wave ($\omega/k_z > c$) and slow-wave ($\omega/k_z < c$) branches of the right-hand circularized polarized waves [Figs. 15(a) and (c)]. These are well-known modes of the magnetized plasma (Krall and Trivelpiece, 1973).

Instabilities, indicated by ω_i , occur only in regions where the cyclotron-resonance condition ($\omega \cong \Omega_e / \gamma$) is satisfied. Both branches are unstable in the relativistic model [Fig. 15(b)]; however, only the slow-wave branch is unstable in the nonrelativistic model [Fig. 15(d)]. Because the relativistic effect is absent in the nonrelativistic model, the slow-wave instability in both models must be of a nonrelativistic origin (axial bunching).¹¹ Inclusion of the relativistic effect gives rise to a fast-wave instability due to azimuthal bunching.

C. Physical interpretation

As discussed in Sec. II.B, wave-induced perturbations of γ and v_z result in azimuthal and axial phase bunching, respectively. The mechanisms are different, but their effects are inseparable. Both perturbations change the effective cyclotron frequency Ω_{eff} [Eq. (11)] and, consequently, the electron phase angle relative to the wave. The increment of Ω_{eff} over an infinitesimal time interval Δt can be written

¹¹Weibel (1959) derived the dispersion relation for this instability for the general case of an anisotropic distribution function. The physical mechanism of this instability—axial bunching—was independently proposed by Gaponov (1959a, 1959b) and by Chow and Pantell (1960).

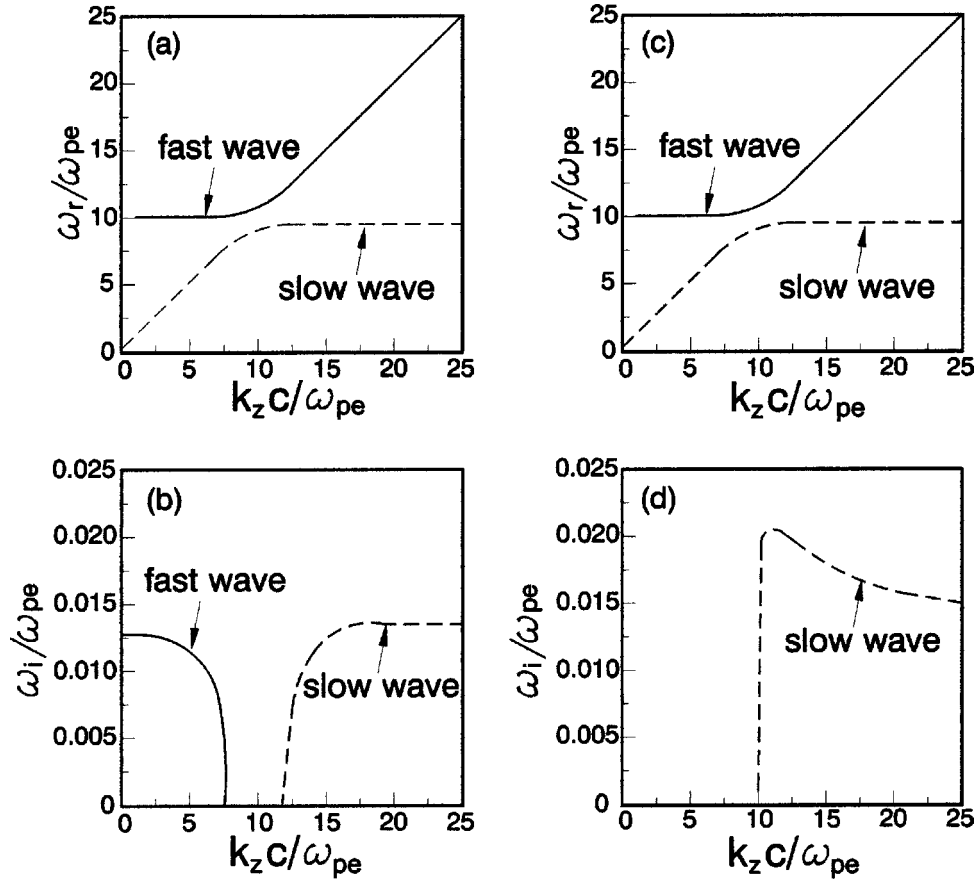


FIG. 15. Solutions for $\omega(=\omega_r+i\omega_i)$ as a function of k_z for a weakly relativistic and tenuous plasma: (a) and (b), ω_r and ω_i predicted by the relativistic dispersion relation [Eq. (67)] for $\gamma_0=1.02$ and $\Omega_e/(\gamma_0\omega_{pe})=10$; (c) and (d), ω_r and ω_i predicted by the nonrelativistic dispersion relation [Eq. (68)] for the same parameters. From Chu and Hirshfield, 1978.

$$\Delta\Omega_{\text{eff}}=k_z\Delta v_z+\Omega_e\Delta\left(\frac{1}{\gamma}\right)=k_z\Delta v_z-\frac{\Omega_e}{\gamma^2}\Delta\gamma, \quad (69)$$

where Δv_z may be evaluated from the axial component of Eq. (15),

$$\begin{aligned} \frac{d}{dt}(\gamma m_e v_z) &= -\frac{e}{c}(\mathbf{v}_\perp \times \mathbf{B}_\perp) \cdot \mathbf{e}_z \\ &= -\frac{ek_z}{\omega}(\mathbf{v}_\perp \cdot \mathbf{E}_\perp). \end{aligned} \quad (70)$$

Because the zero-order v_z vanishes, Eq. (70) readily yields

$$\Delta v_z = -\frac{ek_z}{\gamma m_e \omega}(\mathbf{v}_\perp \cdot \mathbf{E}_\perp)\Delta t. \quad (71)$$

The change of γ is determined by the work done on the electron,

$$\Delta\gamma = -\frac{e}{m_e c^2}(\mathbf{v}_\perp \cdot \mathbf{E}_\perp)\Delta t. \quad (72)$$

Substituting Eqs. (71) and (72) into Eq. (69), we obtain

$$\begin{aligned} \Delta\Omega_{\text{eff}} &= \frac{e}{\gamma m_e \omega} \left(\frac{\Omega_e \omega}{\gamma c^2} - k_z^2 \right) (\mathbf{v}_\perp \cdot \mathbf{E}_\perp) \Delta t \\ &\cong \frac{e}{\gamma m_e \omega} \left(\frac{\omega^2}{c^2} - k_z^2 \right) (\mathbf{v}_\perp \cdot \mathbf{E}_\perp) \Delta t, \end{aligned} \quad (73)$$

where the second equality applies to synchronous interaction and terms proportional to ω^2/c^2 and k_z^2 are due to $\Delta\gamma$ and Δv_z , respectively. The two terms are joined by a subtraction sign, indicating that the two bunching mechanisms are always competing. Thus there is no growth in the neighborhood of $\omega/k_z=c$, where the bunching effects nearly cancel [Fig. 15(b)]. By comparison, the absence of azimuthal bunching in the nonrelativistic model results in an overestimate of the growth rate of the slow-wave instability [Fig. 15(d)].

D. Criterion for mechanism identification

The competition between azimuthal and axial bunching suggests that only the winning mechanism can be regarded as the actual cause for a given instability. We may therefore phrase a criterion as follows:

Azimuthal and axial bunching are both present and are always competitive in electromagnetic cyclotron instabilities.

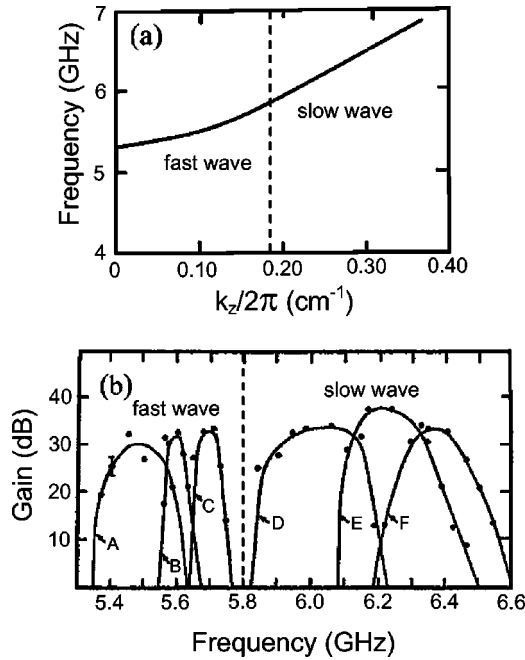


FIG. 16. Electron cyclotron maser instability in a dielectric loaded waveguide at $I_b = 5$ A under different combinations of cathode voltage and magnetic field: (a) measured TE_{01} dispersion curve; (b) small-signal gain. Curve A, 34 kV, 1.90 kG; curve B, 39.7 kV, 1.95 kG; curve C, 39.7 kV, 2.0 kG; curve D, 42 kV, 2.06 kG; curve E, 42 kV, 2.12 kG; curve F, 45.4 kV, 2.17 kG. Adapted from Guo *et al.*, 1982.

ties. The instability is driven by azimuthal bunching if $\omega^2 - k_z^2 c^2 > 0$ and by axial bunching if $\omega^2 - k_z^2 c^2 < 0$.

The criterion is valid in all inertial frames because it is in the form of a Lorentz invariant ($\omega^2 - k_z^2 c^2$). It is also independent of the sign of ω/k_z and thus governs both forward and backward waves. Interestingly, the electron energy plays no role in determining the relative importance of relativistic and nonrelativistic effects (reasons discussed in Sec. II.D.1). On the basis of the criterion above, it may be concluded that early observations of stimulated cyclotron emission in fast-wave structures (Table II) could only be explained by the azimuthal bunching mechanism.

E. An experimental verification

The broad range of the slow-wave growth spectrum in Fig. 15(b) presents the tempting possibility of broadband amplification. In the laboratory frame in which the electrons move at velocity v_z , the frequency in Fig. 15(a) will be up-shifted by the amount $k_z v_z$, which corresponds to a significant bandwidth. This led to the study and invention of the slow-wave cyclotron amplifier (Chu, Ganguly, *et al.*, 1981; Chu, Sprangle, and Granatstein, 1982; Guo *et al.*, 1982). The theoretically predicted 3-dB bandwidth (at 20-dB peak gain) can be as high as 44% for a beam velocity spread ($\Delta v_z/v_z$) of 0.7%, but it decreases to 17% as the velocity spread increases to 3.6% (Chu, Ganguly, *et al.*, 1981).

The principle of slow-wave amplification was experimentally verified (Guo *et al.*, 1982) by employing a dielectric loaded waveguide. The measured TE_{01} dispersion curve is shown in Fig. 16(a). In the slow-wave regime, the experiment achieved a maximum small-signal bandwidth of 3.7% with a gain of 32 dB at 6 GHz [Fig. 16(b)]. It was much less than the predicted value of 20%, probably because of a large beam velocity spread. Amplification was also observed in the fast-wave regime at different beam voltages and magnetic fields, showing similar gain and bandwidth. This experiment clearly demonstrated the competition between azimuthal and axial bunching. No gain was observed in a narrow frequency range centered at $\omega/k_z = c$ or $f = 5.8$ GHz [Fig. 16(b)], as predicted by theory. Across this narrow gap, the bunching mechanisms interchanged roles, and the nature of the instability changed qualitatively.

F. Phase bunching and spatial bunching

Azimuthal bunching and axial bunching have often been referred to as phase bunching and spatial bunching, respectively (Antakov *et al.*, 1966; Gaponov, Petelin, and Yulpatov, 1967; Gaponov and Yulpatov, 1967). However, such a characterization is contradicted by the self-consistent field solutions. From Eqs. (62) and (63), we obtain the perturbed charge and current densities (ρ_1 and \mathbf{J}_1),

$$\rho_1 = \frac{1}{4\pi} \nabla \cdot \mathbf{E}_1 = 0, \quad (74)$$

$$\begin{aligned} \mathbf{J}_1 &= \frac{c}{4\pi} \left(\nabla \times \mathbf{B}_1 - \frac{1}{c} \frac{\partial \mathbf{E}_1}{\partial t} \right) \\ &= \frac{iE_0\omega}{4\pi} \left(1 - \frac{k_z^2 c^2}{\omega^2} \right) (\mathbf{e}_x + i\mathbf{e}_y) e^{-i\omega t + ik_z z}. \end{aligned} \quad (75)$$

The ac space-charge density is identically zero [Eq. (74)], indicating pure phase bunching under all conditions. Microscopically, rf forces on the electrons in a common cyclotron orbit generate density and current perturbations. Macroscopically, however, density perturbations in neighboring orbits cancel out, whereas current perturbations constructively superpose to drive the instability. It is also worth noting that Eq. (75) indicates the absence of any axial current despite the occurrence of axial bunching. Axial current cannot be formed in the interaction processes because at every point in space electron transverse velocities are randomly oriented so that there is no net $\mathbf{v}_\perp \times \mathbf{B}_\perp$ axial force. This renders the perturbed current in divergenceless form ($\nabla \cdot \mathbf{J}_1 = 0$) consistent with the absence of ac space charges.

As demonstrated in the uniform-plasma model, the cancellation of ac space charges is an intrinsic property of cyclotron interactions. An actual device may depart considerably from this idealized model. Finite beam size and nonuniformities of the beam and the rf fields can all result in incomplete cancellation of ac space charges. Space-charge effects under such conditions have been

analyzed by Liu and Yang (1981), Lau (1982), and Antonsen, Manheimer, and Levush (1986). In general, spatial bunching in gyrotrons is insignificant compared with that in linear beam devices. Thus far, ac space-charge effects have not been considered a major factor in the design of even the most powerful gyrotrons.

G. Related plasma instabilities

A magnetized plasma medium is extremely rich in wave phenomena. It is conceivable that other plasma waves can be resonantly destabilized by energetic particles in gyrational motion. Indeed, similar instabilities have been predicted to occur in laboratory and space plasmas. They include both electromagnetic and electrostatic waves, and they are driven by ions as well as electrons. For example, azimuthal bunching can destabilize the Bernstein modes in a plasma with anisotropic velocity distribution (Blanken, Stix, and Kuckes, 1969) as well as in an electron beam composed of gyrating electrons (Charbit, Herscovici, and Mourier, 1981; Hirshfield, 1981; Bondeson and Antonsen, 1986; Chen and Chu, 1986; Chu and Lyu, 1986). Chen (1993, 1994) has further shown that the Bernstein mode instability may even be driven by fast ions born in a thermonuclear plasma.

Plasmas confined in a magnetic mirror are characterized by trapped particles with a loss-cone distribution, and thus they are also susceptible to ECM instability. Instabilities are predicted for electromagnetic modes that propagate nearly perpendicularly to the magnetic field, such as the ordinary and extraordinary modes (Freund and Wu, 1976, 1977) or parallel to the field (Lau and Chu, 1983). Wu and Lee (1979) interpreted the auroral kilometric radiation as a space-plasma ECM instability due to trapped electrons in the geomagnetic mirror field. Judging from the diversity of instabilities enumerated here, ECM effects are likely to have an even broader presence in plasmas.

H. Summary and discussion

The electron cyclotron maser has been studied here as a plasma instability. It has been shown that two types of electromagnetic waves can be simultaneously in cyclotron resonance with plasma electrons and that azimuthal and axial bunching destabilize different waves. In a plasma medium in which the two bunching mechanisms exist on an equal footing, their roles and relationship are definitively clarified. The fully self-consistent plasma-physics approach also provides clear proof that cyclotron phase bunching results in insignificant, if any, spatial bunching. This conclusion will have an important bearing on the modeling and operation of gyrotrons (see Secs. V.A, V.C.1, and VI.G).

V. THE ELECTRON CYCLOTRON MASER AS A COHERENT RADIATION SOURCE

Motivated by myriad application needs for powerful millimeter and submillimeter waves (Fig. 17), intensive

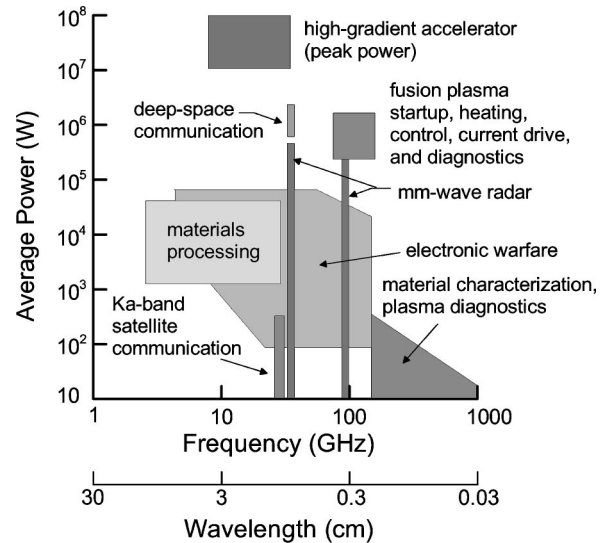
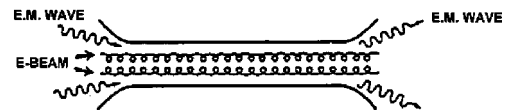


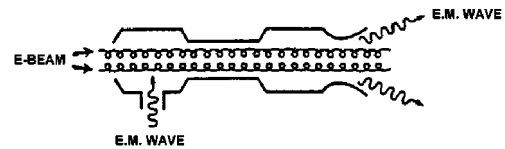
FIG. 17. Current and potential applications of high-power millimeter/submillimeter waves.

research and development efforts have been directed toward the implementation of the ECM as a coherent radiation source. The resulting devices, called gyrotrons, assume a number of forms to meet specific requirements. Interaction structures of four basic types of gyrotrons, all of which support fast waves, are sketched in

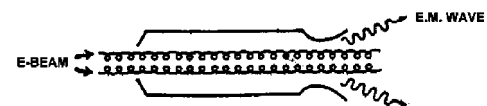
(a) Gyrotron traveling-wave tube amplifier



(b) Gyroklystron amplifier



(c) Gyromonotron oscillator



(d) Gyrotron backward-wave oscillator

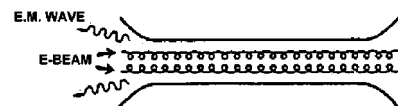


FIG. 18. Interaction structures of four basic types of gyrotrons: (a) The gyro-TWT amplifier features amplitude and phase control over a broad bandwidth. (b) The gyroklystron amplifier has a narrower bandwidth than the gyro-TWT, but better stability property and hence greater power capability. (c) The gyromonotron oscillator produces the highest average power. (d) The gyro-BWO features continuous frequency tunability.

Fig. 18. The cross section of the waveguide or resonant cavity is either constant or slightly nonuniform. To allow high power extraction, the beam-generated wave is usually coupled out through an open end.

The ECM instability is driven by a hollow electron beam consisting of helically moving electrons. The electrons are nearly monoenergetic with a pitch-angle spread. As can be seen in the synchronism condition [Eq. (8)], deleterious effects (on the interaction efficiency, for example) of the spread in v_z are magnified by the propagation constant k_z . This favors operation near the cutoff frequency for maximum tolerance to the electron velocity spread.

Resonant interactions in the rf structure are shown in Fig. 19. The hyperbolic line represents the dispersion relation of a typical waveguide mode. For a resonant cavity, boundary conditions at both ends restrict k_z to a set of discrete values. Resonant frequencies are thus found at discrete points on the hyperbolic line. The straight lines represent synchronism conditions for different magnetic fields. A resonant interaction can, in principle, take place at any intersecting point between the mode line and the synchronism line. As can be seen in the figure, the operating points of the four types of gyrotrons are all close to the cutoff frequency.

Following a brief introduction to device modeling, we present a general discussion of the operating principles, development status, and applications of the four basic types of gyrotrons.¹² More specialized topics will be addressed in subsequent sections.

A. Gyrotron modeling

The rf fields of the gyrotron modes are predominantly in the transverse direction. The basic theories developed in Secs. II and IV for the plane-wave model can therefore serve as a useful basis for the physics discussion to follow. However, more elaborate formalisms¹³ are required for self-consistent evaluations of wave frequency, field profile, and saturation amplitude for specific devices. As discussed in Sec. IV.F, there is negligible spatial bunching in cyclotron interactions. This permits the neglect of ac space-charge fields and the adoption of the transverse field profile of the unloaded interaction structure, in single-mode approximation or as an eigenmode expansion. The dc electric and magnetic fields of the electron beam are normally negligible. With the electron

¹²For reviews of gyrotrons and their applications, see Edgcombe (1993), Gaponov-Grekhov and Granatstein (1994), Gol'denberg and Litvak (1995), Gold and Nusinovich (1997), Granatstein *et al.* (1997, 2001), and Felch *et al.* (1999).

¹³See, for example, Gaponov, Petelin, and Yulpatov (1967), Sprangle and Manheimer (1975), Sprangle and Drobot (1977), Lindsay (1981), Caplan, Lin, and Chu (1982), Ganguly and Ahn (1982, 1984), Fliflet (1986), Ginzburg, Nusinovich, and Zavolsky (1986), Kuraev *et al.* (1988), Chen and Wurtele (1991), Botton *et al.* (1998), Lin and Lin (1998), and Chu *et al.* (1999). In particular, the paper by Fliflet (1986) contains a good survey of the early literature.

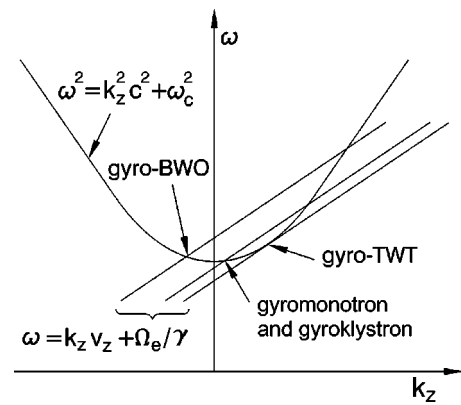


FIG. 19. ω vs k_z diagram showing the intersection point between the mode line and the beam-wave synchronism lines for different types of gyrotrons. ω_c denotes the cutoff frequency of the waveguide. For the resonant rf structures employed in the gyromonotron and gyroklystron, k_z assumes discrete values.

beam treated as an ac current source, the axial and temporal dependence of the rf fields can then be self-consistently evaluated from the set of wave and electron-dynamical equations.

While the concise field expressions of an idealized interaction structure often allow an analytical solution in the linear regime, investigations of practical devices invariably employ a steady-state or time-dependent code. Particle tracing has been the most commonly employed numerical technique. Full-scale particle simulations may also be required to handle problems involving multiple modes or more complex geometry. Calculations for this and subsequent sections are based on one or more of these approaches, as the case demands. Literature on the formalism and numerical tools will be cited where results are presented.

B. The gyrotron traveling-wave amplifier

1. Principle of operation—Convective instability

The gyro-TWT serves as a good example of the transformation of an ECM from a plasma instability to a practical device, as is illustrated in Fig. 20. In the plasma, electrons assume the dual role of providing the fast-wave medium and driving the instability. For a gyro-TWT, a circular waveguide replaces the infinite plasma as the fast-wave medium. A tenuous electron beam is then injected into the waveguide for the sole purpose of driving the ECM instability.

As in the plasma, the ECM instability in a gyro-TWT is characterized by a dispersion relation,¹⁴ which predicts

¹⁴Dispersion relations for gyro-TWT's have been derived by many authors. See, for example, Friedman *et al.* (1973), Ott and Manheimer (1975), Sprangle and Drobot (1977), Chu *et al.* (1979, 1980), Edgcombe (1980), Choe and Ahn (1981), Lau (1982), Lindsay, Lumsden, and Jones (1982), Chu and Lin (1988), and Chen and Wurtele (1991).

ECM instability

Gyro-TWT

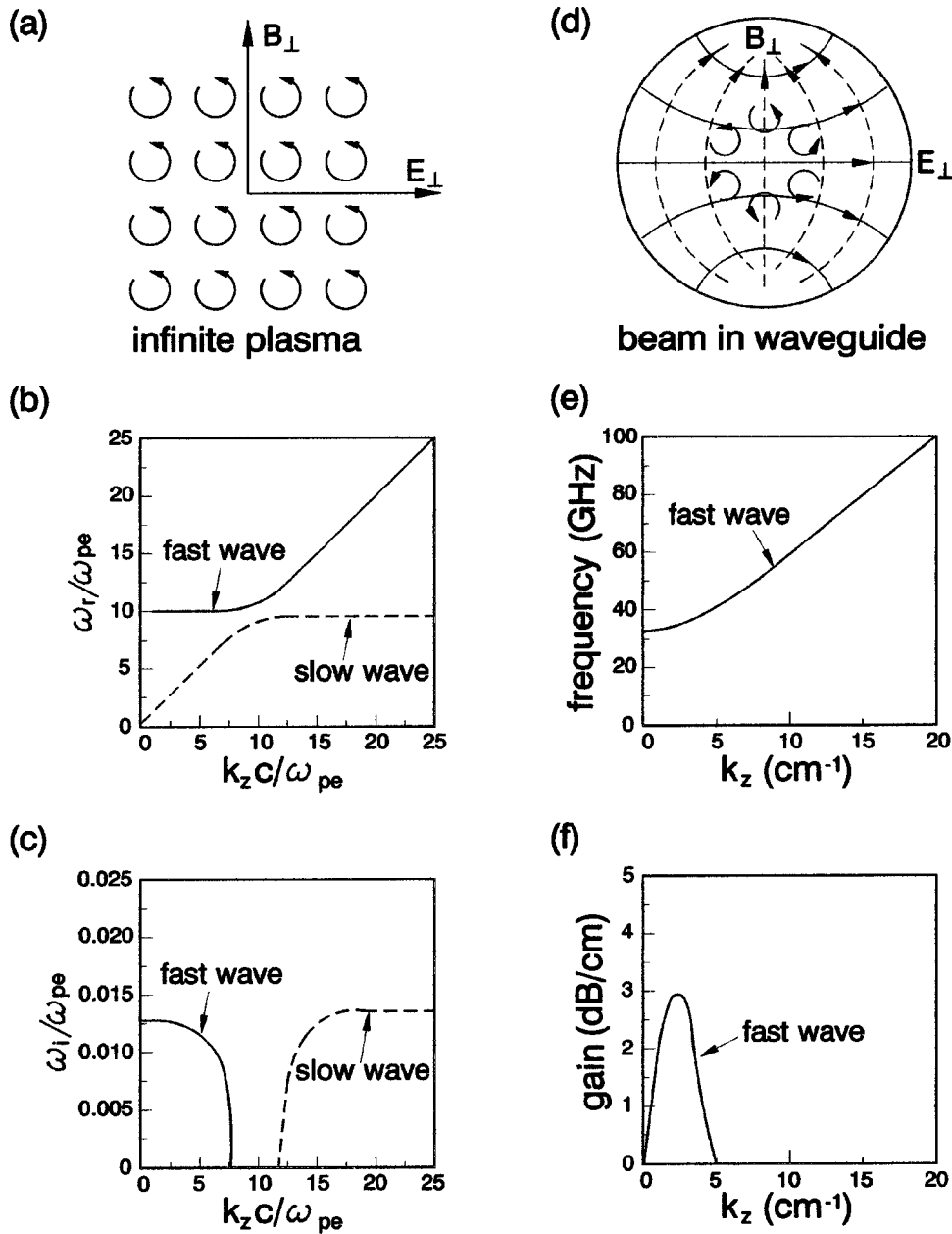


FIG. 20. Comparison of the ECM as a plasma instability [(a)–(c)] and as a radiation source [the gyro-TWT, (d)–(f)] in terms of the dispersive media [(a) and (d)], dispersive properties [(b) and (e)], and growth spectra [(c) and (f)]. The TE₁₁-mode dispersion curve shown in (e) is for a waveguide radius of 0.266 cm.

how an initial disturbance will grow. Instabilities are generally classified into two types: convective and absolute.¹⁵ Operation of the gyro-TWT is based on a convective instability. The input wave is amplified while propagating forward with the beam. Thus, in the steady state, the wave amplitude increases along the axis but

maintains a constant value at any fixed point in space. The device is zero-drive stable in the sense that there is no output power without an input signal. We may therefore define an overall gain (G) in terms of the input power (P_{in}) and the output power (P_{out}),

$$G = 10 \log_{10}(P_{out}/P_{in}) \text{ dB.} \tag{76}$$

2. Backward-wave oscillations—Absolute instability

The dispersion relation predicts a linear gain over a finite bandwidth [Fig. 20(f)]. At a sufficiently high beam

¹⁵Plasma-physics criteria for the classification of absolute and convective instabilities can be found in Sturrock (1958), Briggs (1964), and Stix (1992).

current, the gain spectrum can extend into the negative k_z region. A noise-level disturbance will then be amplified in the backward direction, serving as a feedback to bunch incoming electrons (further discussed in Sec. V.E.1). The disturbance can thus grow locally and spread out in both directions to result in self-oscillations. An instability of this type, characterized by growth at every spatial point, is referred to as an *absolute instability*. Care must be exercised in the interpretation of a numerically evaluated gain spectrum. The analytical threshold conditions for an absolute instability are derived by Lau *et al.* (1981a) and Davies (1989). A graphical method for identifying an absolute instability is presented by Chu and Lin (1988). When the instability turns absolute, the tube is no longer zero-drive stable, and self-oscillations can severely interfere with its performance. For this reason, the operating point of a gyro-TWT is always chosen to be near the grazing intersection (Fig. 19) in order to be farthest away from the backward wave.

There are additional, and often more serious, sources of unwanted oscillations. Intersections of the synchronism line and its harmonics with other mode lines in the backward-wave region are potential sources of absolute instabilities (backward-wave oscillations). Oscillations may also result from regenerative amplification due to end reflections. Competition from these oscillations and methods for their suppression will be analyzed in detail in Sec. VI.A.

3. Status and applications

Traveling-wave amplification via the ECM instability was studied early by Gaponov (1959a, 1959b) and demonstrated in the mid 1960s in a crossed-field device in which the electrons moved in cycloidal orbits (Antakov *et al.*, 1966, see also Sec. III.A). The gyro-TWT in its present form (Granatstein *et al.*, 1980) evolved from a proof-of-the-principle demonstration employing an intense relativistic electron beam (Granatstein *et al.*, 1975). Theoretical studies (Ott and Manheimer, 1975; Sprangle and Manheimer, 1975; Sprangle and Drobot, 1977; Chu *et al.*, 1979, 1980; Lau *et al.*, 1981a, 1981b) provided the additional momentum for its development into the tube configuration at the Naval Research Laboratory (NRL) (Barnett *et al.*, 1979, 1980; Seftor *et al.*, 1979) and Varian Associates (Symons *et al.*, 1979, 1981; Ferguson and Symons, 1980). Measured amplitude and phase modulation coefficients, spectral purity, and phase linearity of a C-band gyro-TWT (Ferguson, Valier, and Symons, 1981) compared favorably with a coupled-cavity TWT. However, the noise figure (above thermal) of ~ 50 dB was estimated to be 12–15 dB higher than that of a coupled-cavity TWT operating at similar power levels. Bandwidth broadening with a tapered waveguide was also studied in theory (Chu, Lau, *et al.*, 1981; Lau and Chu, 1981) and experiment (Barnett *et al.*, 1981). The gyro-TWT experiments during this period were reviewed by Symons and Jory (1981) and Granatstein, Read, and Barnett (1984). While these pioneering ex-

periments demonstrated the principle of the gyro-TWT, research work subsided for a number of years due to severe stability problems.

A new round of international research activities began in the late 1980s, all with emphasis on the fundamental issues of stability and strong theoretical support. The National Tsing Hua University group in Taiwan conducted a systematic investigation of mode competition and suppression, which culminated in a 35-GHz gyro-TWT experiment producing 93-kW saturated output power at 70-dB stable gain. These experiments will be discussed further in Sec. V. The UCLA/UC Davis team pursued the physics and technology of harmonic interactions, with an impressive demonstration of amplification at the eighth cyclotron harmonic (Furuno *et al.*, 1989). A second-harmonic experiment (Wang, McDermott, and Luhmann, 1995, 1996) produced the highest gyro-TWT output power to date (207 kW at 16.7 GHz) for a moderately energetic electron beam. The current research focus of the UC Davis group is on a W-band gyro-TWT (McDermott *et al.*, 2002).

The NRL group, on the other hand, launched a research effort focused on the tapered gyro-TWT, producing a record bandwidth of 33% centered at 34 GHz (Park *et al.*, 1991, 1994, 1995). A separate NRL effort was directed at gyro-TWT's, driven by an intense relativistic electron beam, which achieved 20-MW peak power at 35 GHz (Gold *et al.*, 1991). Recently, a Russian and United Kingdom team developed a helically corrugated interaction structure (Denisov, Bratman, Gross, *et al.*, 1998). This novel circuit provides the important advantages of broadband operation and relative insensitivity to electron velocity spread, as has been demonstrated by Denisov, Bratman, Phelps, and Samsonov (1998) and Bratman *et al.* (2000). More recently, an MIT group built a 140-GHz gyro-TWT employing a confocal waveguide for high-order-mode operation. This quasi-optical circuit promises high-average-power operation deep in the millimeter-wave region. The initial test produced 30 kW peak power in HE_{06} -mode operation with a gain of 29 dB and an unsaturated bandwidth of 2.3 GHz (Sirigiri, Shapiro, and Temkin, 2003).

By employing a nonresonant interaction structure [Fig. 18(a)], the gyro-TWT features broad instantaneous bandwidth [Figs. 20(e) and (f)], which makes it attractive for radar and communication applications. The millimeter-wave radar provides higher resolution than centimeter-wave radar and penetrates deeper than optical radar under foggy and smoky conditions. The general outlook for millimeter-wave radars is discussed by Skolnik (2002). The angular spread of electromagnetic waves scales inversely with the antenna diameter. In the U.S. space program, for example, deep-space communications currently employ a carrier frequency of ~ 10 GHz. With the antenna diameter (~ 64 m) approaching the mechanical limit, significant improvement in directivity can only be achieved with a millimeter-wave transmitter. Another candidate for millimeter-wave transmitters, the gyrokystron amplifier, is discussed below along with its applications.

C. The gyrokystron amplifier

1. Principle of operation—Ballistic bunching and distributed interaction

The gyrokystron (Antakov *et al.*, 1967) is a narrow-band amplifier that is both similar to and different from the conventional klystron. Multiple cavities are commonly employed to increase the gain; however, the principle can be illustrated with a two-cavity model [Fig. 18(b)]. The electrons are energy modulated in the first cavity by the input signal and are azimuthally bunched in the cyclotron phase angle. The resulting (transverse) ac beam current continues to grow in the drift region. Upon entering the second cavity, it drives a large-amplitude oscillation from which the output power is extracted.

As discussed in Sec. IV.F, phase bunching in cyclotron interactions produces insignificant ac space charges. Consequently the drift region is virtually free of ac forces and the electrons are ballistically (or inertially) bunched in their independent trajectories. Ballistic bunching also takes place in a conventional klystron, but in a more complicated manner. The electrons are velocity modulated by cavity rf fields in the axial direction. Subsequent ballistic bunching results in axial density modulation. The ac space-charge forces will then set off plasma waves in the drift region (Gewartowski and Watson, 1965, Chap. 9; Gilmour, 1986, Chap. 9). Thus the electrons are bunched to the maximum density that the space-charge repulsion forces allow.

In further contrast, energy extraction is distributed over the length of the gyrokystron cavity, whereas it is concentrated in the narrow gap(s) of the klystron cavity (Slater, 1950, p. 232). The action will not be reversed despite a typical electron transit time of several wave periods. This is possible because the electrons are in cyclotron resonance with a traveling-wave component of the cavity mode. The total phase variation of the wave, as experienced by the electron in traversing the cavity, is given by the *electron transit angle* (Θ) defined as

$$\Theta = (\omega - k_z v_{z0} - \Omega_e / \gamma_0) \tau, \quad (77)$$

where τ is the electron transit time at the initial axial velocity (v_{z0}), $k_z > 0$ for the forward wave, and $k_z < 0$ for the backward wave. In terms of the detuning factor [Eq. (25b)], we can simply write $\Theta = \varepsilon \tau$.

Under the synchronism condition, the transit angle remains small ($|\Theta| < \pi$) even when $\omega \tau \gg \pi$. Long interaction

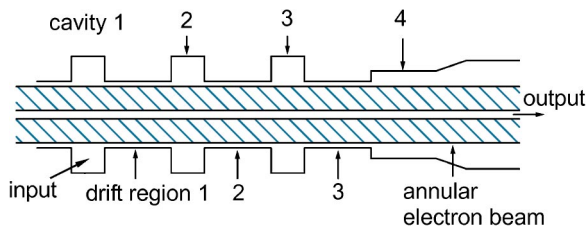


FIG. 21. Schematic of a 30-MW, 10-GHz, four-cavity gyrokystron design. Dimensions are given in Table III. From Chu *et al.*, 1985.

TABLE III. Parameters of the gyrokystron interaction structure.

	Mode	Q_L	f_0 (GHz)	Length (cm)	Radius (cm)
Cavity 1	TE ₀₁₁	300	10	2.1	2.61
First drift region				4.5	1.50
Cavity 2	TE ₀₁₁	300	10	2.1	2.61
Second drift region				4.5	1.50
Cavity 3	TE ₀₁₁	300	10	2.1	2.61
Third drift region				4.5	1.50
Cavity 4	TE ₀₁₁	100	10	3.0	2.11

time reduces the required field strength. This gives the gyrokystron significantly greater power-handling capability than the klystron. However, the gyrokystron efficiency is generally lower by comparison, because only the transverse electron energy is free for rf power generation.

2. A design example

A new generation of particle accelerators, such as TeV-level linear colliders, are being planned for high-energy physics research. To make the size and cost manageable, more powerful microwave amplifiers operating at shorter wavelengths are required to generate the high accelerating field. The gyrokystron provides an ideal candidate rf source for such applications (Granatstein and Lawson, 1996).

Here, we illustrate the ultrahigh-power capability of gyrokystrons with a 30-MW, 10-GHz design example shown in Fig. 21 (Chu *et al.*, 1985). The dimensions of the four-cavity interaction structure and the beam parameters are listed in Tables III and IV, respectively. The ideal cavity field profile is assumed. The field amplitude is self-consistently calculated, including beam-loading effects on the cavity resonant frequency and bandwidth. The predicted performance is given in Table V. Efficiency degradation due to electron velocity spread is shown in Fig. 22. The transfer curve (P_{out} vs P_{in}) is plotted in Fig. 23 for a beam axial velocity spread of 10%. Table VI shows the large-signal amplitude and phase modulation sensitivities with respect to the operating parameters. In order to achieve a phase stability of

TABLE IV. Gyrokystron electron-beam parameters.

Voltage	500 kV
Current	200 A
Power	100 MW
Velocity ratio ($v_{\perp 0} / v_{z0}$)	1.5
Velocity spread ($\Delta v_{z0} / v_{z0}$)	10%
Inner radius	0.12 cm
Outer radius	1.45 cm
Larmor radius	0.44 cm

TABLE V. Gyrokystron small- and large-signal predicted performance.

	Small signal	Large signal
Static magnetic field (kG)	5.65	5.65
Center frequency (GHz)	10.02	10.02
Peak power (MW)		28.1
Peak gain (dB)	63.1	56.2
3-dB bandwidth (%)	0.10	0.21
Efficiency (%)		28.1

$\pm 5^\circ$, for example, the static magnetic field and the beam voltage need to be stable within 0.1% and 0.2%, respectively.

In the distributed interaction, energy modulation, electron bunching, and power conversion all occur in a single cavity. Hence each individual cavity can oscillate by itself, the prevention of which becomes an important consideration in the gyrokystron design. Short-length cavities have been chosen to ensure stability. As an example, Fig. 24 plots the start-oscillation current (I_{st} , discussed further in Sec. V.D.2) for different modes in the output cavity. It can be seen that, at the operating beam current of 200 A and the design magnetic field of 5.65 kG, the output cavity is zero-drive stable.

3. Status and applications

Early Soviet gyrokystron development was aimed at radar applications. The results, reviewed by Gol'denberg and Litvak (1995), were not published until much later. Two phase-matched, *Ka*-band gyrokystrons are currently in operation to power a megawatt radar station for tracking orbiting objects around the earth (Tolkachev *et al.*, 2000).

In the United States, exploratory studies were conducted at Varian Associates (Jory *et al.*, 1977) and NRL (Ganguly and Chu, 1981; Arfin and Ganguly, 1982; Bollen *et al.*, 1985). The design in Table V and its demonstration (Lawson *et al.*, 1991) provided a strong impetus for subsequent gyrokystron activities aimed at accelera-

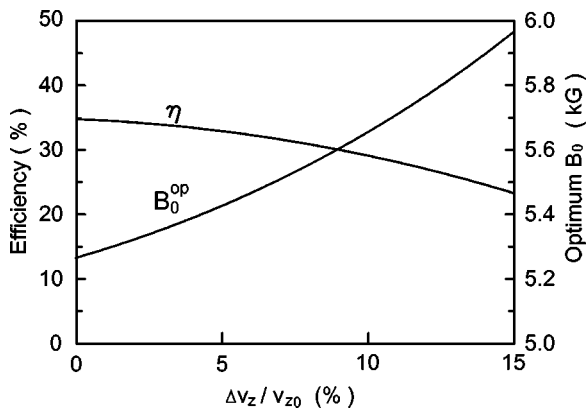


FIG. 22. Calculated gyrokystron efficiency as a function of the electron velocity spread. The optimum magnetic field varies with the velocity spread. From Chu *et al.*, 1985.

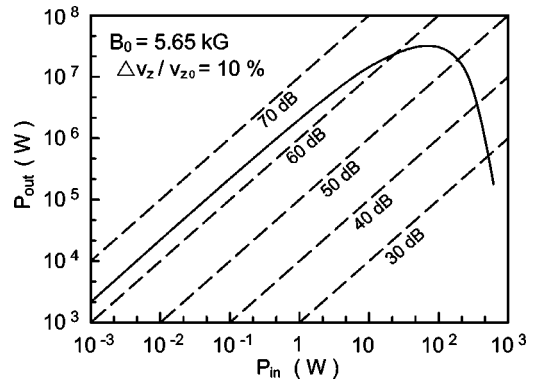


FIG. 23. Calculated gyrokystron output power vs input power for the parameters shown in Tables IV and V. From Chu *et al.*, 1985.

tor and radar applications. A later experiment employing coaxial cavities achieved 75 MW peak power in the *X* band (Lawson *et al.*, 1998). At the same time, a conventional klystron developed at the Stanford Linear Accelerator Center produced 50-MW peak power in the same band (Phillips and Sprehn, 1999). At frequencies beyond the *X* band, however, the gyrokystron appears to be a better choice. For example, a 50-MW, 30-GHz version is under development for rf structure testing and conditioning of the Compact Linear Collider at CERN (Blank, Borchard, *et al.*, 2002). *W*-band gyrokystrons capable of 100-kW peak power at a 10% duty factor (Fig. 25, Danly *et al.*, 2000, Blank, Felch *et al.*, 2002) have also been developed and integrated into the NRL WARLOC radar system (Ngo *et al.*, 2002). Novel applications requiring more powerful gyrokystrons have been envisioned, such as radar tracking and cataloging of centimeter-size space debris (Manheimer, Mesyats, and Petelin, 1994). The measured noise levels of a 200-kW, *Ka*-band gyrokystron are similar to those of conventional klystrons (Calame *et al.*, 2000; see also Antonson *et al.*, 2001; Manheimer, 2001).

D. The gyromonotron oscillator

1. Principle of operation—Reflective feedback

As just discussed, distributed interaction allows a cavity to oscillate by itself. Self-oscillation in a single cavity forms the basis of a high-average-power device called the gyromonotron [Fig. 18(c), Gaponov *et al.*, 1965, 1967]. To build up and sustain the oscillation, a feedback loop is required. In the gyromonotron, it is provided by

TABLE VI. Gyrokystron large-signal predicted amplitude modulation (AM) and phase modulation (PM) sensitivities.

	AM sensitivity	PM sensitivity
Static magnetic field	0.18 dB/%	51.1°/%
Beam voltage	0.13 dB/%	25.8°/%
Beam current	0.07 dB/%	2.9°/%
Electron pitch angle	0.34 dB/degree	6.1°/degree

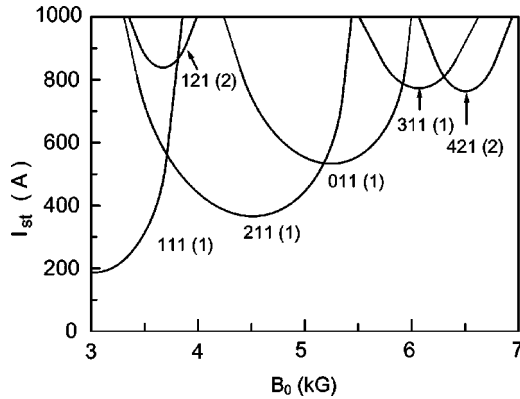


FIG. 24. Calculated start-oscillation current (I_{st}) vs the magnetic field (B_0) for modes with low I_{st} in the output cavity of Fig. 21. Mode indexes are labeled for each curve and the cyclotron harmonic number is indicated in parentheses. Dimensions of the cavity are given in Table III (cavity 4). Electron-beam parameters are given in Table IV. All modes have the same axial index of 1 and are assumed to have the same loaded Q value of 100. From Chu *et al.*, 1985.

end reflections. Consider the two traveling-wave components of a resonant mode. The forward wave turns into a backward wave upon reflection at one end, while the backward wave reverses to a forward wave at the other end. This results in continuous wave circulation in a closed loop. If the power gained from the beam exceeds the power lost, the circulating wave will be repetitively pumped by the electron beam from the noise level to an equilibrium amplitude. This may be regarded as a feedback process because fresh electrons are interacting with a wave generated by early electrons. By comparison, wave growth in the gyro-TWT is a single-path process.

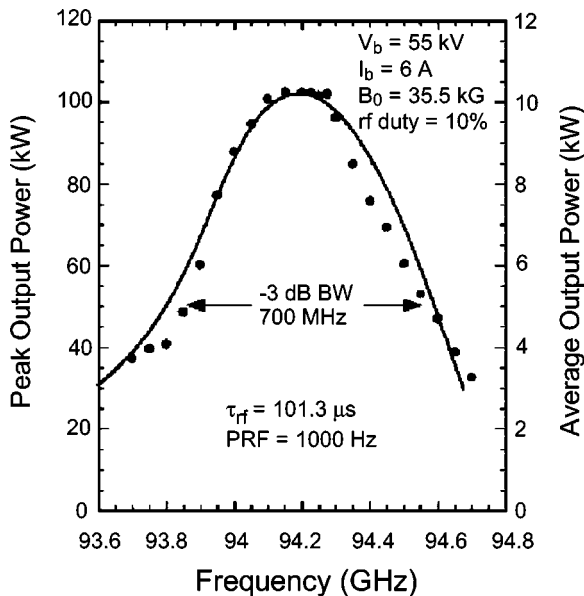


FIG. 25. Measured peak and average output powers (dots) of a five-cavity gyrokystron amplifier. The theoretical prediction (solid curve) assumes an $\alpha (=v_{\perp 0}/v_{z0})$ value of 1.2 and an rms velocity spread of 3%. From Blank, Felch, *et al.*, 2002.

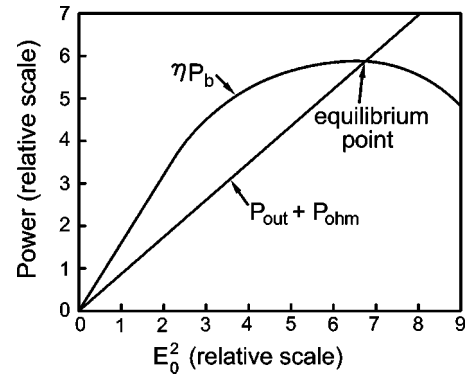


FIG. 26. Schematic illustration of the beam-generated power (ηP_b) and the sum of output and Ohmic powers ($P_{out} + P_{ohm}$) as functions of the square of the field amplitude (E_0^2). E_0 increases when $\eta P_b > P_{out} + P_{ohm}$ and decreases when $\eta P_b < P_{out} + P_{ohm}$. Hence a stable equilibrium is maintained at the intersection of the two curves, which is usually designed to occur at or near the maximum efficiency point.

The growth time is limited by the wave transit time. An input wave well above the noise level is thus required in order to generate significant output power. On the other hand, this allows amplitude and phase control of the output wave.

2. Power balance, oscillation threshold, and equilibrium field

As the electron beam deposits energy into the cavity fields, there are also power losses through output coupling (P_{out}) and wall dissipation (P_{ohm}). The power versus E_0^2 curves in Fig. 26 demonstrate the existence of a threshold condition for self-oscillation. At any level of the rf field amplitude (E_0), both P_{out} and P_{ohm} scale as E_0^2 . Their sum thus appears as a straight line in Fig. 26, the slope of which depends upon the loaded quality factor Q_L . The beam-generated power can be written as ηP_b , where η is the interaction efficiency and P_b is the beam power. The interaction efficiency scales as E_0^2 in the linear regime [Eq. (37)], and P_b is assumed to remain constant during the field buildup. Hence the beam-generated power also appears as a straight line in the linear stage, with a slope proportional to P_b . The threshold beam power (P_b^{th}) is the power at which the two slopes are equal. When P_b exceeds the threshold value, there is more power generated than lost, and consequently E_0 starts to grow.

Returning to the basic model of Sec. II, we may estimate an optimum magnetic field for the startup of oscillation. As shown in Figs. 7 and 8, both linear and nonlinear efficiencies reach their first peak on a synchronous time scale, or when $\epsilon t \cong \pi$. Because ϵt (a phase angle) is a frame-independent quantity, its optimum value in the beam frame transforms into an optimum electron transit angle in the lab frame:

$$\Theta_{op} \cong \pi. \tag{78}$$

Equation (78) is an approximate condition applicable to both linear and nonlinear regimes, although the pre-

cise values of Θ_{op} in the two regimes are slightly different. With the beam parameters and cavity dimensions fixed, the magnetic field is the only free parameter in Θ . Thus, for each mode, condition (78) specifies an optimum magnetic field for the lowest oscillation threshold.¹⁶ Given the beam voltage, the threshold beam power can be converted into a more convenient figure of merit—the *start-oscillation current* (I_{st}). Figure 24 illustrates the dependence of I_{st} on the magnetic field for a number of low-order modes. These modes are separated by differences between their optimum magnetic fields, while neighboring modes partially overlap because of finite resonant width. Higher-order modes will be more closely spaced in the chart. However, overlapping modes can be separated by interaction strength (hence I_{st}) if the beam is positioned in favor of the operating mode [see Eq. (58)]. The I_{st} vs B_0 chart provides a useful guide for mode selection. To minimize the possibility of mode competition, the operating mode should be sufficiently separated from the other modes in B_0 or I_{st} .

The start-oscillation current is a linear property. Linearly, the electrons become more tightly bunched in a longer interaction structure. Hence I_{st} decreases with increasing structure length (L). As discussed in Sec. II.E, cyclotron emission and absorption both take place in the interaction processes, and they scale differently with the interaction time (or L). As a result, I_{st} depends upon L in a complicated manner, rather than obeying a simple scaling law. A specific example will be considered in Sec. VII.B for the gyrotron backward-wave oscillator.

Figure 26 also shows how an equilibrium state is reached and stably maintained. The field amplitude (E_0) grows as long as $\eta P_b > P_{out} + P_{ohm}$. However, the growth cannot continue indefinitely. As E_0 rises and the interaction becomes nonlinear, the efficiency will level off and eventually decrease. This causes the ηP_b line to bend downward and intercept the $P_{out} + P_{ohm}$ line at the point where $\eta P_b = P_{out} + P_{ohm}$ (Fig. 26). An equilibrium state is thus established and E_0 will no longer increase. As can also be seen in Fig. 26, the equilibrium state is stable against E_0 fluctuations. The operating beam current is usually chosen so that the equilibrium field yields the maximum efficiency, as in Fig. 26.

3. Status and applications

The gyromonotron oscillator is the most mature type of gyrotron. Pioneering work was conducted at the Institute of Applied Physics (IAP; see Sec. III.A). Highlights of early accomplishments included cw operations at the second cyclotron harmonic, which produced 1.5 kW at 326 GHz (Zaytsev *et al.*, 1974) and 10 kW at 34 GHz (Kisel' *et al.*, 1974), both in low-order-mode operation. These demonstrations proved the viability of the

¹⁶Higher-order axial modes are rarely used; however, they can be excited in two regions of the magnetic field through either forward- or backward-wave coupling (Chang *et al.*, 2003).

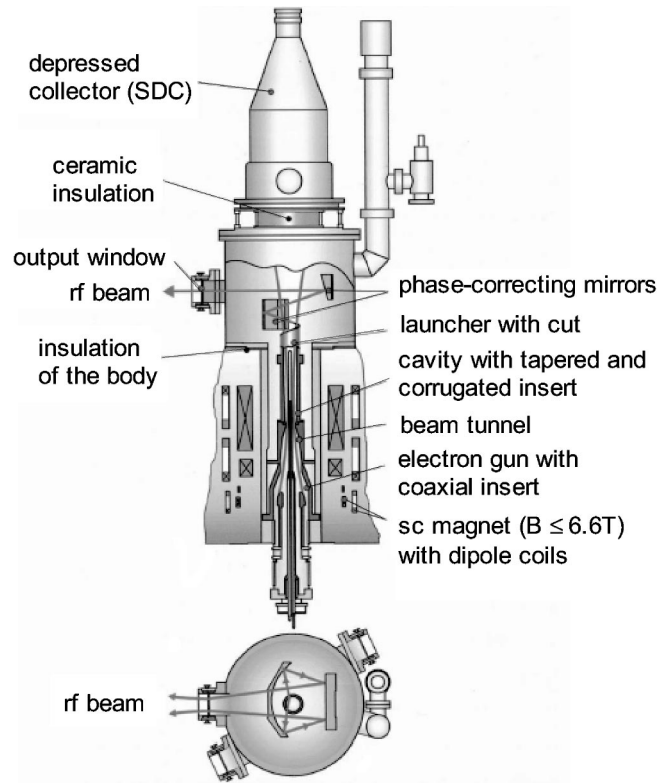


FIG. 27. Schematic layout of an 165-GHz, $TE_{31,17}$ -mode, 2.2-MW coaxial gyromonotron. The insert at the bottom shows the quasi-optical output coupling structure. From Piosczyk *et al.*, 2002.

gyromonotron as a powerful source, and its application for fusion plasma heating generated a strong development program at IAP. Plasma heating requires high power; thus high-order modes must be utilized. The whispering gallery modes were found to be more stable against mode competition and to possess field profiles compatible with a large-radius annular electron beam (Bykov *et al.*, 1975). By the late 1970s, fundamental harmonic gyromonotrons at operating frequencies of up to 100 GHz and peak power levels up to 1 MW (Andronov *et al.*, 1978) had been developed for tokamak heating (Alikaev and Suvorov, 1994). The early history of the Soviet gyromonotron work is reviewed by Flyagin *et al.* (1977), Andronov *et al.* (1978), Symons and Jory (1981), Flyagin and Nusinovich (1988), and Gol'denberg and Litvak (1995).

The successes of the Soviet work stimulated major gyromonotron development activities in the U.S., France, China, Japan, Switzerland, and Germany for a variety of fusion-oriented applications such as plasma startup, heating, current drive, instability control, and plasma diagnostics (Luce, 2002). Gyromonotrons are now commercially available (reviewed by Felch *et al.*, 1999). These devices produce megawatt output power in long-pulse or cw operation in the frequency range 75–170 GHz, which represents an advance more than three orders of magnitude beyond the capability of other tube types. A coaxial-cavity version recently developed at the Institute for Pulsed Power and Microwave Technology

in Germany generated peak power as high as 2.2 MW at 165 GHz in TE_{31,17}-mode operation (Fig. 27, Piosczyk *et al.*, 2002). Medium-power gyromonotrons at lower frequencies have also found applications in materials processing (Bykov and Semenov, 1994; Link *et al.*, 1999).

In a different direction, step-tunable gyromonotrons (Brand, 1985) have been developed for research use. As the magnetic field is varied over a broad range, the oscillation jumps from mode to mode, thus generating a broad and usually discrete radiation spectrum. Step-tunable gyrotrons developed at Fukui University, Japan, are capable of delivering submillimeter-wave radiation ranging from hundreds of watts cw at 190 GHz to tens of watts cw at 860 GHz (Idehara *et al.*, 1999). These sources are provided in a user facility dedicated to research on materials characterization, plasma wave scattering, and electron spin resonances (Fekete, Brand, and Idehara, 1994; Timms and Brand, 1996; Idehara *et al.*, 1999). High-power, step-tunable gyromonotrons are also desirable for position-selective heating of fusion plasmas (see, for example, Kreischer and Temkin, 1987).

E. The gyrotron backward-wave oscillator

1. Principle of operation—Internal feedback

The gyrotron backward-wave oscillator [gyro-BWO, Fig. 18(d)] employs a waveguide structure like the gyro-TWT but operates at a point in the ω - k_z diagram where the group velocity is opposite to the beam velocity (Fig. 19). This allows oscillations to build up in an internal feedback loop composed of the forward-moving electron beam and the backward-propagating wave. In accordance with the previous argument, the beam power must exceed a certain threshold to start the oscillation. In the noise fields, the electron beam will be weakly bunched by a resonant backward wave. The bunched electrons impart energy to the wave, which propagates backward toward the beam entrance to generate tighter electron bunches. More and more energy is thus fed to the wave until an equilibrium state is reached. Since the beam and the wave constitute a closed loop, no reflections are required in the buildup process. In addition to frequency tuning by voltage adjustment, as in the conventional BWO, the gyro-BWO can also be tuned through variation of the magnetic field (Fig. 19).

2. Axial modes of the gyro-BWO

In contrast to the gyromonotron, for which each hot mode corresponds to a cold mode, there exists no cold resonant mode in the gyro-BWO interaction structure (basically a waveguide; see the simplest model at the top of Fig. 28). The identities of hot modes must then be determined entirely by the beam-wave interaction. Field-shaping processes, as well as the resultant axial field profile in a gyro-BWO, are therefore fundamentally different from those in a gyromonotron. Referring to Fig. 7 again, successive peaks of the linear efficiency occur at discrete values of ϵt . Applying Fig. 7 to gyro-BWO interactions in a waveguide of fixed length, these

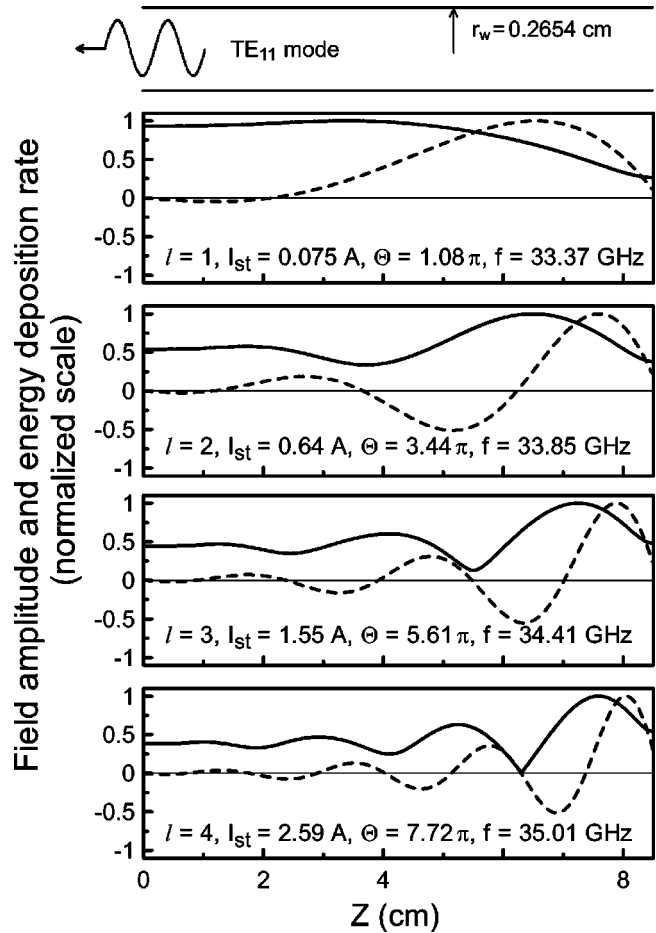


FIG. 28. Model and linear axial modes of a gyro-BWO. Top figure: the gyro-BWO interaction structure (a uniform waveguide). Bottom figures: axial dependence of calculated field amplitude (solid curves) and beam energy deposition rate (dashed curves) of the first four axial modes at their respective I_{st} . $V_b=95$ kV, $\alpha=1.1$, $r_c=0.35 r_w$, and $B_0=14.5$ kG. From Chen *et al.*, 2002.

optimum values of ϵt translate into a set of optimum transit angles approximately written as

$$\Theta_{op} \cong (2l-1)\pi, \quad l=1,2,3,\dots \quad (79)$$

Despite its approximate nature, Eq. (79) exhibits the essential feature—the discreteness—of optimum transit angles. In addition to the magnetic field, the wave frequency is now a free parameter in Θ . Hence, in any given magnetic field, condition (79) specifies a discrete set of frequencies (and the associated k_z). These turn out to be the eigenfrequencies of the gyro-BWO axial modes, as shown by Chen *et al.* (2002). Figure 28 plots the axial profiles of the rf field amplitude and beam energy deposition rate for the first four axial modes at their respective start-oscillation currents. For the fundamental axial mode (Fig. 28, $l=1$ or $\Theta \cong \pi$), the electron beam deposits energy in the wave over its entire passage through the interaction structure, following the initial absorption dip. Each higher-order axial mode is characterized by a step increase in Θ (by $\sim 2\pi$), which results in one more region of negative energy deposition and

hence an amplitude trough of the field (Fig. 28, $l = 2-4$). Thus the order of an axial mode is differentiated by the transit angle or, equivalently, by the number of regions of positive energy deposition. These properties extend to the case of a tapered interaction structure as well.

Note that the field in Fig. 28 represents an amplitude-modulated backward wave, rather than the standing wave of a resonator. This is revealed by the strong correlation between the field profile and the energy-deposition profile. As the wave propagates backward, each field peak and trough occurs precisely at the completion of a positive and negative energy-deposition phase. Higher-order axial modes will be further discussed in Secs. VIII.C and VIII.D in connection with nonlinear issues.

3. Nonlinear properties

As Fig. 28 shows, the interaction dynamics, rather than resonant structure, determine the axial mode profile of a gyro-BWO. Thus the linear and nonlinear field profiles of a gyro-BWO are found to be significantly different (Chen, Chu, and Chang, 2000). The axial field profile contracts nonlinearly as the beam current rises, because the feedback loop shortens with an increased rate of beam energy depletion. This results in stable saturated operation at currents orders-of-magnitude higher than the start-oscillation current (Chang *et al.*, 2001). More studies have revealed that stationary and nonstationary states appear alternately as the beam current rises (Nusinovich, Vlasov, and Antonsen, 2001; Chen *et al.*, 2002; Grudiev and Schunemann, 2002, see also Sec. VIII.D). Nonlinear properties of backward-wave oscillations will be further examined in Secs. VII and VIII.

4. Status and applications

By employing a nonresonant circuit, the gyro-BWO is able to feature continuous frequency tunability by either voltage or magnetic-field adjustment, as was demonstrated early with low-energy electron beams (Pantell, 1959; Schriever and Johnson, 1966) and more recently with moderate-energy (Park *et al.*, 1990; Kou *et al.*, 1993; Basten *et al.*, 1995) and high-energy electron beams (Spencer *et al.*, 1996; Water *et al.*, 1996; Kamada *et al.*, 1998). Theoretical studies of the gyro-BWO first appeared in the mid 1960s in the Soviet literature. These and later theories are reviewed by Nusinovich and Dumbrajs (1996). As discussed in Sec. III.A, the principle of the ECM was first demonstrated in backward-wave oscillations (Pantell, 1959). Thus far, however, the gyro-BWO remains the least-investigated ECM device despite numerous applications that require frequency tunability, such as electronic countermeasures, position-selective plasma heating, spectroscopy, and drivers of ultrahigh-power amplifiers. Some interesting properties of backward-wave interactions have only recently come to light, as discussed above. Further research is war-

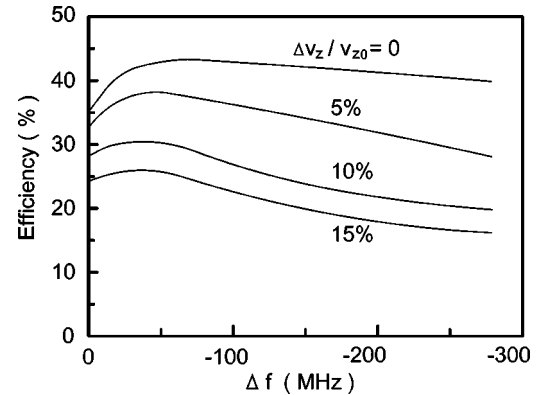


FIG. 29. Calculated efficiency of the gyroklystron (Fig. 21) as a function of the downward tuning of the resonant frequency of the penultimate cavity. The 3-dB resonant width of the cavity is 33 MHz. From Chu, Latham, and Granatstein, 1988.

ranted for a better physical picture of the gyro-BWO and its development into a useful device.

F. Efficiency considerations

Interaction efficiency is a common measure of device quality, in addition to being of utmost importance to high-average-power operation. In Fig. 10, it is shown that the saturated efficiency maximizes at an optimum detuning factor. For cavity interactions in the gyromonotron and gyroklystron, the wave frequency is fixed by the cavity resonance. The magnetic field can thus be adjusted to achieve optimum detuning. However, it is difficult to control the detuning factor for waveguide-based devices. The gyro-BWO oscillation frequency varies in concert with the magnetic field to maintain synchronous interaction. The gyro-TWT gain diminishes with too large a detuning factor. There are also other factors that adversely affect the efficiency of the gyro-TWT and gyro-BWO. The gyro-TWT operates at a frequency farthest away from the cutoff (Fig. 19) and thus is most sensitive to beam velocity spread. The gyro-BWO field is at a high level at the beam entrance, which results in abrupt electron bunching unfavorable for efficient interaction. Largely for these reasons, the interaction efficiency is generally higher for the gyromonotron and gyroklystron (30–50%) than for the gyro-TWT and gyro-BWO (10–30%).

Profiling of the interaction structure (Kisel' *et al.*, 1974; Bykov and Gol'denberg, 1975) or the static magnetic field (see, for example, Chu, Read, and Ganguly, 1980; Read *et al.*, 1982) are common means for efficiency enhancement. Other methods include penultimate-cavity tuning for the gyroklystron and the use of a below-grazing magnetic field for the gyro-TWT (see, for example, Chu *et al.*, 1979). When these methods are applied to amplifiers, they are often at the expense of gain and bandwidth and are effective only for an electron beam with low velocity spread. As an example, Fig. 29 shows the effect of penultimate-cavity tuning (Chu, Latham, and Granatstein, 1988) for the 30-MW, 10-GHz

gyrokystron design shown in Fig. 21. Significant efficiency enhancement (from 36% to 43%) occurs for a cold electron beam, but the benefit fades away as the velocity spread increases. The performance of harmonic gyrotrons is especially limited by the availability of low-velocity-spread, axis-encircling electron beams. In such cases, good electron optics appears to hold the key to dramatic advances.

External to the interaction region, a depressed collector can be used to increase the overall efficiency. In the experiment of Piosczyk *et al.* (2002), for example, a single-stage depressed collector (Fig. 27) resulted in an efficiency increase from 30 to 48 %.

G. Summary and discussion

We have surveyed four decades of active research that has yielded fruitful results in gyrotron physics, modeling, technology, performance, and applications. Present-day modeling capabilities are illustrated by the excellent agreement between theory and experiment shown in Fig. 25, while the tube layout in Fig. 27 serves as an example of the sophistication of the latest technology. By delivering power ranging from tens of watts at ~ 1000 GHz to nearly 100 MW at ~ 10 GHz, the gyrotron has indeed lived up to its promise as a millimeter/submillimeter-wave source of unprecedented capabilities. Looking forward, challenging applications will continue to give fresh impetus to further research and technology development. The full potential of the gyrotron remains to be demonstrated.

VI. GYROTRON TRAVELING-WAVE AMPLIFIER—A STUDY OF MODE COMPETITION

Mode competition in the gyrotron is a physics issue of both academic interest and practical importance. Early studies on this subject were mostly concerned with oscillators (reviewed by Nusinovich, 1999). However, this is a phenomenon more richly manifested in the gyro-TWT than in other device types. Here, to illustrate the general nature of the problem, we present a detailed study of multimode effects in the gyro-TWT and methods for competing mode stabilization.

A. Sources of self-oscillations in the gyro-TWT

In a resonant cavity, ω and k_z assume discrete values, which restricts cyclotron resonance to a narrow magnetic-field range for each mode. In contrast, there are no such restrictions in a waveguide structure. Consequently, electrons in a gyro-TWT can be in simultaneous resonance with a multitude of forward and backward waves in both the fundamental and higher cyclotron harmonics. Furthermore, the amplifying wave, without a feedback mechanism, is at a disadvantage relative to oscillating modes. All of these factors make the gyro-TWT susceptible to a variety of spurious oscillations.

Figure 30 shows the ω - k_z diagram of the TE_{11} and

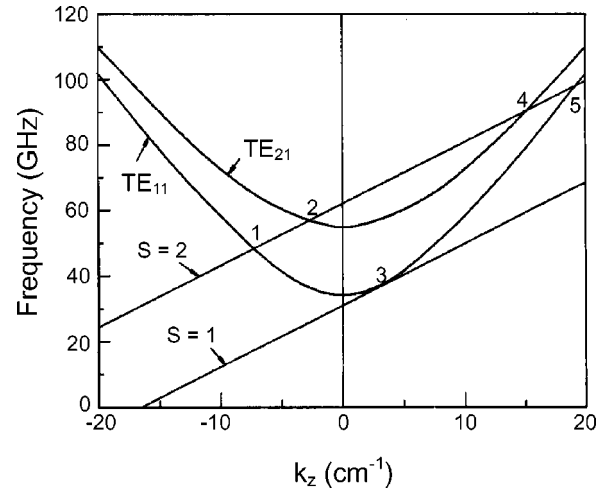


FIG. 30. Frequency vs k_z diagram of a fundamental cyclotron harmonic, Ka -band gyro-TWT based on the TE_{11} -mode convective instability (point 3). Other convective instabilities (points 4 and 5) and possible absolute instabilities (points 1 and 2) due to second cyclotron harmonic interactions are also indicated. This illustration assumes $r_w = 0.2654$ cm, $V_b = 87.75$ kV, $\alpha = 1$, and $B_0 = 12.38$ kG.

TE_{21} modes of a waveguide and the beam-wave synchronism lines at the fundamental ($s=1$) and second ($s=2$) cyclotron harmonics. As discussed in Secs. V.B.2 and V.E.1, interactions involving backward waves (points 1 and 2) will grow locally in an internal feedback loop at sufficiently high beam current. These oscillations belong to the general category of absolute instabilities. Interactions in the forward-wave region (points 3, 4, and 5) normally give rise to convective instabilities, which grow spatially along the path of the electron beam. The gyro-TWT is a complicated case because it exploits a convective instability near the cutoff frequency (point 3), which transitions into an absolute instability when the unstable spectrum extends into the backward-wave region at high beam currents (Chu and Lin, 1988).

The problem of absolute instabilities is compounded by an additional source of oscillation that results from regenerative amplification due to reflections at, for example, the input/output mismatches. This occurs when the tube gain (G) exceeds the sum of the power reflection coefficients at the left and right ends ($R_l + R_r$) plus the cold-circuit attenuation (A) between the ends (all expressed in dB),

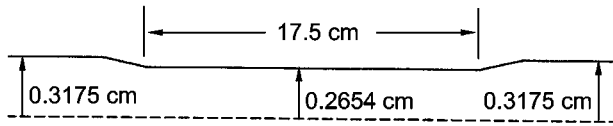
$$G - R_l - R_r - A > 0, \quad (80)$$

where typical values for R_l and R_r are 10–20 dB, corresponding to 10–1% reflection.

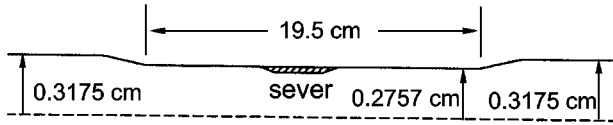
B. Competition between convective and absolute instabilities

We discuss here a series of Ka -band gyro-TWT experiments conducted with three types of interaction structures as shown in Fig. 31, all designed for TE_{11} -mode interaction at the fundamental cyclotron har-

(a) unsevered interaction structure



(b) severed interaction structure



(c) interaction structure with distributed wall losses

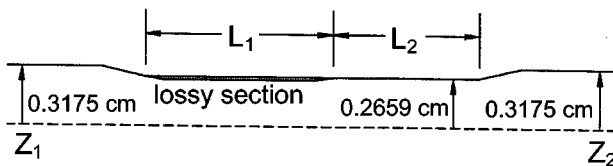


FIG. 31. Schematics of the (a) unsevered, (b) severed, and (c) distributed-loss gyro-TWT circuits employed in experimental investigations. The interaction structure is connected at each end, through a weakly tapered section, to a uniform section of larger radius for broadband input/output coupling through the side walls.

monic (point 3 in Fig. 30). The experimental device (photo shown in Fig. 32) features a pair of dual-port couplers, one at each end, specifically designed to separate the operating mode from the oscillating modes (Barnett *et al.*, 1989; Chang *et al.*, 1999). The TE_{11} wave enters and exits exclusively through one set of input/output ports with 1 dB transmission loss over a band of ~ 3.5 GHz. Good isolation (~ 30 dB) from the other two ports allows very-low-level oscillations of non- TE_{11} modes to be monitored through the extra port at each end without interference from the TE_{11} wave. A superconducting magnet provides the uniform magnetic field in the interaction region. A single-anode magnetron injection gun generates the electron beam with a simulated axial velocity spread of $\sim 5\%$. The TE_{11} output power is measured with a calibrated crystal detector (with an estimated accuracy of $\pm 5\%$) and verified with a calorimeter (agreement within $\sim 5\%$).

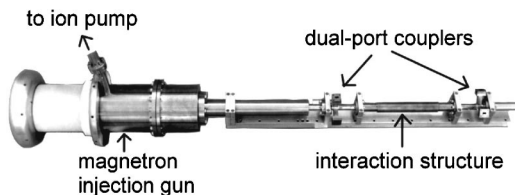


FIG. 32. Photograph of a Ka-band gyro-TWT detached from the superconducting magnet.

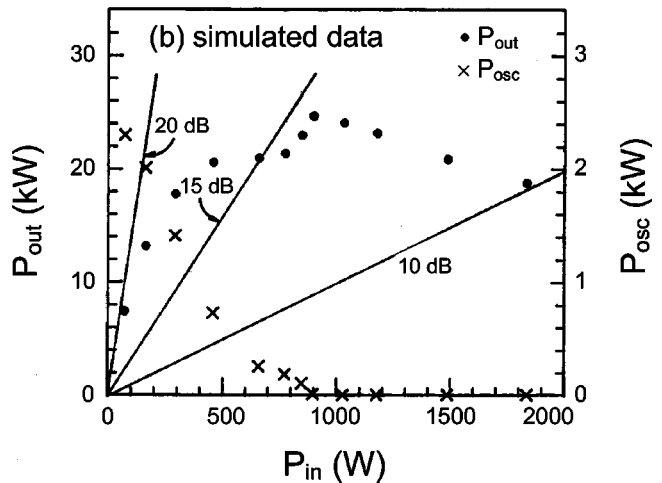
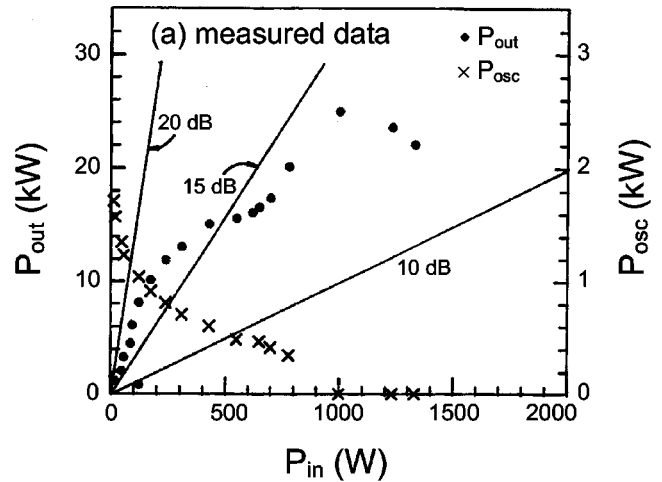


FIG. 33. Competition between absolute and convective instabilities in an unsevered gyro-TWT: (a) \bullet , measured TE_{11} output power and \times , TE_{21} oscillation power vs the TE_{11} drive power; (b) simulation data for the experiment in (a). In both (a) and (b), $V_b = 87.75$ kV, $I_b = 1.25$ A, $r_w = 0.2654$ cm, $L = 17.46$ cm, and $f = 34.7$ GHz. The simulation assumes an electron beam with $\alpha = 1$, $\Delta v_z/v_{z0} = 5\%$ and $r_c/r_w = 0.35$. From Chu *et al.*, 1991.

The unsevered gyro-TWT [Fig. 31(a)] was driven by an 87.75-kV electron beam with the magnetic field (12.38 kG) optimized for high saturated efficiency. Figure 33(a) shows the 34.7-GHz, TE_{11} output power (dots) versus the drive power at a beam current (I_b) of 1.25 A (Barnett *et al.*, 1989). The experiment was found to be susceptible to a second cyclotron harmonic, TE_{21} backward-wave oscillation (point 2 in Fig. 30) at I_b as low as 0.1 A. Output power of the simultaneous TE_{21} oscillation, measured by a calorimeter at the extra upstream port, is also plotted (\times 's). The TE_{21} power measurement has a 3-dB uncertainty because the oscillation frequency (~ 56 GHz) falls outside the range of the Ka-band components. Mode competition is revealed by the strong correlation between the TE_{11} and TE_{21} power levels. The TE_{21} oscillation dominates at zero or small drive powers. The oscillation level decreases steadily and eventually disappears as the drive power is in-

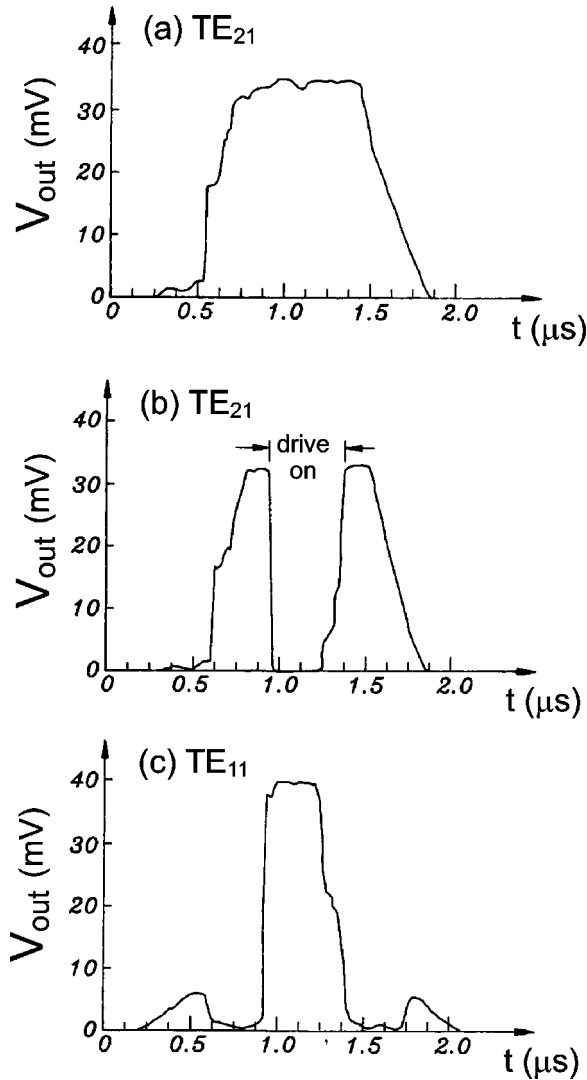


FIG. 34. Oscilloscope traces showing oscillation suppression by a large-amplitude drive wave: (a) TE_{21} oscillation signal at zero drive over the duration of the beam pulse; (b) TE_{21} oscillation signal with a 1-kW, TE_{11} drive pulse applied in the middle of the beam pulse; (c) TE_{11} output signal during application of the 1-kW drive wave. Other experimental parameters are given in Fig. 33. From Chu *et al.*, 1991.

creased. Upon complete suppression of the TE_{21} oscillation, the amplified power rises precipitously to a high saturation level corresponding to $\sim 23\%$ efficiency, an indication that the presence of TE_{21} oscillation has severely degraded the amplification efficiency.

Figure 34 displays, in oscilloscope traces, oscillation suppression by a large-amplitude drive wave. In the absence of the drive wave, the TE_{21} oscillation is present over the duration of the beam pulse [Fig. 34(a)]. When a 1-kW, TE_{11} drive is applied in the middle of the beam pulse, the oscillation is completely suppressed [Fig. 34(b)] by the amplified TE_{11} wave [Fig. 34(c)]. Oscillation returns as soon as the drive is turned off.

C. Simulation analysis and physical interpretation

The preceding experiment was simulated by Chu *et al.* (1991) with a multimode, finite-size particle code (Ca-

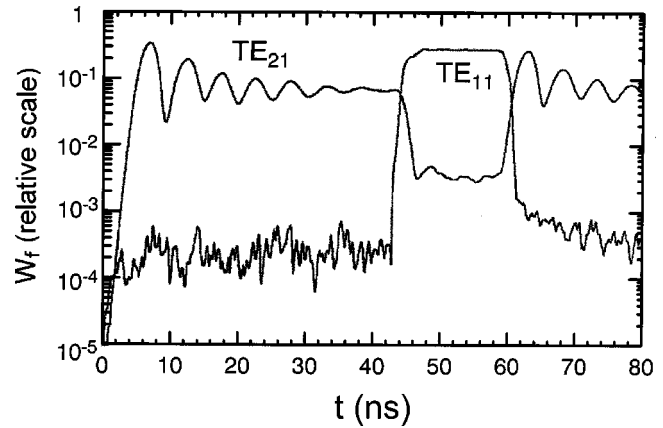


FIG. 35. Simulated evolution of the total field energy of TE_{21} and TE_{11} modes. The electron beam is injected at $t=0$. A 900-W, TE_{11} drive wave is injected at $t=42.5$ ns and turned off at $t=58$ ns. Other parameters are the same as in Fig. 33. From Chu *et al.*, 1991.

plan, Lin, and Chu, 1982). Figure 33(b) shows the simulated TE_{11} output power and TE_{21} oscillation power as functions of the TE_{11} drive power, using the experimental parameters of Fig. 33(a). Apart from minor quantitative differences, the simulation results exhibit all of the essential features of the measurements shown in Fig. 33(a).

To compare with the temporal measurements (Fig. 34), Fig. 35 plots the simulated evolution of the spatially integrated field energy (W_f) of both the TE_{11} and TE_{21} modes. The TE_{21} oscillation grows from the numerical noise level to a steady state as soon as the electron beam is injected at $t=0$. At $t=42.5$ ns, a 900-W TE_{11} drive wave is injected, which grows to the maximum amplitude on a time scale (~ 2 ns) comparable to the end-to-end transit time of the TE_{11} wave. The growth time is indicative of convective amplification. Consistent with the nonlinear nature of mode competition, the TE_{21} oscillation starts to diminish only when the TE_{11} wave has grown to a sufficiently high level. The oscillation is almost completely suppressed at $t=46$ ns. As the drive wave is turned off at $t=58$ ns, it immediately grows back to the predrive level. Simulated oscillation signals exhibit a few transient ripples when the electron beam is suddenly turned on and again when the drive signal is suddenly turned off. The ripples were not observed in the experiment because the experimental rise and fall times were much longer than the ripple period.

Numerical simulations have provided illuminating details not measurable in experiment. For example, consider the processes in Fig. 35. Figure 36 shows the electron distribution, at the end of the interaction section, as a function of the axial momentum p_z , the perpendicular momentum p_{\perp} , and the kinetic energy $W [= (\gamma - 1)m_e c^2]$. Initially (Fig. 36, $t=0$), the electron beam was monoenergetic ($W=W_0$) with a 5% spread in both p_z and p_{\perp} about the average values p_{z0} and $p_{\perp 0}$. The distribution function was then diagnosed at a time when

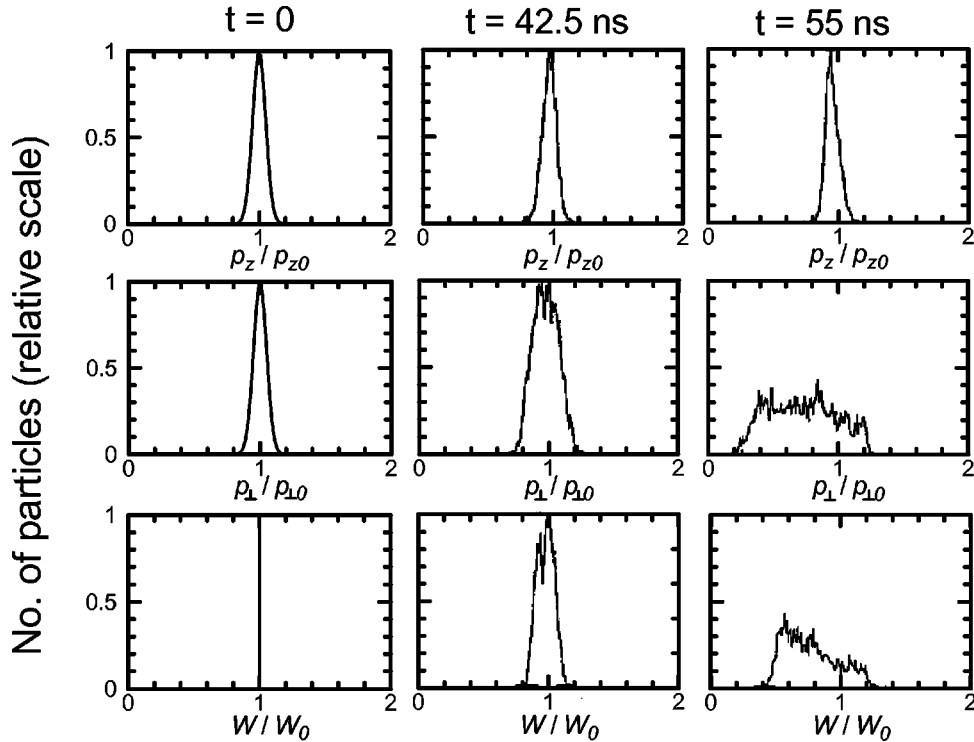


FIG. 36. Diagnostics of the electron distribution for the simulation in Fig. 35. The electron distribution at the end of the interaction section is diagnosed as a function of p_z/p_{z0} , $p_{\perp}/p_{\perp0}$, and W/W_0 , at times $t=0$, 42.5 ns, and 55 ns. From Chu *et al.*, 1991.

the TE_{21} oscillation dominated ($t=42.5$ ns), and later when the oscillation was completely suppressed ($t=55$ ns). Since neither mode had an axial electric field and the B_{\perp} field was weak at the near-cutoff frequency, the electrons experienced no axial electric force and only small ($\mathbf{v}_{\perp} \times \mathbf{B}_{\perp}$) axial forces. Thus the distribution in p_z changed slightly throughout the interaction (Fig. 36, first row). By comparison, the electrons developed a significant spread in both p_{\perp} and W in the course of the interaction (Fig. 36, bottom two rows).

The diagnostics in Fig. 36 also reveal the physical mechanism for the mode competition. Self-consistent beam perturbations associated with one mode will appear as deleterious momentum/energy spreads to another mode of different frequency and field structure, and vice versa. Mode suppression occurs when one mode reaches such a high level that its associated beam momentum or energy spread completely stabilizes the other mode. This can be seen in Fig. 36 ($t=42.5$ ns) where the steady-state TE_{21} oscillation is characterized by a p_{\perp} spread of $\sim 10\%$ and a W spread of $\sim 6\%$. As expected from the linear theory, spreads of such magnitude are insufficient to stabilize the TE_{11} instability. Thus the TE_{11} wave is amplified (at a reduced growth rate) in the presence of the TE_{21} oscillation. It will soon reach a much higher level than the TE_{21} oscillation, with an electron spread in p_{\perp} and W as high as 30–40% (Fig. 36, $t=55$ ns). Consequently the TE_{21} oscillation will be suppressed.

In all of the cases considered so far, the TE_{11} drive wave was injected after the TE_{21} oscillation had reached a steady state. The scenario of an early drive injection is simulated in Fig. 37, where a 450-W, TE_{11} drive wave is injected at $t=0$ along with the electron beam. The TE_{11} wave grows immediately, but not to a level sufficient to cause complete suppression of the TE_{21} oscillation (see Fig. 33 at $P_{in}=450$ W). Thus the TE_{21} oscillation soon catches up, and the TE_{11} level decreases as a result. The end state does not significantly differ from that of the late-injection case.

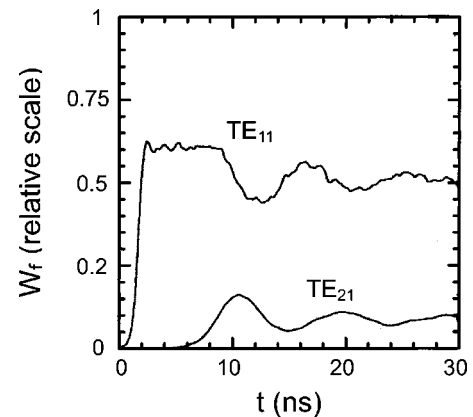


FIG. 37. Simulated evolution of the field energies of the TE_{21} and TE_{11} modes. The electron beam and a 450-W, TE_{11} drive wave are injected simultaneously at $t=0$. From Chu *et al.*, 1991.

D. Stabilization of reflective oscillations and absolute instabilities

1. Stabilization with a sever

Oscillation prevention is an important consideration for amplifier design, particularly under high-gain conditions. A severed structure is commonly employed in the TWT to increase the gain (Gilmour, 1986, Chap. 10). The sever effectively damps the backward wave and thereby cuts off the feedback path responsible for the global reflective oscillation caused by input/output mismatches. However, sever reflections can still trigger local oscillations in individual sections under criterion (80). The gain per section is thus limited (typically to 20 dB). More sections have been used to stack up the gain. This is possible because the gain achieved in previous section(s) is largely preserved in the ac signals embedded in the electron beam, even when the amplified wave is completely absorbed by the sever. The wave quickly grows back (to a few dB below the preabsorption level) as soon as the beam enters the next section. Thus, to the amplifying wave, all sections function as one integrated interaction structure.

A two-section, severed interaction structure [Fig. 31(b)] with a total length of 19.5 cm has been tested in an attempt to counter the TE_{21} absolute instability (Chu *et al.*, 1990b). The 3-cm-long sever located in the middle had a cold-circuit attenuation of ~ 30 dB. It significantly increased the TE_{21} oscillation threshold from 0.1 to 0.9 A. However, the threshold was still too low to allow stable operation at beam currents required for high-power generation. The limited success was a reminder of the severity of the absolute instability, which persisted even as a second cyclotron harmonic instability. Apparently, a different remedy is required.

2. Stabilization with distributed wall losses

The sever may be less effective in damping backward-wave oscillations in the first section because the power flows away from (instead of into) the sever. Weak coupling between the two sections may further lower the oscillation threshold. These possibilities suggest the use of a two-section interaction structure with wall losses distributed along the entire length of the first section¹⁷ [see Fig. 31(c)]. The lossy and copper sections constitute the linear and nonlinear stages, respectively. Similar to the sever, the lossy section cuts off the path of the reflective feedback loop. In contrast to the sever, it is also an amplification stage. The distributed loss absorbs the amplifying wave only in the region where its amplitude is small. However, to the predominantly backward power flow of the absolute instability, it functions as an effective energy sink.

¹⁷Distributed losses were employed in early gyro-TWT experiments for oscillation stabilization (Barnett *et al.*, 1980; Symons *et al.*, 1981).

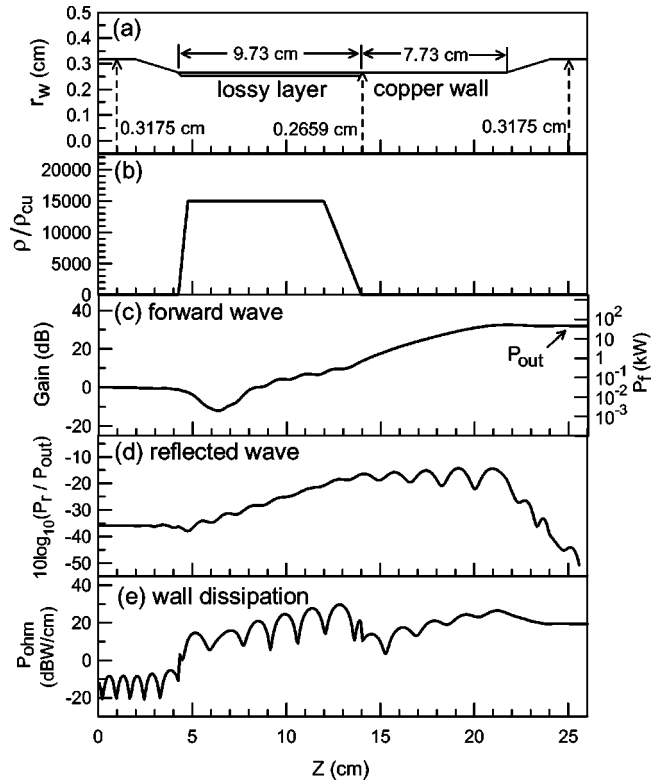


FIG. 38. Interaction structure and calculated powers (at $f = 34.2$ GHz) of a TE_{11} -mode, fundamental cyclotron harmonic gyro-TWT with distributed wall losses: (a) structure dimensions; (b) wall resistivity ρ (normalized to copper resistivity ρ_{cu}) vs z . The total cold-circuit attenuation is approximately 20 dB; (c) forward-wave power P_f and gain vs z ; (d) reflected backward-wave power (P_r , normalized to output power) vs z ; (e) Ohmic power P_{ohm} vs z . Here $V_b = 99.5$ kV, $\alpha = 0.85$, $I_b = 3$ A, $\Delta v_z/v_{z0} = 5\%$, $r_c/r_w = 0.35$, and $B_0/B_g = 0.99$. From Chu *et al.*, 1995.

The distributed-loss scheme was tested in a subsequent experiment. The circuit, shown in Fig. 38(a), has a total interaction length of 17.46 cm with the first 9.73 cm coated with Aquadag. The resistivity profile of the lossy section is shown in Fig. 38(b). Zero-drive stability was demonstrated at a beam current of 3 A, producing 62 kW saturated power with 33-dB gain, 21% efficiency, and a 3-dB bandwidth of 12% (Chu *et al.*, 1995). These figures represent substantial improvements over those of the first two attempts. Interestingly, they were accomplished with a total cold-circuit attenuation of only 20 dB (10 dB less than that of the previously used sever). However, a TE_{11} oscillation limited the stable operating current to 3 A.

Physical processes in this experiment, modeled with a single-mode, particle-tracing code, are displayed in Figs. 38(c)–(e). As is well known for both the TWT (Gilmour, 1986, Chap. 10) and the gyro-TWT (Kou, 1995), amplification is always preceded by a launching loss [Fig. 38(c)]. It is interesting to note that the forward wave grows linearly in the lossy section, accumulating a gain of 13 dB just before it enters the copper section [Fig. 38(c)]. With the lossy section replaced by a copper sec-

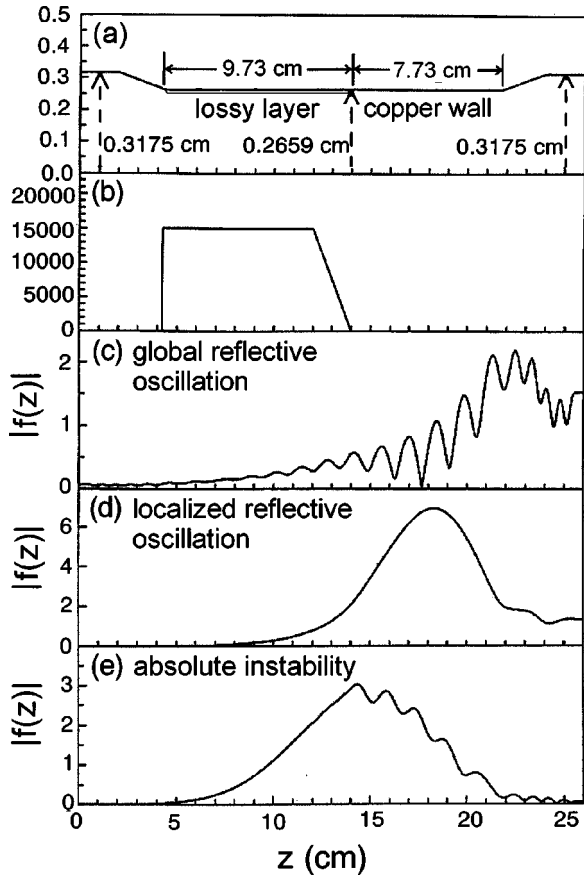


FIG. 39. Calculated rf field profiles, $|f(z)|$, of three types of oscillations in a distributed-loss structure: (a) and (b), the structure; (c) global reflective oscillation of the TE_{11} mode; (d) localized reflective oscillation of the TE_{11} mode; (e) the TE_{21} absolute instability. Operating parameters in (c)–(e) were chosen to accentuate the respective types of oscillations. From Chu *et al.*, 1998, 1999.

tion, there would be a total gain of 23 dB over the same distance. The 10-dB difference is much less than the cold-circuit attenuation (20 dB) of the lossy section. This illustrates a basic difference between the resistive damping of cold and hot modes. The cold mode has all of its energy in the electromagnetic fields. For the beam-generated hot mode, however, a substantial portion of the energy also resides in the ac motion of the electrons. The lossy wall absorbs the electromagnetic energy but not the electron kinetic energy. Thus it attenuates the reflected wave (basically a cold mode) more than it reduces the gain of the amplifying wave (a hot mode). Not counting the launching loss, it has been analytically shown (Lau *et al.*, 1981b) that the reduction in hot-tube gain due to the wall resistivity is only one-third that of the cold-circuit attenuation over the same distance.

Reflected power and Ohmic power are also diagnosed in Figs. 38(d) and (e), respectively. There is no reflective oscillation because approximately 99% of the reflected power has been absorbed in the lossy section. Total Ohmic power dissipated on the wall equals approximately 1.1% of the beam power.

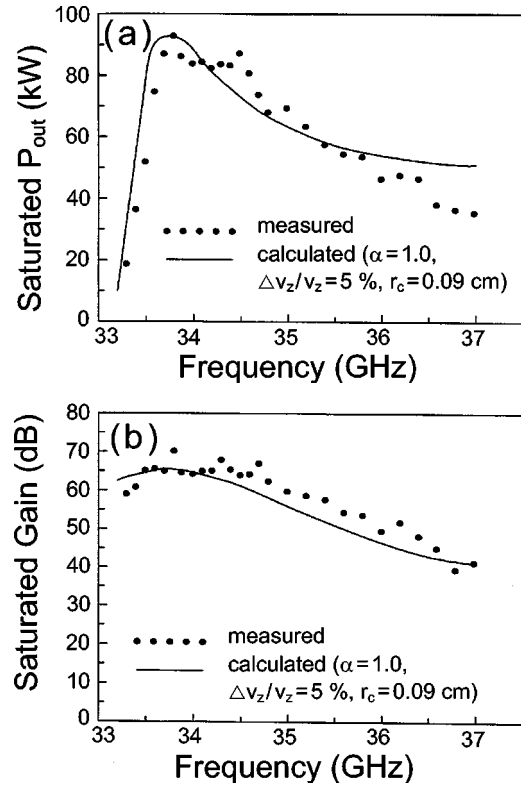


FIG. 40. Saturated output power and gain vs the frequency of an ultrahigh-gain gyro-TWT: dots, measured data; solid curves, calculated. $V_b = 100$ kV, $I_b = 3.5$ A, $B_0 = 12.7$ kG, $L_1 = 20$ cm, and $L_2 = 4$ cm (see Fig. 31). The calculation assumes $\alpha = v_{\perp 0}/v_{z0} = 1$, $r_c/r_w = 0.35$, $\Delta v_z/v_{z0} = 5\%$, and a wall resistivity of $\rho = 3.6 \times 10^4 \rho_{cu}$ for the lossy section consistent with the measured cold circuit attenuation of ~ 100 dB near the cutoff frequency. From Chu *et al.*, 1998, 1999.

E. An ultrahigh-gain scheme

Successful demonstration of the lossy section as both a linear amplification stage and an oscillation stabilizer suggests a scheme for ultrahigh-gain operation. In this scheme, the lossy section is made sufficiently long so as to provide the desired gain, while the copper section is constrained to a minimum length to increase the thresholds of absolute instabilities. On the other hand, the observed TE_{11} oscillation at $I_b > 3$ A warrants a closer examination of stability issues. Further theoretical studies have indicated that three types of oscillations are associated with the distributed-loss structure [Figs. 39(a) and (b)]. In addition to the global oscillation due to reflections at the input/output ends [Fig. 39(c)] and the TE_{21} absolute instability [Fig. 39(e)], the copper section is susceptible to a localized oscillation [Fig. 39(d)], much like that of the gyromonotron (Sec. V.D). The operating parameters in Fig. 39 have been chosen to accentuate the oscillation problems. In practice, these oscillations can be stabilized with increased wall losses and/or decreased copper section length (Chu *et al.*, 1999).

An experiment has been conducted to test the high-gain scheme (Chu *et al.*, 1998, 1999) by employing a mechanically tunable magnetron injection gun (Wang *et al.*,

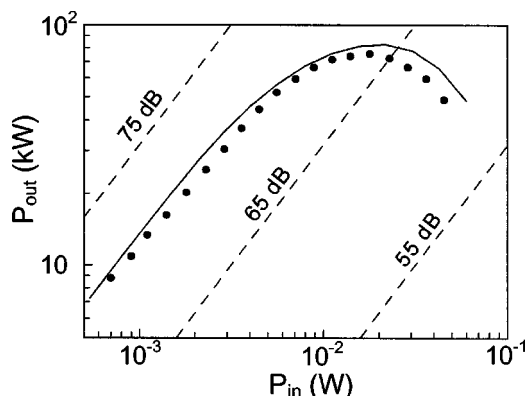


FIG. 41. Output power vs drive power at 34.2 GHz: dots, measured; solid curve, calculated. Other parameters are the same as in Fig. 40. From Chu *et al.*, 1998, 1999.

1997). The interaction structure consists of a 4-cm copper section preceded by a 20-cm, Aquadag-coated lossy section with a cold-circuit attenuation of ~ 100 dB. The Aquadag layer has a thickness of ~ 0.007 cm, which is approximately equal to the skin depth. Oscillations inside the couplers have limited the maximum stable operating current to 3.5 A. At this operating current, the experiment produced 93 kW saturated output power at a gain of 70 dB, more than 30 dB beyond that previously achieved by the gyro-TWT. Improved stability permitted operation at a higher α value ($v_{\perp 0}/v_{z0} \cong 1$) and hence higher efficiency (26.5%). Figure 40 plots the measured (dots) and calculated (solid lines) output power and gain as functions of the frequency, and both indicate a 3-dB bandwidth of $\sim 8.6\%$. Figure 41 shows the measured (dots) and calculated (solid lines) output power versus the input power. Zero-drive stability is evidenced by good linearity of the transfer curve. Measurements and calculations are in good agreement in both figures. Table VII compares the key parameters of this proof-of-principle gyro-TWT with those of a state-of-the-art TWT.

F. Harmonic multiplying amplification

In the multistage amplifier, the rf fields in neighboring stages are isolated by a cutoff section (as in the gyroklystron) or a sever (as in the severed gyro-TWT). In the evanescent region between stages, the ac signal is embedded in the electron beam, which drives an oscillation or launches an amplifying wave upon entering the next stage. In such configurations, nonlinearity of the electron dynamics can be exploited for harmonic multiplying operation. In the linear analysis of the electron

beam acted upon by a small-signal drive wave, higher-order terms are neglected. These neglected terms are multiplications of first-order perturbations at the drive frequency and, if retained, give rise to low-level harmonic components. The harmonic contents become richer as the beam-embedded ac signal grows in magnitude through, for example, drift-space bunching or preamplification in the first stage. Harmonic multiplying amplification will result if conditions in subsequent stage(s) are set to favor interaction with a particular harmonic component of the beam current.

The harmonic multiplying scheme is of practical interest because of the reduced magnetic-field requirement and the ready availability of low-frequency drivers. The scheme can be implemented in different configurations. A frequency-doubling, two-cavity gyroklystron has been demonstrated that produced 21-MW output power at 19.76 GHz with an efficiency near 21% (Lawson *et al.*, 1993). An improved four-cavity version is under development for linear collider applications (Yovchev *et al.*, 2000). A frequency-doubling inverted gyrotwystron has also been demonstrated (Guo *et al.*, 1997; Rogers *et al.*, 2001) and analyzed (Zhao *et al.*, 2000). The experiment produced Ka-band output at approximately 100-kW power levels. Harmonic multiplying amplifiers are nonlinear devices possessing characteristics fundamentally different from those of a single-frequency amplifier. Issues such as the gain/power scaling, input/output phase relation, and interference from lower harmonic beam perturbations have been studied for the traveling-wave configuration (Chu, Guo, and Granatstein, 1997).

G. Summary and discussion

Oscillations due to absolute instabilities are the most serious problem encountered in the gyro-TWT. Competition between convective and absolute instabilities has been examined in theory and experiment. Oscillations due to circuit reflections have also been identified and analyzed. Distributed attenuation has been shown to be effective in stabilizing both types of oscillations. These studies have led to the demonstration of a stable gyro-TWT with ultrahigh gain by taking advantage of the fact that the reduction in hot-tube gain due to the wall resistivity is only one-third that of the cold-circuit attenuation over the same distance.

Although convenient for physics studies, a waveguide coated with Aquadag is incompatible with high-average-power operation. For increased tolerance to wall heating, the NRL group has recently built a 35-GHz, TE₀₁-mode gyro-TWT employing ceramic rings for distributed attenuation. The experiment produced 137 kW

TABLE VII. Comparison of the experimental gyro-traveling-wave tube with the state-of-the-art TWT (Varian/CPI model VTA 5701).

Type	Voltage	Current	Magnet	Peak power	Efficiency	Gain	Bandwidth
gyro-TWT	100 kV	3.5 A	cryogenic	93 kW	26.5%	70 dB	8.6%
TWT	45 kV	7 A	solenoid	50 kW	16%	40 dB	6%

saturated power in zero-drive stable operation with 47 dB gain, 17% efficiency, and a 3-dB bandwidth of 3.3% (Garven *et al.*, 2002). Diffractive slots are being developed for still greater power-handling capability (Pershing *et al.*, 2002).

Distributed attenuation has been a long-practiced technique to stabilize the conventional TWT. In linear beam interactions, however, ac space-charge fields may overwhelm the depressed rf fields in the lossy section, resulting in poor electron bunching and degraded efficiency (Gilmour, 1986, Chap. 10). For this reason, short severers are more commonly employed in the TWT. By comparison, negligible spatial bunching in cyclotron interactions (Sec. IV.F) makes distributed attenuation a viable scheme for the gyro-TWT, as can be seen by the efficient operation of the gyro-TWT with a long lossy section.

Highlights of worldwide research on the gyro-TWT have been briefly summarized in Sec. V.B.3. A detailed survey can be found in Chu (2002). These efforts have culminated in the demonstration of the gyro-TWT as a new generation of millimeter-wave amplifiers of unprecedented power, gain, efficiency, and bandwidth.

VII. NONLINEAR FIELD CONTRACTION IN BACKWARD-WAVE OSCILLATIONS

Backward-wave oscillations form the basis of the gyro-BWO and may also be present as an interference to the normal operation of the gyro-TWT. As discussed in Sec. V.E.1, these oscillations build on an internal feedback process, which requires no resonant structure. Consequently there are only hot resonant modes without cold counterparts. In the absence of a resonant structure, the oscillation frequency and axial field profile are governed entirely by the interaction dynamics. In this section, we consider a resultant nonlinear property that distinguishes the gyro-BWO from other device types (Chen, Chu, and Chang, 2000).

A. Modeling of backward-wave oscillations

Theoretical studies of the gyro-BWO usually begin with a linear calculation of the start-oscillation current (Wachtel and Wachtel, 1980; Park, Granatstein, and Parker, 1984; Kou, 1994). Orbit tracing techniques¹⁸ or particle simulations¹⁹ are then employed to follow the nonlinear behavior. In the standard treatment, self-oscillation of the backward wave is formulated as a condition of infinite gain, with a zero-field point imposed at the downstream end. This condition is justifiable when the downstream field tapers down to small values, as is usually the case. Rigorously, however, there is no reason

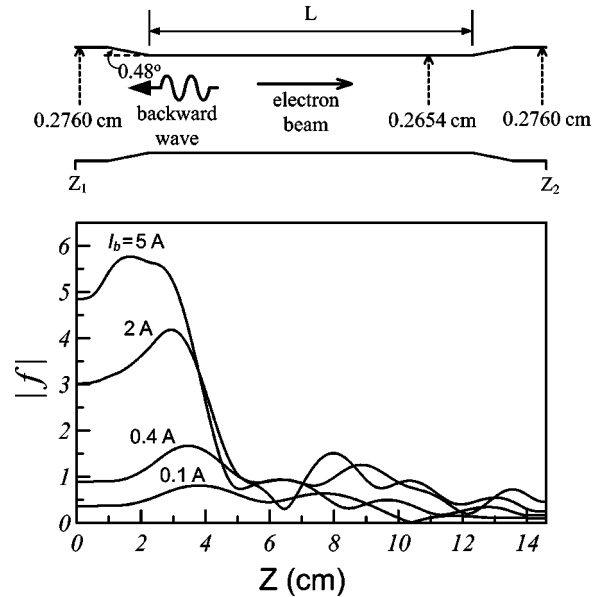


FIG. 42. Model and axial field profiles of a gyro-BWO: upper figure, configuration of the Ka -band, TE_{11} -mode gyro-BWO under study; lower figure, calculated axial field profile ($|f|$, on relative scale) at different values of beam current (I_b), showing the effect of nonlinear field contraction. $L=10$ cm, $B_0=14.52$ kG, $V_b=100$ kV, $\alpha=1$, and $r_c/r_w=0.35$. A cold beam is assumed. The oscillation frequency varies from 33.3 to 33.5 GHz as the beam current increases from 0.1 to 5 A. From Chen, Chu, and Chang, 2000.

to demand a zero field at a fixed position or even its presence at all. Hence we impose outgoing-wave boundary conditions at both ends. In the absence of external excitation, any solution that exists must be one of self-oscillation. Since the field is at no point restricted to a fixed value, it is allowed to relax to a self-consistent profile at any beam current above threshold. For the study in this section, a single-mode, steady-state code (Chu *et al.*, 1999) is employed.

We model a Ka -band, TE_{11} -mode gyro-BWO by the configuration shown in Fig. 42. It consists of a uniform interaction section of length L connected at each end, through a 0.48° up-taper, to a short uniform section of slightly larger radius. The end tapers model the couplers employed in the experiment to be described in Sec. VIII. There are small reflections at the taper interfaces. Weak interaction in the upstream taper results in less abrupt electron bunching and thus increases the interaction efficiency (Kou, Chen, and Wu, 1998). All of these effects are modeled in the theory. The presence of end tapers will not change the basic conclusions.

B. Nonlinear field contraction

Figure 42 shows the evolution of the axial field profile (for $L=10$ cm) from the linear state ($I_b=0.1$ A) to a highly nonlinear state ($I_b=5$ A). The field is seen to contract significantly toward the upstream end as I_b increases. Field contraction represents the combined effect of early electron energy depletion and backward

¹⁸See, for example, Bratman *et al.* (1981), Ganguly and Ahn (1989), Nusinovich and Dumbrajs (1996), Kou, Chen, and Wu (1998), Chen, Chu, and Chang (2000).

¹⁹See, for example, Lin (1992), Lin and Kaw (1992), Walter *et al.* (1996), and Arman (1998).

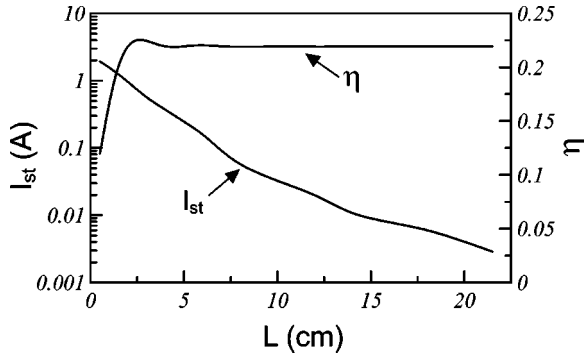


FIG. 43. Calculated start-oscillation current (I_{st}) and nonlinear interaction efficiency (η) vs the uniform section length (L). The start-oscillation current depends sensitively upon L , whereas the nonlinear interaction efficiency (all evaluated at the beam current of 5 A) is almost independent of L as long as L exceeds a relaxation value of ~ 3 cm (cf. Fig. 45). Other parameters are the same as in Fig. 42. From Chen, Chu, and Chang, 2000.

flow of the generated power. At higher beam currents, the interaction intensifies, and saturation occurs early. Thus the electron energy is depleted in a shorter distance. Following saturation, the “spent” electron beam generates much less power as it flows downstream. Since there is no forward wave in the circuit to transfer energy

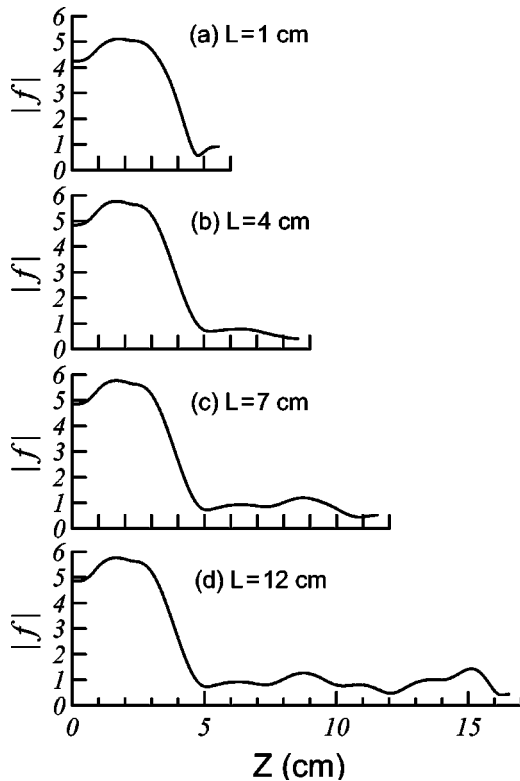


FIG. 44. Calculated nonlinear field profiles (relative scale, plotted from z_1 to z_2 of Fig. 42) for $I_b = 5$ A and (a) $L = 1$ cm; (b) $L = 4$ cm; (c) $L = 7$ cm; and (d) $L = 12$ cm. Other parameters are the same as in Fig. 42. From Chen, Chu, and Chang, 2000.

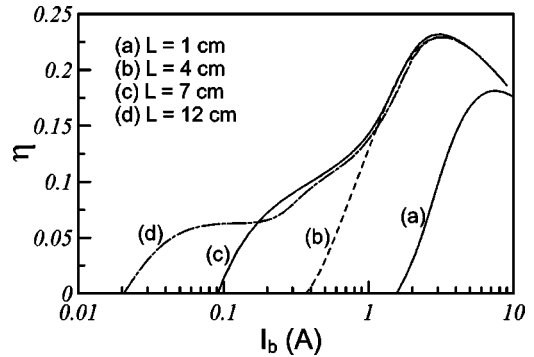


FIG. 45. Calculated efficiency vs beam current for different values of L . Oscillations start at widely different currents, but exhibit almost the same nonlinear behavior as long as L exceeds the relaxation length of ~ 3 cm. Other parameters are the same as in Fig. 42. From Chen, Chu, and Chang, 2000.

down to the region of weak interaction, the field amplitude decreases immediately upon depletion of the electron energy.²⁰

The consequences of nonlinear field contraction are displayed in Fig. 43, which compares the start-oscillation current (I_{st} , a linear quantity) and the nonlinear interaction efficiency (evaluated at $I_b = 5$ A) as functions of L . Linearly, the electron beam becomes more tightly bunched in a longer interaction structure. Hence I_{st} decreases sharply with increased L . In contrast, the nonlinear efficiency remains almost constant as long as L exceeds a certain “relaxation length” (approximately half a guide wavelength for the present case). The constancy of the nonlinear efficiency can be understood in light of the corresponding field profiles plotted in Fig. 44 for several values of L . It can be seen that the bulk field contracts to virtually the same profile, provided that L exceeds the relaxation length [Figs. 44(b)–(d)]. With negligible influence from the weak trailing fields, all the interaction efficiencies thus reach virtually the same value.

Linear and nonlinear behavior are examined from a different perspective in Fig. 45, which plots the interaction efficiency as a function of I_b for several values of L . For each L value, the oscillation starts at the beam current at which the efficiency approaches zero, then transitions into the nonlinear regime as I_b increases. Between $L = 1$ cm and $L = 12$ cm, I_{st} varies by almost two orders of magnitude, whereas the saturation current and saturated efficiency remain virtually independent of L provided it exceeds the relaxation length (~ 3 cm). The nearly identical nonlinear behavior displayed in curves (b)–(d) is consistent with the nearly identical bulk field profiles shown in Figs. 44(b)–(d).

C. Summary and discussion

We have shown that the effect of nonlinear field contraction is to completely decouple the linear and nonlin-

²⁰By the same argument, nonlinear field contraction might also take place in the conventional BWO.

ear behaviors of the gyro-BWO, especially in a long interaction structure. Linear interaction extends over the entire structure length, whereas nonlinear interaction is concentrated within an effective length determined only by the interaction dynamics. This marks a fundamental difference between the gyro-BWO and the gyromonotron. In the latter device, the feedback loop and hence the field profile extends from end to end in both the linear and nonlinear regimes. This difference will significantly impact the performance optimization of the gyro-BWO, as illustrated in the following example.

Most of the gyro-BWO experiments reported so far (see, for example, Park *et al.*, 1990; Kou *et al.*, 1993; Basten *et al.*, 1995) have employed an interaction length of at least two guide wavelengths, which scales to $L > 12$ cm for the Ka -band structure of Fig. 42(a). Erratic frequency tuning has often been observed. Possible causes include mode competition, mode switching, and self-modulation. These phenomena are all expected to have higher threshold currents with a shorter interaction length. On the other hand, field profiles all relax nonlinearly to a short width of ~ 3 cm regardless of the structure length (Fig. 44). Thus elimination of the extra interaction length may provide a simple remedy at no expense to the interaction efficiency (Fig. 43).

The distinctive properties of the gyro-BWO also have important implications for nonstationary behavior. The results presented in this section were obtained with a steady-state code. While the solutions represent valid equilibrium states, there is no verification that these states are stable. Stability issues will be examined in the following section with a time-dependent code.

VIII. NONSTATIONARY OSCILLATIONS

Inherently a high-power source, the gyrotron is susceptible to a range of single-mode and multimode nonstationary behavior. In various ways, this behavior imposes severe limitations on gyrotron performance. Multimode effects in the gyro-TWT have been considered in Sec. VI. Here, we examine the nonstationary behavior resulting from the overdrive of a single mode of the gyromonotron and gyro-BWO.

A. Single-mode nonstationary behavior

It was recognized early in theory (Ginzburg, Kuznetsov, and Fedoseeva, 1978) and experiment (Bezruchko and Kuznetsov, 1978) that the onset currents for nonstationary oscillations in a conventional BWO range typically from 2.5 to 3.5 times the start-oscillation current. Similar results have also been reported in more recent theoretical investigations of the BWO (Dmitriev, Trubetsko, and Chtverikov, 1991; Levush *et al.*, 1992) and the gyromonotron (Nusinovich and Zapevalov, 1985; Ginzburg, Nusinovich, and Zavolsky, 1986; Lin, Yang, and Chu, 1988). Immediately above the nonstationary threshold, the oscillation amplitude is modulated, which generates sidebands separated from the main frequency by approximately

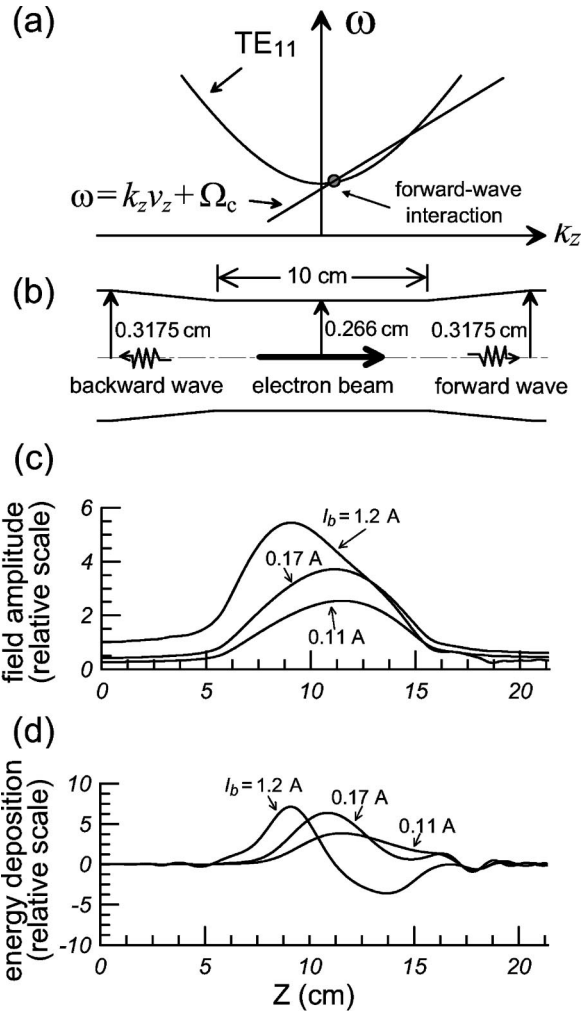


FIG. 46. Model and calculated behavior of a gyromonotron: (a) operating point of the gyromonotron in the ω - k_z diagram. $\Omega_c (= \Omega_e / \gamma)$ is the electron cyclotron frequency; (b) geometry and dimensions of the interaction structure; (c) calculated linear and nonlinear field profiles at different I_b ; (d) calculated beam energy deposition profiles for the corresponding fields shown in (c). A cold electron beam is assumed. $V_b = 100$ kV, $\alpha = 1$, $r_c / r_w = 0.35$, and $B_0 = 13.47$ kG. From Chang *et al.*, 2001.

$$\Delta f \sim 1 / (\tau_w + \tau) \quad (81a)$$

for the BWO and

$$\Delta f \sim 1 / (2\tau_w) \quad (81b)$$

for the gyromonotron, where τ_w is the wave transit time at the group velocity and τ is the electron transit time. The denominator in Eqs. (81a) or (81b) is the time required for a modulation signal to complete a round-trip path in the feedback loop. Such single-mode nonstationary behavior is referred to as *self-modulation*. As the beam current increases further, harmonic sidebands appear, and eventually the system transitions from the self-modulation state into a chaotic state. During the transition, doubling of the modulation period has been observed in a simulation study (Lin, Yang, and Chu, 1988).

The theories discussed above are based on equal in-

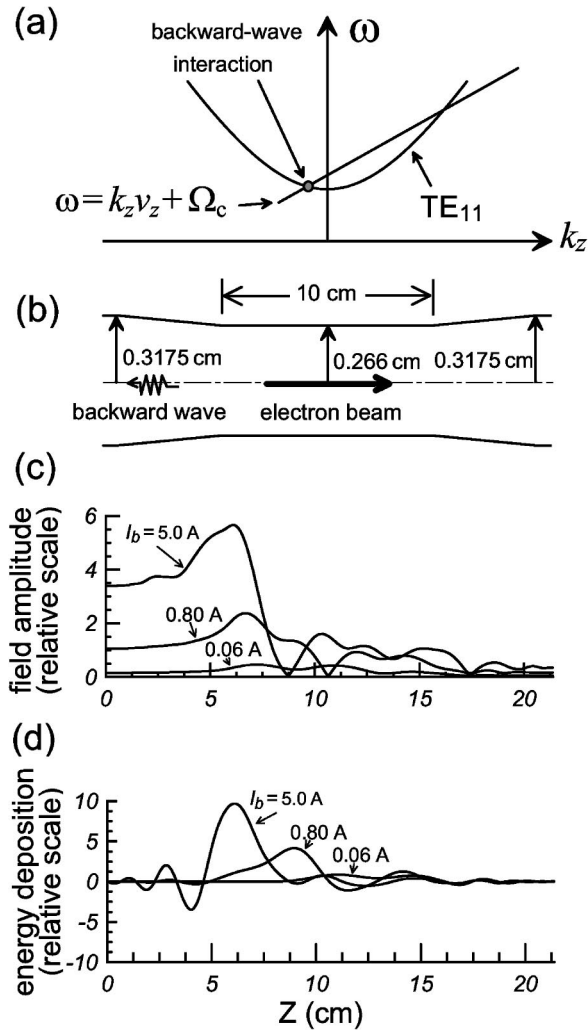


FIG. 47. Model and calculated behavior of a gyro-BWO: (a) operating point of the gyro-BWO in the ω - k_z diagram; (b) same interaction structure as in Fig. 46(b); (c) calculated linear and nonlinear field profiles at different I_b . (d) Calculated beam energy deposition profiles for the corresponding fields shown in (c). A cold electron beam is assumed. $V_b=100$ kV, $\alpha=1$, $r_c/r_w=0.35$, and $B_0=14.59$ kG. From Chang *et al.*, 2001.

interaction length in linear and nonlinear regimes. The onset currents for stationary and nonstationary oscillations both vary with the interaction length in much the same manner, so that their ratio remains largely fixed. However, for the gyro-BWO, the effective lengths for linear and nonlinear interactions can be drastically different (Fig. 42), which makes it impossible to establish a fixed relationship between the oscillation threshold (a linear effect) and the nonstationary threshold (a nonlinear effect). This and other related issues will be addressed here through a comparative study of the nonstationary behavior of the gyromonotron and gyro-BWO.

B. Experimental observations

We first discuss a recent experimental study on a *Ka*-band, TE₁₁-mode gyromonotron and gyro-BWO with

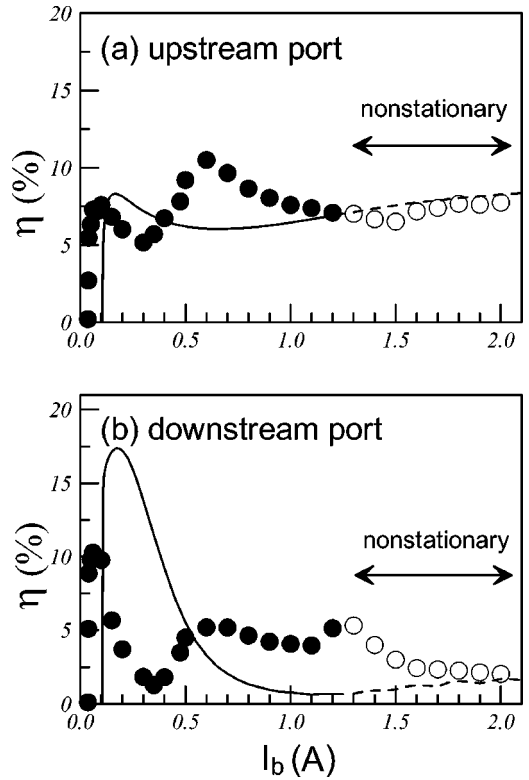


FIG. 48. Output power (normalized to the beam power) of a gyromonotron at (a) the upstream port and (b) the downstream port as functions of the beam current: ●, measured power in the stationary state; ○, measured power in the nonstationary state; solid curve, calculated power for the stationary state; dashed curve, calculated power for the nonstationary state. Parameters are the same as in Fig. 46. From Chang *et al.*, 2001.

the same interaction structure (Chang *et al.*, 2001). The geometry and dimensions of the interaction structure are shown in Figs. 46(b) and 47(b). The 10-cm uniform interaction section in the middle is connected at each

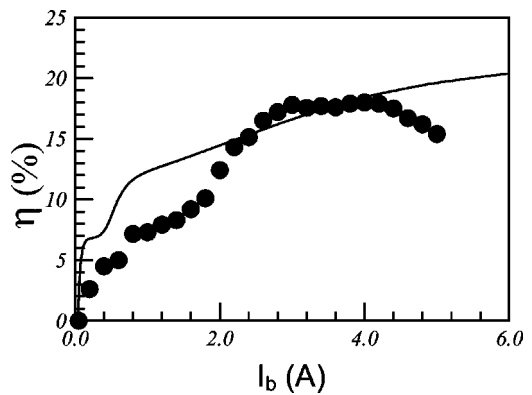


FIG. 49. Output power (normalized to the beam power) of gyro-BWO at the upstream port as a function of the beam current: ●, measured power; solid curve, calculated power. Measured and calculated powers at the downstream port (not shown) are negligible by comparison. Stationary oscillations have been observed at all operating currents. Parameters are the same as in Fig. 47. From Chang *et al.*, 2001.

end by a 5-cm up-taper (with a 0.57° taper angle) to a uniform output section of 0.7 cm in length. Reflections from the end tapers can result in gyromonotron oscillations; however, the reflection coefficients are sufficiently weak for the structure to function also as a gyro-BWO circuit at higher magnetic fields. Transition from one type of oscillation to the other is effected by magnetic-field adjustment only [Figs. 46(a) and 47(a)]. It is therefore possible to make a direct comparison between the measurements in the two regimes. Other parts of the experimental setup are described in Sec. VI.B.

In both the gyromonotron and gyro-BWO regimes, oscillations were observed to start at $I_b \cong 50$ mA. However, the gyromonotron oscillation became nonstationary at $I_b = 1.29$ A, while the gyro-BWO oscillation remained stationary up to the maximum operating current of 5 A. An oscillation in the output coupler, detected at $I_b > 5$ A, prevented further measurement beyond 5 A. Figures 48(a) and (b) show the measured output power (normalized to the beam power) at, respectively, the upstream and downstream ports of the gyromonotron as a function of I_b . Output powers measured in the stationary state are indicated by dots, and those measured in the nonstationary state (time-averaged values) are indicated by circles. Figure 49 shows the output power of the gyro-BWO (dots, also normalized to the beam power) measured at the upstream port up to $I_b = 5$ A. Output power at the downstream port (not shown) is negligible by comparison. Calculated values, obtained with a stationary code, are also plotted in Figs. 48 and 49 for comparison. They are shown with dashed lines in the (experimentally observed) nonstationary regime.

The difference in feedback processes is evident from the power measurements. The feedback loop of the gyromonotron consists of two counterstreaming waves. Hence there are comparable power levels at both ends (Fig. 48). However, the feedback loop of the gyro-BWO consists of the backward wave and the forward-moving electron beam. This results in the predominance of the output power at the upstream end (Fig. 49).

The nonstationary behavior of the gyromonotron was diagnosed with an oscilloscope and a spectrum analyzer (HP8564E). The video response of the detector and oscilloscope is ~ 260 MHz at 3 dB. The spectrum analyzer is gated with a high-speed diode switch to block the rise and fall portions of the signal and hence the transient effects. Figures 50(a)–(f) show the gated signal traces and corresponding spectrograms of the gyromonotron output pulse at different beam currents. The center frequency varies steadily from 33.19 GHz at $I_b = 50$ mA to 33.42 GHz at $I_b = 2$ A. The oscillation is stationary [Fig. 50(a)] at beam currents up to 1.29 A. At $I_b = 1.29$ A, sidebands begin to appear [Fig. 50(b)], which are symmetrically separated from the center frequency by approximately 102 MHz, in good agreement with Eq. (81b) if we assume an effective interaction length of 18 cm. Harmonic sidebands then appear at increased beam currents [Fig. 50(c)]. At still higher beam currents, doubling

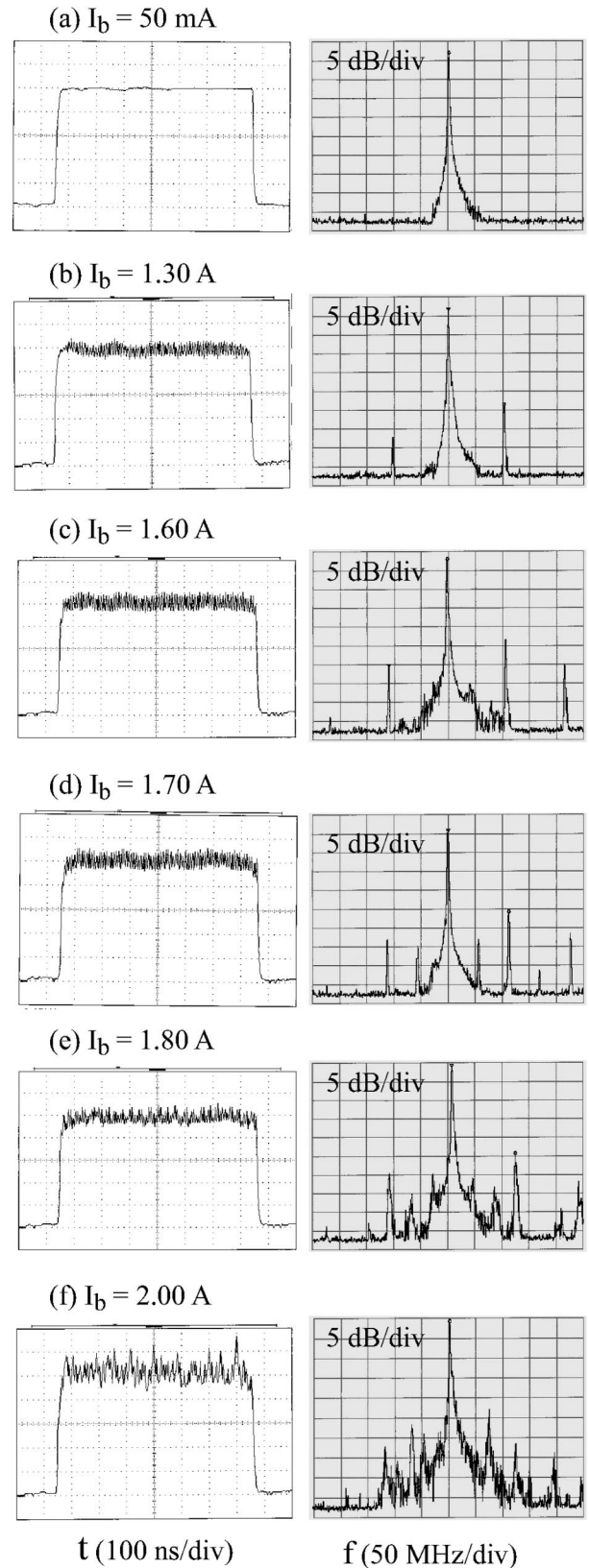


FIG. 50. Signal traces and corresponding spectrograms of gated gyromonotron output at different beam currents. Adapted from Chang *et al.*, 2001.

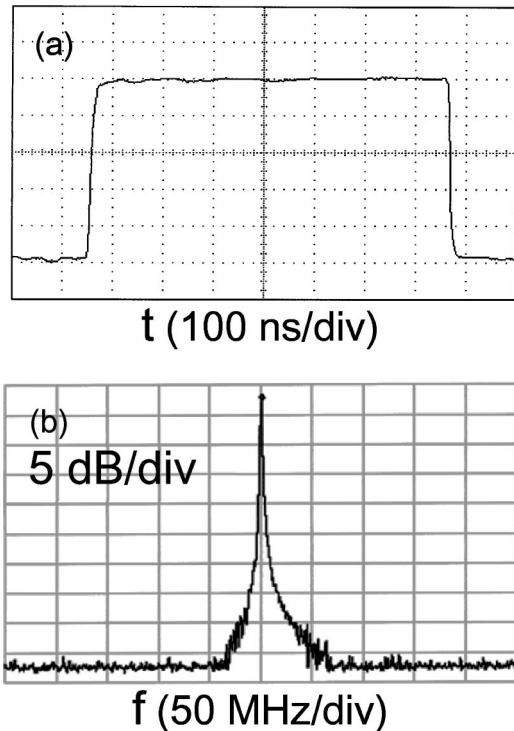


FIG. 51. Signal trace and corresponding spectrogram of a gated gyro-BWO output signal at $I_b = 5$ A, showing stationary oscillation at a single frequency. Adapted from Chang *et al.*, 2001.

[Fig. 50(d)] and tripling [Fig. 50(e)] of the modulation period are witnessed before the oscillation eventually turns stochastic [Fig. 50(f)].

By comparison, the gyro-BWO remains stationary [Fig. 51(a)], within the 260-MHz video response of the detector, up to the maximum operating current of 5 A (100 times I_{st}).²¹ At $I_b = 5$ A, the spectrum [Fig. 51(b)] is characterized by a single frequency at 34.2 GHz and a spectral width (~ 1.2 MHz) consistent with the pulse length.

C. Theoretical interpretation

Calculated stationary field profiles of the gyromonotron are shown in Fig. 46(c). They represent a stable balance between the (axially) uneven deposition of the beam energy [Fig. 46(d)] and its equilibration through counterstreaming traveling waves. The two curves in Fig. 46(d) marked by $I_b = 0.11$ and 0.17 A show the beam energy deposition profiles in the linear and saturated states, respectively. The curve marked by $I_b = 1.2$ A shows the deposition profile just before the onset of the (experimentally measured) nonstationary state. In the marginally stable state ($I_b = 1.2$ A), it can be seen that the overbunched electron beam rapidly re-

²¹In an early gyro-BWO experiment (Kou *et al.*, 1993), stationary oscillations were observed at a beam current 500 times higher than the theoretical oscillation threshold.

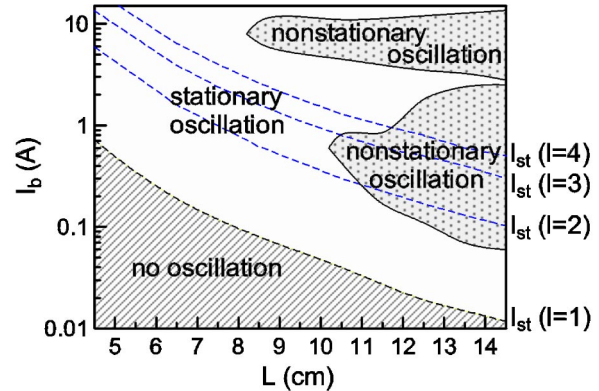


FIG. 52. Simulated stability map of a gyro-BWO with a uniform interaction structure of length L . Multiple nonstationary zones appear in the I_b - L space. No correlation is seen between the onset current of the nonstationary state and that of any higher-order axial mode (dashed curve). Other parameters are the same as in Fig. 28. From Chen *et al.*, 2002.

leases its energy to the field and then immediately retrieves a large fraction as it propagates downstream. As a result, the field shape is distorted. Upon further current increase, the oscillation becomes nonstationary, characterized by back-and-forth bounces of the field peak and hence the appearance of sidebands.

The field profile in the gyromonotron is shaped primarily by the resonant structure. Hence, as shown in Fig. 46(c), the linear and nonlinear field profiles differ only in amplitude but maintain almost the same shape up to the saturation current of 0.17 A. However, the gyro-BWO axial field profile depends only upon the interaction dynamics. Thus, as shown in Fig. 47(c), rapid energy depletion at higher beam currents results in a much-contracted field. This facilitates energy equilibration and explains the observed stability at beam currents far above the oscillation threshold (see Fig. 49).

D. Time-dependent simulation of the gyro-BWO

Time-dependent gyro-BWO simulations (Nusinovich, Vlasov, and Antonsen, 2001; Grudiev and Schunemann, 2002) on the weakly tapered structure of Fig. 42 confirmed its stability at beam currents far above I_{st} . However, these studies also revealed the puzzling effect that stationary and nonstationary states alternately appear as the beam current rises. To avoid complications arising from a tapered structure, time-dependent simulations were subsequently performed for a uniform interaction structure, assuming perfect matching at both ends (Chen *et al.*, 2002). Stability properties are displayed in the parameter space of I_b and L (Fig. 52). Again, it is shown that the onset currents for nonstationary oscillations can be more than 100 times I_{st} (for $L < 10$ cm). Multiple zones of nonstationary states are also found for the uniform structure. This phenomenon thus appears to be general, though reasons for it are still unclear. As a first step toward an interpretation, we consider below possible causes of the nonstationary oscillation.

We have shown in Sec. V.E.2 that higher-order axial modes of a gyro-BWO are characterized by larger electron transit angles and hence more regions of negative energy deposition. Interaction weakens with negative energy deposition. Consequently, the higher the mode order, the greater the start-oscillation current.²² This is exhibited in Fig. 52. Superposed on the stability map are the start-oscillation currents of the first four axial modes (dashed curves, $l=1-4$) obtained with a single-mode, steady-state code. As expected, I_{st} of the fundamental axial mode ($l=1$) falls precisely on the boundary between no oscillation and stationary oscillations found from time-dependent simulations (Fig. 52). However, there is no correlation between the I_{st} of higher-order axial modes (obtained with the single-mode, steady-state code) and the onset current of the nonstationary state (obtained with the time-dependent code). For example, oscillations can either remain stable at beam currents far above the I_{st} of the $l=4$ mode (for $L < 8$ cm) or turn nonstationary at currents well below the I_{st} of the $l=2$ mode (for $L > 11$ cm). It thus appears that axial mode competition cannot be the cause of the nonstationary behavior.

Figure 53 displays the calculated output spectrum at a beam current slightly above the onset current of the nonstationary state for $L=8.5$ cm and 12 cm. Both spectra exhibit characteristics similar to self-modulated oscillations of the gyromonotron [Figs. 50(b) and (c)]. The frequency separation between the main oscillation and sidebands is greater for $L=8.5$ cm than for $L=12$ cm, which is consistent with the higher oscillation frequency (hence faster group velocity) and shorter bounce distance in the former case [see Eq. 81(a)]. This qualitatively identifies self-modulation to be the cause of nonstationary oscillations.

E. Summary and discussion

Nonstationary behavior of the gyromonotron has been experimentally characterized and theoretically interpreted in terms of uneven beam energy deposition. On the other hand, the gyro-BWO exhibits a much broader stable operating range, which can be attributed to rapid energy equilibration in the contracted rf field. In both cases, the onset stage of nonstationary oscillations displays evidence of self-modulation, rather than axial mode competition. The existence of multiple nonstationary zones in the gyro-BWO parameter space, however, remains an unresolved issue for further investigation.

Additional nonlinear issues can be inferred from the linear properties of the gyro-BWO. We have just argued

²²This is true for any magnetic field (see Chen *et al.*, 2002). For the gyromonotron, by comparison, the optimum transit angle for all orders of axial modes falls in the neighborhood of π [Eq. (78)]. Through magnetic-field tuning, any axial mode can be made to interact more strongly with the electron beam than the other axial modes.

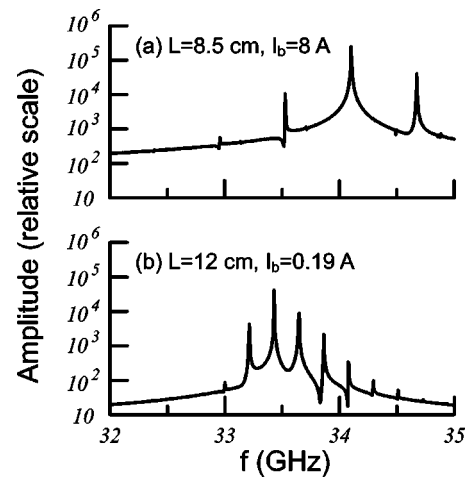


FIG. 53. Calculated output spectrum of a gyro-BWO at a beam current slightly above the onset current of the nonstationary state shown in Fig. 52: (a) $L=8.5$ cm, (b) $L=12$ cm. Other parameters are the same as in Fig. 28. From Chen *et al.*, 2002.

that, in a uniform interaction structure, the start-oscillation current always increases with the axial mode index (illustrated in Fig. 52). As a result, the fundamental axial mode will always appear first as the beam current rises. This suggests that excitation of higher-order axial modes is inherently a multimode effect. Dominance of a higher-order axial mode, if possible, will be the consequence of mode competition.

Furthermore, the large separation (by a factor of ~ 8 , see Fig. 52)²³ between the I_{st} of the fundamental and second axial modes implies a substantial buildup of the fundamental axial mode as the beam current continues to rise to the threshold of the second axial mode. Since the formation of axial modes depends entirely upon the beam-wave interaction, questions arise as to the accessibility and identities of higher-order axial modes defined on the basis of the single-mode theory, given the presence of a large-amplitude fundamental mode. In fact, the absence of mode competition at a current well above the threshold of several higher-order axial modes (Fig. 52) has already raised similar questions. The gyro-BWO offers the unique advantage of continuous frequency tunability. As is evident from the unresolved issues, it is also an intriguing electrodynamic system with nonlinear properties yet to be fully unraveled.

ACKNOWLEDGMENTS

The author is deeply indebted to Professor N. C. Luhmann, Jr., for his suggestions and critical comments throughout the course of writing this article. He is grateful to F. F. Chung for carrying out the calculations for

²³Perhaps for the same reason, the corresponding separation in a conventional BWO is by an even greater factor of 81 (Johnson, 1955; Chodorow and Susskind, 1964).

Figs. 7–11, and to Dr. T. H. Chang and Dr. G. Caryotakis for many helpful comments on the manuscript. This work was performed under the auspices of the National Science Council, Taiwan, and the S.S. Shu Chair of the National Tsing Hua University.

REFERENCES

- Alikaev, V. V., and E. V. Suvorov, 1994, "Electron-cyclotron resonance plasma heating and current drive in toroidal devices," in *Applications of High Power Microwaves*, edited by A. V. Gaponov-Grekhov and V. L. Granatstein (Artech House, Norwood, MA), pp. 111–144.
- Alonso, M., and E. J. Finn, 1970, *Physics* (Addison-Wesley, Reading, MA), p. 238.
- Andronov, A. A., V. A. Flyagin, A. V. Gaponov, A. L. Gol'denberg, M. I. Petelin, V. G. Usov, and V. K. Yulpatov, 1978, "The gyrotron: High-power source of millimeter and submillimeter waves," *Infrared Phys.* **18**, 385–393.
- Antakov, I. I., V. M. Bokov, R. P. Vasil'ev, and A. V. Gaponov, 1960, "Interaction of trochoidal electron beam with electromagnetic wave in a rectangular waveguide," *Izv. Vyssh. Uchebn. Zaved., Radiofiz.* **3**, 1033.
- Antakov, I. I., A. V. Gaponov, V. A. Ginzburg, A. L. Gol'denberg, M. I. Petelin, and V. K. Yulpatov, 1967, "An amplifier of electromagnetic oscillations in centimeter, millimeter, and submillimeter wavelength regions," *USSR Patent No. 302050*.
- Antakov, I. I., A. V. Gaponov, O. V. Malygin, and V. A. Flyagin, 1966, "Application of induced cyclotron radiation of electrons for the generation and amplification of high power electromagnetic waves," *Radio Eng. Electron. Phys.* **11**, 1195–1197.
- Antonsen, T. M., A. Fliflet, J. P. Calame, and B. Levush, 2001, "Collective theory of shot noise in gyrokystrons," *Phys. Plasmas* **8**, 4592–4607.
- Antonsen, T. M., W. M. Manheimer, and B. Levush, 1986, "Effect of ac and dc transverse self-fields in gyrotrons," *Int. J. Electron.* **61**, 823–854.
- Arfin, B., and A. K. Ganguly, 1982, "A three-cavity gyrokystron amplifier," *Int. J. Electron.* **53**, 709–714.
- Arman, M. J., 1998, "Plasma-filled gyro-BWO," *IEEE Trans. Plasma Sci.* **26**, 693–687.
- Baird, J. M., 1987, "Gyrotron theory," in *High Power Microwave Sources*, edited by V. L. Granatstein and I. Alexeff (Artech House, Norwood, MA), pp. 103–184.
- Baird, J. M., and W. Lawson, 1986, "Magnetron injection gun (MIG) design for gyrotron applications," *Int. J. Electron.* **61**, 953–967.
- Barnett, L. R., J. M. Baird, Y. Y. Lau, K. R. Chu, and V. L. Granatstein, 1980, "A high-gain single-stage gyrotron traveling-wave amplifier," in *Technical Digest International Electron Devices Meeting* (IEEE, New York), pp. 314–317.
- Barnett, L. R., L. H. Chang, H. Y. Chen, K. R. Chu, Y. K. Lau, and C. C. Tu, 1989, "Absolute instability competition and suppression in a millimeter-wave gyrotron traveling-wave tube," *Phys. Rev. Lett.* **63**, 1062–1065.
- Barnett, L. R., K. R. Chu, J. M. Baird, V. L. Granatstein, and A. T. Drobot, 1979, "Gain, saturation, and bandwidth measurements of the NRL gyrotron traveling wave amplifier," in *Technical Digest International Electron Devices Meeting* (IEEE, New York), pp. 164–167.
- Barnett, L. R., Y. Y. Lau, K. R. Chu, and V. L. Granatstein, 1981, "An experimental wideband gyrotron traveling-wave amplifier," *IEEE Trans. Electron Devices* **28**, 872–875.
- Basten, M. A., W. C. Guss, K. E. Kreischer, R. J. Temkin, and M. Caplan, 1995, "Experimental investigation of a 140-GHz gyrotron backward-wave oscillator," *Int. J. Infrared Millim. Waves* **16**, 889–905.
- Bateman, H., 1954, *Tables of Integral Transforms* (McGraw-Hill, New York), Vol. 2, p. 362.
- Bekefi, G., A. DiRienzo, C. Leibovitch, and B. G. Danly, 1989, "35-GHz cyclotron autoresonance maser amplifier," *Appl. Phys. Lett.* **54**, 1302–1304.
- Bezruchko, B. P., and S. P. Kuznetsov, 1978, "Experimental investigation of nonlinear nonstationary processes in a type O backward-wave tube oscillator," *Radiophys. Quantum Electron.* **21**, 739–744.
- Blank, M., P. Borchard, S. Cauffman, K. Felch, and Y. M. Mizuhara, 2002, "Design of a 50-MW 30-GHz gyrokystron amplifier for accelerator applications," in *Proceedings IEEE International Vacuum Electronics Conference* (IEEE, New York), pp. 85–86.
- Blank, M., K. Felch, B. G. James, P. Borchard, P. Cahalan, T. S. Chu, H. Jory, B. G. Danly, B. Levush, J. P. Calame, K. T. Nguyen, and D. E. Pershing, 2002, "Development and demonstration of high-average power W-band gyro-amplifiers for radar applications," *IEEE Trans. Plasma Sci.* **30**, 865–875.
- Blanken, R. A., T. H. Stix, and A. F. Kuckes, 1969, "Relativistic cyclotron instabilities," *Plasma Phys.* **11**, 946–960.
- Bollen, W. M., A. H. McCurdy, B. Arfin, R. K. Parker, and A. K. Ganguly, 1985, "Design and performance of a three-cavity gyrokystron amplifier," *IEEE Trans. Plasma Sci.* **13**, 417–423.
- Bondeson, A., and T. M. Antonsen, 1986, "Space-charge instabilities in gyrotron beams," *Int. J. Electron.* **61**, 855–870.
- Bott, I. B., 1964, "Tunable source of millimeter and submillimeter electromagnetic radiation," *Proc. IEEE* **52**, 330–331.
- Bott, I. B., 1965, "A powerful source of millimeter wavelength electromagnetic radiation," *Phys. Lett.* **14**, 293–294.
- Botton, M., T. M. Antonsen, B. Levush, K. T. Nguyen, and A. N. Vlasov, 1998, "MAGY: a time-dependent code for simulation of slow and fast microwave sources," *IEEE Trans. Plasma Sci.* **26**, 882–892.
- Brand, G. F., 1985, "Tunable gyrotrons," in *Infrared and Millimeter Waves*, edited by K. J. Button (Academic, New York), Vol. 14, pp. 371–408.
- Bratman, V. L., G. G. Denisov, B. D. Kol'chugin, S. V. Samsonov, and A. B. Volkov, 1995, "Experimental demonstration of high-efficiency cyclotron autoresonance maser operation," *Phys. Rev. Lett.* **75**, 3102–3105.
- Bratman, V. L., A. E. Fedotov, Y. K. Kalynov, V. N. Manuilov, M. M. Ofitserov, S. V. Samsonov, and A. V. Savilov, 1999, "Moderately relativistic high-harmonic gyrotrons for millimeter/submillimeter wavelength band," *IEEE Trans. Plasma Sci.* **27**, 456–461.
- Bratman, V. L., N. S. Ginzburg, G. S. Nusinovich, M. I. Petelin, and P. S. Strelkov, 1981, "Relativistic gyrotrons and cyclotron autoresonance masers," *Int. J. Electron.* **51**, 541–567.
- Bratman, V. L., A. W. Gross, G. G. Denisov, W. He, A. D. R. Phelps, K. Ronald, S. V. Samsonov, C. G. Whyte, and A. R. Young, 2000, "High-gain wideband gyrotron traveling-wave amplifier with a helically corrugated waveguide," *Phys. Rev. Lett.* **84**, 2746–2749.

- Briggs, R. J., 1964, *Electron-Stream Interaction with Plasmas* (MIT, Cambridge, MA).
- Bykov, Yu. V., and A. L. Gol'denberg, 1975, "Influence of resonator profile on the maximum power of a cyclotron resonance maser," *Radiophys. Quantum Electron.* **18**, 791–792.
- Bykov, Yu. V., A. L. Gol'denberg, L. V. Nikolaev, M. M. Ofitserov, and M. I. Petelin, 1975, "Experimental investigation of a gyrotron with whispering-gallery modes," *Radiophys. Quantum Electron.* **18**, 1141–1143.
- Bykov, Y. V., and V. E. Semenov, 1994, "Processing of material using microwave radiation," in *Applications of High Power Microwaves*, edited by A. V. Gaponov-Grekhov and V. L. Granatstein (Artech House, Norwood, MA), pp. 319–351.
- Calame, J. P., B. G. Danly, M. Garven, and B. Levush, 2000, "Studies of electronic noise in gyrokystrons," *Phys. Plasmas* **7**, 2180–2185.
- Caplan, M., A. T. Lin, and K. R. Chu, 1982, "A study of the saturated output of a TE₀₁ gyrotron using an electromagnetic finite-size particle code," *Int. J. Electron.* **53**, 659–671.
- Chang, T. H., L. R. Barnett, K. R. Chu, F. Tai, and C. L. Hsu, 1999, "A dual-function circular polarization converter for microwave/plasma processing systems," *Rev. Sci. Instrum.* **70**, 1530–1534.
- Chang, T. H., S. H. Chen, L. R. Barnett, and K. R. Chu, 2001, "Characterization of stationary and nonstationary behavior in gyrotron oscillators," *Phys. Rev. Lett.* **87**, 064802.
- Chang, T. H., K. F. Pao, S. H. Chen, and K. R. Chu, 2003, "Self-consistent effects on the starting current of gyrotron oscillators," *Int. J. Infrared Millim. Waves* **24**, 1415–1420.
- Charbit, P., A. Herscovici, and G. Mourier, 1981, "A partly self-consistent theory of the gyrotron," *Int. J. Electron.* **51**, 303–330.
- Chen, C., and J. S. Wurtele, 1991, "Linear and nonlinear theory of cyclotron autoresonance masers with multiple waveguide modes," *Phys. Fluids B* **3**, 2133–2148.
- Chen, K. R., 1993, "Fast ion driven Bernstein instabilities," *Phys. Lett. A* **181**, 308–314.
- Chen, K. R., 1994, "Anomalous thermalization of fast ions in magnetized plasma," *Phys. Rev. Lett.* **72**, 3534–3537.
- Chen, K. R., and K. R. Chu, 1986, "Study of a noise amplification mechanism in gyrotrons," *IEEE Trans. Microwave Theory Tech.* **34**, 72–79.
- Chen, S. H., T. H. Chang, K. F. Pao, C. T. Fan, and K. R. Chu, 2002, "Linear and time-dependent behavior of the gyrotron backward-wave oscillator," *Phys. Rev. Lett.* **89**, 268303.
- Chen, S. H., K. R. Chu, and T. H. Chang, 2000, "Saturated behavior of the gyrotron backward-wave oscillator," *Phys. Rev. Lett.* **85**, 2633–2636.
- Chodorow, M., and C. Susskind, 1964, *Fundamentals of Microwave Electronics* (McGraw-Hill, New York), p. 187.
- Choe, J. Y., and S. Ahn, 1981, "General mode analysis of a gyrotron dispersion relation," *IEEE Trans. Electron Devices* **28**, 94–102.
- Chow, K. K., and R. H. Pantell, 1960, "The cyclotron resonance backward-wave oscillator," *Proc. IRE* **48**, 1865–1870.
- Chu, K. R., 1978, "Theory of electron cyclotron maser interaction in a cavity at the harmonic frequencies," *Phys. Fluids* **21**, 2354–2364.
- Chu, K. R., 2002, "Overview of research on the gyrotron traveling-wave amplifier," *IEEE Trans. Plasma Sci.* **30**, 903–908.
- Chu, K. R., L. R. Barnett, H. Y. Chen, S. H. Chen, Ch. Wang, Y. S. Yeh, Y. C. Tsai, T. T. Yang, and T. Y. Dawn, 1995, "Stabilizing of absolute instabilities in gyrotron traveling-wave amplifier," *Phys. Rev. Lett.* **74**, 1103–1106.
- Chu, K. R., L. R. Barnett, W. K. Lau, L. H. Chang, and H. Y. Chen, 1990a, "A wideband millimeter-wave gyrotron traveling-wave amplifier experiment," *IEEE Trans. Electron Devices* **37**, 1557–1560.
- Chu, K. R., L. R. Barnett, W. K. Lau, L. H. Chang, and C. S. Kou, 1990b, "Recent development in millimeter wave gyro-TWT research at NTHU," in *Technical Digest International Electron Devices Meeting* (IEEE, New York), pp. 699–702.
- Chu, K. R., L. R. Barnett, W. K. Lau, L. H. Chang, A. T. Lin, and C. C. Lin, 1991, "Nonlinear dynamics of the gyrotron traveling-wave amplifier," *Phys. Fluids B* **3**, 2403–2408.
- Chu, K. R., H. Y. Chen, C. L. Hung, T. H. Chang, L. R. Barnett, S. H. Chen, and T. T. Yang, 1998, "Ultra-high-gain gyrotron traveling-wave amplifier," *Phys. Rev. Lett.* **81**, 4760–4763.
- Chu, K. R., H. Y. Chen, C. L. Hung, T. H. Chang, L. R. Barnett, S. H. Chen, T. T. Yang, and D. Dialetis, 1999, "Theory and experiment of ultra-high-gain gyrotron traveling-wave amplifier," *IEEE Trans. Plasma Sci.* **27**, 391–404.
- Chu, K. R., A. T. Drobot, V. L. Granatstein, and J. L. Seftor, 1979, "Characteristics and optimum operating parameters of a gyrotron traveling-wave amplifier," *IEEE Trans. Microwave Theory Tech.* **27**, 178–187.
- Chu, K. R., A. T. Drobot, H. H. Szu, and P. Sprangle, 1980, "Theory and simulation of the gyrotron traveling-wave amplifier operating at cyclotron harmonics," *IEEE Trans. Microwave Theory Tech.* **28**, 313–317.
- Chu, K. R., A. K. Ganguly, V. L. Granatstein, J. L. Hirshfield, S. Y. Park, and J. M. Baird, 1981, "Theory of a slow wave cyclotron amplifier," *Int. J. Electron.* **51**, 493–502.
- Chu, K. R., V. L. Granatstein, P. E. Latham, W. Lawson, and C. D. Striffler, 1985, "A 30-MW gyrokystron amplifier design for high-energy linear accelerators," *IEEE Trans. Plasma Sci.* **13**, 424–434.
- Chu, K. R., H. Guo, and V. L. Granatstein, 1997, "Theory of the harmonic multiplying gyrotron traveling-wave amplifier," *Phys. Rev. Lett.* **78**, 4661–4664.
- Chu, K. R., and J. L. Hirshfield, 1978, "Comparative study of the axial and azimuthal bunching mechanisms in electromagnetic cyclotron instabilities," *Phys. Fluids* **21**, 461–466.
- Chu, K. R., P. E. Latham, and V. L. Granatstein, 1988, "Penultimate cavity tuning of the gyrokystron amplifier," *Int. J. Electron.* **65**, 419–428.
- Chu, K. R., Y. Y. Lau, L. R. Barnett, and V. L. Granatstein, 1981, "Theory of a wideband distributed gyrotron traveling-wave amplifier," *IEEE Trans. Electron Devices* **28**, 866–871.
- Chu, K. R., and A. T. Lin, 1988, "Gain and bandwidth of the gyro-TWT and CARM amplifier," *IEEE Trans. Plasma Sci.* **16**, 90–104.
- Chu, K. R., and L. H. Lyu, 1986, "Simulation of electrostatic noise amplification in gyrotrons," *IEEE Trans. Microwave Theory Tech.* **34**, 690–695.
- Chu, K. R., M. E. Read, and A. K. Ganguly, 1980, "Methods of efficiency enhancement and scaling for the gyrotron oscillator," *IEEE Trans. Microwave Theory Tech.* **28**, 318–325.
- Chu, K. R., P. A. Sprangle, and V. L. Granatstein, 1982, "Slow-wave wideband cyclotron amplifier," U.S. Patent No. 4362968.
- Danly, B. G., M. Blank, J. P. Calame, B. Levush, K. T. Nguyen, D. E. Pershing, R. K. Parker, K. L. Felch, B. G. James, P. Borchard, P. Cahalan, T. S. Chu, H. R. Jory, T. A. Hargreaves,

- R. B. True, W. G. Lawson, and T. M. Antenson, 2000, "Development and testing of a high-average-power 94-GHz gyrokystron," *IEEE Trans. Plasma Sci.* **28**, 713–726.
- Davies, J. A., 1989, "Conditions for absolute instability in the cyclotron resonance maser," *Phys. Fluids B* **1**, 663–669.
- Denisov, G. G., V. L. Bratman, A. W. Gross, W. He, A. D. R. Phelps, K. Ronald, S. V. Samsonov, and C. G. Whyte, 1998, "Gyrotron traveling-wave amplifier with a helical interaction waveguide," *Phys. Rev. Lett.* **81**, 5680–5683.
- Denisov, G. G., V. L. Bratman, A. D. R. Phelps, and S. V. Samsonov, 1998, "Gyro-TWT with a helical operating waveguide: New possibilities to enhance efficiency and frequency bandwidth," *IEEE Trans. Plasma Sci.* **26**, 508–518.
- Dickerson, W. L., and C. C. Johnson, 1964, "A ten kilomegacycle amplifier utilizing the interaction between a periodic electron beam and an unloaded waveguide mode," University of Utah Technical Report No. ASD-2.
- DiRienzo, A. C., G. Bekefi, C. Chen, and J. S. Wurtele, 1991, "Experimental and theoretical studies of a 35-GHz cyclotron autoresonance maser amplifier," *Phys. Fluids B* **3**, 1755–1765.
- Dmitriev, A. Y., D. I. Trubetsko, and A. P. Chtverikov, 1991, "Transient processes in the interaction of a helical electron beam with an oppositely traveling wave in a waveguide," *Radiophys. Quantum Electron.* **34**, 502–507.
- Edgcombe, C. J., 1980, "The dispersion equation for the gyrotron amplifier," *Int. J. Electron.* **48**, 471–486.
- Edgcombe, C. J., 1993, Ed., *Gyrotron Oscillators—Their Principles and Practices* (Taylor and Francis, London).
- Fekete, P. W., G. F. Brand, and T. Idehara, 1994, "Scattering from discrete Alfvén waves in a tokamak using a gyrotron radiation source," *Plasma Phys. Controlled Fusion* **36**, 1407–1417.
- Felch, K. L., B. G. Danly, H. R. Jory, K. E. Kreischer, W. Lawson, B. Levush, and R. J. Temkin, 1999, "Characteristics and applications of fast-wave gyrodevices," *Proc. IEEE* **87**, 752–781.
- Ferguson, P. E., and R. S. Symons, 1980, "A C-band gyro-TWT," in *Technical Digest International Electron Devices Meeting* (IEEE, New York), pp. 310–313.
- Ferguson, P. E., G. Valier, and R. S. Symons, 1981, "Gyrotron-TWT operating characteristics," *IEEE Trans. Microwave Theory Tech.* **29**, 794–799.
- Fliflet, A. W., 1986, "Linear and nonlinear theory of the Doppler-shifted cyclotron resonance maser based on TE and TM waveguide modes," *Int. J. Electron.* **61**, 1049–1080.
- Flyagin, V. A., A. V. Gaponov, M. I. Petelin, and V. K. Yulpatov, 1977, "The gyrotron," *IEEE Trans. Microwave Theory Tech.* **25**, 514–521.
- Flyagin, V. A., and G. S. Nusinovich, 1988, "Gyrotron oscillators," *Proc. IEEE* **76**, 644–656.
- Forman, P., 1995, "Swords into ploughshares: Breaking new ground with radar hardware and techniques in physical research after World War II," *Rev. Mod. Phys.* **67**, 397–455.
- Freund, H. P., and C. S. Wu, 1976, "Excitation of the ordinary electromagnetic mode in low- β plasmas," *Phys. Fluids* **19**, 299–304.
- Freund, H. P., and C. S. Wu, 1977, "Induced gyroresonant emission of extraordinary mode radiation," *Phys. Fluids* **20**, 619–627.
- Friedman, M., D. A. Hammer, W. M. Manheimer, and P. Sprangle, 1973, "Enhanced microwave emission due to the transverse energy of an intense relativistic electron beam," *Phys. Rev. Lett.* **31**, 752–755.
- Furuno, D. S., D. B. McDermott, C. S. Kou, N. C. Luhmann, Jr., and P. Vitello, 1989, "Theoretical and experimental investigation of a high-harmonic gyro-traveling-wave-tube amplifier," *Phys. Rev. Lett.* **62**, 1314–1317.
- Ganguly, A. K., and S. Ahn, 1982, "Self-consistent large signal theory of the gyrotron traveling-wave amplifier," *Int. J. Electron.* **53**, 641–658.
- Ganguly, A. K., and S. Ahn, 1984, "Large-signal theory of a two-stage wideband gyro-TWT," *IEEE Trans. Electron Devices* **31**, 474–480.
- Ganguly, A. K., and S. Ahn, 1989, "Nonlinear analysis of gyro-BWO in three dimensions," *Int. J. Electron.* **67**, 261–276.
- Ganguly, A. K., and K. R. Chu, 1981, "Analysis of two-cavity gyrokystron," *Int. J. Electron.* **51**, 503–520.
- Gaponov, A. V., 1959a, "Interaction between electron fluxes and electromagnetic waves in waveguides," *Izv. Vyssh. Uchebn. Zaved., Radiofiz.* **2**, 450–462.
- Gaponov, A. V., 1959b, "Letter to the editor," *Izv. Vyssh. Uchebn. Zaved., Radiofiz.* **2**, 836–837.
- Gaponov, A. V., A. L. Gol'denberg, D. P. Grigor'ev, I. M. Orlova, T. P. Pankratova, and M. I. Petelin, 1965, "Induced synchrotron radiation of electrons in cavity resonators," *JETP Lett.* **2**, 267–269.
- Gaponov, A. V., A. L. Gol'denberg, M. I. Petelin, and V. K. Yulpatov, 1967, "A device for centimeter, millimeter, and submillimeter wave generation," *USSR Patent No.* 223931.
- Gaponov, A. V., M. I. Petelin, and V. K. Yulpatov, 1967, "The induced radiation of excited classical oscillators and its use in high-frequency electronics," *Radiophys. Quantum Electron.* **10**, 794–813.
- Gaponov, A. V., and V. K. Yulpatov, 1967, "Interaction of helical electron beams with the electromagnetic field in a waveguide," *Radio Eng. Electron. Phys.* **12**, 582–587.
- Gaponov-Grekhov, A. V., and V. L. Granatstein, 1994, Eds., *Applications of High Power Microwaves* (Artech House, Norwood, MA).
- Garven, M., J. P. Calame, B. G. Danly, K. T. Nguyen, B. Levush, F. N. Wood, and D. E. Pershing, 2002, "A gyrotron traveling wave tube amplifier experiment with a ceramic loaded interaction region," *IEEE Trans. Plasma Sci.* **30**, 885–893.
- Gewartowski, J. W., and H. A. Watson, 1965, *Principles of Electron Tubes* (Van Nostrand, Princeton, NJ).
- Gilmour, A. S., Jr., 1986, *Microwave Tubes* (Artech House, Norwood, MA).
- Ginzburg, N. S., S. P. Kuznetsov, and T. N. Fedoseeva, 1978, "Theory of transients in relativistic backward-wave tubes," *Radiophys. Quantum Electron.* **21**, 728–744.
- Ginzburg, N. S., G. S. Nusinovich, and N. A. Zavolsky, 1986, "Theory of nonstationary processes in gyrotrons with low Q resonators," *Int. J. Electron.* **61**, 881–894.
- Ginzburg, N. S., N. S. Zarnitsyna, and G. S. Nusinovich, 1981, "Theory of relativistic cyclotron resonance maser amplifiers," *Radiophys. Quantum Electron.* **24**, 331–338.
- Gold, S. H., D. A. Kirkpatrick, A. W. Fliflet, R. B. McCowan, A. K. Kinkead, D. L. Hardesty, and M. Sucey, 1991, "High-voltage millimeter-wave gyro-traveling-wave amplifier," *J. Appl. Phys.* **69**, 6696–6698.
- Gold, S. H., and G. S. Nusinovich, 1997, "Review of high-power microwave source research," *Rev. Sci. Instrum.* **68**, 3945–3974.

- Gol'denberg, A. L., and A. G. Litvak, 1995, "Recent progress of high-power millimeter wavelength gyrodevices," *Phys. Plasmas* **2**, 2562–2572.
- Granatstein, V. L., and W. Lawson, 1996, "Gyro-amplifiers as candidate rf drivers for TeV linear colliders," *IEEE Trans. Plasma Sci.* **24**, 648–665.
- Granatstein, V. L., B. Levush, B. G. Danly, and R. K. Parker, 1997, "A quarter century of gyrotron research and development," *IEEE Trans. Plasma Sci.* **25**, 1322–1335.
- Granatstein, V. L., G. S. Nusinovich, M. Blank, K. Felch, R. M. Gilgenbach, H. Guo, H. Jory, N. C. Luhmann, D. B. McDermott, J. M. Rogers, and T. A. Spencer, 2001, "Gyrotron oscillators and amplifiers," in *High-Power Microwave Sources and Technologies*, edited by R. J. Barker and E. Schamiloglu (IEEE, New York), pp. 156–198.
- Granatstein, V. L., R. K. Parker, and C. M. Armstrong, 1999, "Vacuum electronics at the dawn of the twenty-first century," *Proc. IEEE* **87**, 702–716.
- Granatstein, V. L., M. Read, and L. R. Barnett, 1984, "Measured performance of gyrotron oscillators and amplifiers," in *Infrared and Millimeter Waves*, edited by K. J. Button (Academic, New York), Vol. 5, pp. 267–304.
- Granatstein, V. L., P. S. Sprangle, A. T. Drobot, K. R. Chu, and J. L. Seftor, 1980, "Gyrotron traveling wave amplifier," U.S. Patent No. 4224576.
- Granatstein, V. L., P. Sprangle, M. Herndon, R. K. Parker, and S. P. Schlesinger, 1975, "Microwave amplification with an intense relativistic electron beam," *J. Appl. Phys.* **46**, 3800–3805.
- Grudiev, A., and K. Schunemann, 2002, "Nonstationary behavior of the gyrotron backward-wave oscillator," *IEEE Trans. Plasma Sci.* **30**, 851–858.
- Guo, H., L. Chen, H. Keren, J. L. Hirshfield, S. Y. Park, and K. R. Chu, 1982, "Measurement of gain for slow cyclotron waves on an annular electron beam," *Phys. Rev. Lett.* **49**, 730–733.
- Guo, H., S. H. Chen, V. L. Granatstein, J. Rogers, G. S. Nusinovich, M. Waters, B. Levush, and W. J. Chen, 1997, "Operation of a highly overmoded harmonic-multiplying wideband gyrotron amplifier," *Phys. Rev. Lett.* **79**, 515–518.
- Hirshfield, J. L., 1981, "Cyclotron harmonic maser," *Int. J. Infrared Millim. Waves* **2**, 695–703.
- Hirshfield, J. L., I. B. Bernstein, and J. M. Wachtel, 1965, "Cyclotron resonance interactions of microwaves with energetic electrons," *IEEE J. Quantum Electron.* **1**, 237–245.
- Hirshfield, J. L., and V. L. Granatstein, 1977, "The electron cyclotron maser—An history survey," *IEEE Trans. Microwave Theory Tech.* **25**, 522–527.
- Hirshfield, J. L., and J. M. Wachtel, 1964, "Electron cyclotron maser," *Phys. Rev. Lett.* **12**, 533–536.
- Hsu, T. W., and P. N. Robson, 1965, "Negative absorption from weakly relativistic electrons traversing a Cuccia coupler," *Electron. Lett.* **1**, 84–85.
- Idehara, T., I. Ogawa, S. Mitsudo, M. Pereyaslavets, N. Nishida, and K. Yoshida, 1999, "Development of frequency tunable, medium power gyrotrons (gyrotron FU series) as submillimeter wave radiation sources," *IEEE Trans. Plasma Sci.* **27**, 340–354.
- Johnson, H. R., 1955, "Backward-wave oscillators," *Proc. IRE* **43**, 684–697.
- Jory, H. R., F. Friedlander, S. J. Hegji, J. R. Shively, and S. Symons, 1977, "Gyrotrons for high-power millimeter wave generation," in *Technical Digest International Electron Devices Meeting* (IEEE, New York), pp. 234–237.
- Jory, H. R., and A. W. Trivelpiece, 1968, "Charged-particle motion in large-amplitude electromagnetic fields," *J. Appl. Phys.* **39**, 3053–3060.
- Kamada, K., K. Nawashiro, F. Tamagawa, H. Igarashi, S. Kizu, C. Y. Lee, S. Kawasaki, R. Ando, and M. Masuzaki, 1998, "Gyrotron backward wave oscillator experiments with a relativistic electron beam using an X-band rectangular waveguide," *Int. J. Infrared Millim. Waves* **19**, 1317–1324.
- Kisel', D. V., G. S. Korablev, V. G. Navel'Yev, M. I. Petelin, and Sh. Ye. Tsimring, 1974, "An experimental study of a gyrotron operating at the second harmonic of the cyclotron frequency with optimized distribution of the high-frequency field," *Radio Eng. Electron. Phys.* **19**, 95–100.
- Kou, C. S., 1994, "Starting oscillation conditions for gyrotron backward wave oscillators," *Phys. Plasmas* **1**, 3093–3099.
- Kou, C. S., 1995, "On the launching loss and the Weibel instability of the gyrotron traveling-wave tube," *Phys. Plasmas* **2**, 578–585.
- Kou, C. S., S. H. Chen, L. R. Barnett, H. Y. Chen, and K. R. Chu, 1993, "Experimental study of an injection-locked gyrotron backward-wave oscillator," *Phys. Rev. Lett.* **70**, 924–927.
- Kou, C. S., C. H. Chen, and T. J. Wu, 1998, "Mechanism of efficiency enhancement by a tapered waveguide in gyrotron backward-wave oscillators," *Phys. Rev. E* **57**, 7162–7168.
- Kou, C. S., Q. S. Wang, D. B. McDermott, A. T. Lin, K. R. Chu, and N. C. Luhmann, Jr., 1992, "High-power harmonic gyro-TWT. Part I: Linear theory and oscillation study," *IEEE Trans. Plasma Sci.* **20**, 155–162.
- Krall, N. A., and A. W. Trivelpiece, 1973, *Principles of Plasma Physics* (McGraw-Hill, New York), Chap. 8.
- Kreischer, K. E., and R. J. Temkin, 1987, "Single-mode operation of a high-power, step-tunable gyrotron," *Phys. Rev. Lett.* **59**, 547–550.
- Kuraev, A. A., S. V. Kolosov, A. F. Stekolnikov, G. Ya. Slepyan, and A. Ya. Slepyan, 1988, "TWT-gyrotrons: nonlinear theory, optimization, and analysis," *Int. J. Electron.* **65**, 437–462.
- Lau, Y. Y., 1982, "Simple macroscopic theory of cyclotron maser instabilities," *IEEE Trans. Electron Devices* **29**, 320–335.
- Lau, Y. Y., and K. R. Chu, 1981, "Gyrotron traveling wave amplifier. III. A proposed wideband fast wave amplifier," *Int. J. Infrared Millim. Waves* **2**, 415–425.
- Lau, Y. Y., and K. R. Chu, 1983, "Electron cyclotron maser instability driven by loss cone distribution," *Phys. Rev. Lett.* **50**, 243–246.
- Lau, Y. Y., K. R. Chu, L. R. Barnett, and V. L. Granatstein, 1981a, "Gyrotron traveling-wave amplifier. I. Analysis of oscillations," *Int. J. Infrared Millim. Waves* **2**, 373–393.
- Lau, Y. Y., K. R. Chu, L. R. Barnett, and V. L. Granatstein, 1981b, "Gyrotron traveling-wave amplifier. II. Effects of velocity spread and wall resistivity," *Int. J. Infrared Millim. Waves* **2**, 395–413.
- Lawson, W., J. P. Calame, B. Hogan, P. E. Latham, M. E. Read, V. L. Granatstein, and M. Reiser, 1991, "Efficient operation of a high-power X-band gyrokystron," *Phys. Rev. Lett.* **67**, 520–523.
- Lawson, W., J. Cheng, J. P. Calame, M. Castle, B. Hogan, V. L. Granatstein, M. Reiser, and G. P. Saraph, 1998, "High-power operation of a three-cavity X-band coaxial gyrokystron," *Phys. Rev. Lett.* **81**, 3030–3033.
- Lawson, W., H. W. Matthews, M. K. E. Lee, J. P. Calame, B. Hogan, J. Cheng, P. E. Latham, V. L. Granatstein, and M.

- Reiser, 1993, "High-power operation of a K-band second-harmonic gyrokystron," *Phys. Rev. Lett.* **71**, 456–459.
- Levush, B., T. M. Antonsen, A. Bromborsky, W. R. Lou, and Y. Carmel, 1992, "Theory of relativistic backward-wave oscillator with end reflections," *IEEE Trans. Plasma Sci.* **20**, 263–280.
- Lin, A. T., 1984, "Doppler shift dominated cyclotron masers," *Int. J. Electron.* **57**, 1097–1107.
- Lin, A. T., 1992, "Mechanism for efficiency enhancement in gyrotron backward-wave oscillators with tapered magnetic fields," *Phys. Rev. A* **46**, R4516–R4519.
- Lin, A. T., K. R. Chu, and A. Bromborsky, 1987, "Stability and tunability of a CARM amplifier," *IEEE Trans. Electron Devices* **34**, 2621–2624.
- Lin, A. T., K. R. Chu, C. C. Lin, C. S. Kou, D. B. McDermott, and N. C. Luhmann, Jr., 1992, "Marginal stability design criterion for gyro-TWTs and comparison of fundamental with second harmonic operation," *Int. J. Electron.* **72**, 873–885.
- Lin, A. T., and P. K. Kaw, 1992, "Absolute instability in finite-length electron cyclotron maser systems," *Int. J. Electron.* **72**, 887–894.
- Lin, A. T., Z. H. Yang, and K. R. Chu, 1988, "Particle simulation of a high-power gyrotron oscillator," *IEEE Trans. Plasma Sci.* **16**, 129–134.
- Lin, C. C., and A. T. Lin, 1998, "A new algorithm for solving Maxwell's equation in high-power microwave device simulations," *IEEE Trans. Plasma Sci.* **26**, 893–900.
- Lindsay, P. A., 1972, "Cyclotron resonance interaction," *Int. J. Electron.* **33**, 289–310.
- Lindsay, P. A., 1981, "Self-consistent large-signal interaction in a TWT gyrotron," *Int. J. Electron.* **51**, 379–393.
- Lindsay, P. A., R. M. Jones, and R. J. Lumsden, 1984, "Some observations on gyrotron interaction models," *Int. J. Electron.* **57**, 915–951.
- Lindsay, P. A., R. J. Lumsden, and R. M. Jones, 1982, "A dispersion relation for gyrotron TWTs," *Int. J. Electron.* **53**, 619–640.
- Link, G., L. Feher, M. Thumm, H. J. Ritzhaupt-Kleissl, R. Bohme, and A. Weisenburger, 1999, "Sintering of advanced ceramics using a 30-GHz, 10-kW, CW industrial gyrotron," *IEEE Trans. Plasma Sci.* **27**, 547–554.
- Liu, S., and Z. Yang, 1981, "The kinetic theory of the electron cyclotron maser with space charge effect," *Int. J. Electron.* **51**, 341–349.
- Luce, T. C., 2002, "Applications of high-power millimeter waves in fusion energy research," *IEEE Trans. Plasma Sci.* **30**, 734–754.
- Luhmann, N. C., Jr., G. S. Nusinovich, and D. M. Goebel, 2004, "Historical highlights, applications and trends," in *Modern Microwave and Millimeter-Wave Power Electronics*, edited by R. J. Barker, N. C. Luhmann, Jr., J. H. Booske, and G. S. Nusinovich (IEEE, New York, in press), Chap. 2.
- Manheimer, W. M., 2001, "Uniform plasma model of shot noise in gyrokystrons," *IEEE Trans. Plasma Sci.* **29**, 639–648.
- Manheimer, W. M., G. Mesyats, and M. I. Petelin, 1994, "Applications of high-power microwave sources to enhanced radar systems," in *Applications of High Power Microwaves*, edited by A. V. Gaponov-Grekhov and V. L. Granatstein (Artech House, Norwood, MA), pp. 169–208.
- McDermott, D. B., D. S. Furuno, and N. C. Luhmann, Jr., 1985, "Production of relativistic rotating electron beams by gyroresonant rf acceleration in a TE_{11} cavity," *J. Appl. Phys.* **58**, 4501–4508.
- McDermott, D. B., H. H. Song, Y. Hirata, A. T. Lin, T. H. Chang, H. L. Hsu, P. S. Marandos, J. S. Lee, K. R. Chu, and N. C. Luhmann, Jr., 2002, "Design of a W-band TE_{01} mode gyrotron traveling-wave amplifier with high power and broadband capabilities," *IEEE Trans. Plasma Sci.* **30**, 894–902.
- Mourier, G., 1980, "Gyrotron tubes—A theoretical study," *Arch. Elektr. Uebertrag.* **34**, 473–484.
- Ngo, M., B. G. Danly, R. Myers, D. E. Pershing, V. Gregers-Hansen, and G. Lind, 2002, "High-power millimeter-wave transmitter for the NRL WARLOC radar," in *Proceedings IEEE International Vacuum Electronics Conference* (IEEE, New York), pp. 363–364.
- Nusinovich, G. S., 1999, "Review of the theory of mode interaction in gyrodevices," *IEEE Trans. Plasma Sci.* **27**, 313–326.
- Nusinovich, G. S., and O. Dumbrajs, 1996, "Theory of gyro-backward-wave oscillators with tapered magnetic field and waveguide cross section," *IEEE Trans. Plasma Sci.* **24**, 620–629.
- Nusinovich, G. S., A. N. Vlasov, and T. M. Antonsen, Jr., 2001, "Nonstationary phenomena in tapered gyro-backward-wave oscillators," *Phys. Rev. Lett.* **87**, 218301.
- Nusinovich, G. S., and Zapevalov, 1985, "Self-modulation instability of gyrotron radiation," *Radio Eng. Electron. Phys.* **30**, 101–108.
- Ott, E., and W. M. Manheimer, 1975, "Theory of microwave emission by velocity-space instabilities of an intense relativistic electron beam," *IEEE Trans. Plasma Sci.* **3**, 1–5.
- Pantell, R. H., 1959, "Backward-wave oscillations in an unloaded waveguide," *Proc. IRE* **47**, 1146.
- Park, G. S., J. J. Choi, S. Y. Park, C. M. Armstrong, A. K. Ganguly, R. H. Kyser, and R. K. Parker, 1995, "Gain broadening of two-stage tapered gyrotron traveling-wave amplifier," *Phys. Rev. Lett.* **74**, 2399–2402.
- Park, G. S., S. Y. Park, R. H. Kyser, C. M. Armstrong, A. K. Ganguly, and R. K. Parker, 1994, "Broadband operation of a Ka -band tapered gyro-traveling-wave amplifier," *IEEE Trans. Plasma Sci.* **22**, 536–543.
- Park, G. S., S. Y. Park, R. H. Kyser, A. K. Ganguly, and C. M. Armstrong, 1991, "Gain broadening in an inhomogeneous gyrotron traveling wave amplifier," in *Technical Digest International Electron Devices Meeting* (IEEE, New York), pp. 779–781.
- Park, S. Y., V. L. Granatstein, and R. K. Parker, 1984, "A linear theory and design study for a gyrotron backward-wave oscillator," *Int. J. Electron.* **57**, 1109–1123.
- Park, S. Y., R. H. Kyser, C. M. Armstrong, R. K. Parker, and V. L. Granatstein, 1990, "Experimental study of a Ka -band gyrotron backward-wave oscillator," *IEEE Trans. Plasma Sci.* **18**, 321–324.
- Pershing, D. E., K. T. Nguyen, J. P. Calame, B. G. Danley, and B. Levush, 2002, "Implementation of a TE_{11} Ka -band gyro-TWT amplifier with distributed loss," in *Conference Digest of the Twenty-Seventh International Conference on Infrared and Millimeter Waves*, edited by R. J. Temkin (IEEE, New York), pp. 199–201.
- Petelin, M. I., 1974, "On the theory of ultrarelativistic cyclotron self-resonance masers," *Radiophys. Quantum Electron.* **17**, 686–690.
- Petelin, M. I., 1999, "One century of cyclotron radiation," *IEEE Trans. Plasma Sci.* **27**, 294–302.
- Phillips, R. M., and D. W. Sprehn, 1999, "High-power klystrons for the next linear collider," *Proc. IEEE* **87**, 738–751.

- Piosczyk, B., A. Arnold, G. Dammertz, O. Dumbrajs, M. Kuntze, and M. K. Thumm, 2002, "Coaxial cavity gyrotron—Recent experimental results," *IEEE Trans. Plasma Sci.* **30**, 819–827.
- Read, M. E., K. R. Chu, and A. J. Dudas, 1982, "Experimental examination of the enhancement of gyrotron efficiencies by use of profiled magnetic fields," *IEEE Trans. Microwave Theory Tech.* **30**, 42–46.
- Rodgers, J., H. Guo, G. S. Nusinovich, and V. L. Granatstein, 2001, "Experimental study of phase deviation and pushing in a frequency doubling second harmonic gyro-amplifier," *IEEE Trans. Electron Devices* **48**, 2434–2441.
- Schmidt, G., 1979, *Physics of High Temperature Plasmas*, 2nd ed. (Academic, New York), p. 257, Eq. (8-109).
- Schneider, J., 1959, "Stimulated emission of radiation by relativistic electrons in a magnetic field," *Phys. Rev. Lett.* **2**, 504–505.
- Schriever, R. L., and C. C. Johnson, 1966, "A rotating beam waveguide oscillator," *Proc. IEEE* **54**, 2029–2030.
- Seftor, J. L., V. L. Granatstein, K. R. Chu, P. Sprangle, and M. E. Read, 1979, "The electron cyclotron maser as a high power traveling-wave amplifier of millimeter waves," *IEEE J. Quantum Electron.* **15**, 848–853.
- Sehn, G. J., and R. E. Hayes, 1969, "Relativistic effect in electron cyclotron transverse wave devices," *IEEE Trans. Electron Devices* **16**, 1077–1078.
- Sirigiri, J. R., M. A. Shapiro, and R. J. Temkin, 2003, "High-power 140-GHz quasi-optical gyrotron traveling-wave amplifier," *Phys. Rev. Lett.* **90**, 258302.
- Skolnik, M., 2002, "Role of radar in microwaves," *IEEE Trans. Microwave Theory Tech.* **50**, 625–632.
- Slater, J. C., 1950, *Microwave Electronics* (Van Nostrand, Princeton, NJ).
- Spencer, T. A., C. E. Davis, K. J. Hendricks, F. J. Agee, and R. M. Gilgenbach, 1996, "Results from gyrotron backward wave oscillator experiments utilizing a high-current high-voltage annular electron beam," *IEEE Trans. Plasma Sci.* **24**, 630–635.
- Sprangle, P., and A. Drobot, 1977, "The linear and self-consistent nonlinear theory of the electron cyclotron maser instability," *IEEE Trans. Microwave Theory Tech.* **25**, 528–544.
- Sprangle, P., and W. M. Manheimer, 1975, "Coherent nonlinear theory of a cyclotron instability," *Phys. Fluids* **18**, 224–230.
- Stix, T. W., 1992, *Waves in Plasmas* (AIP, New York).
- Sturrock, P. A., 1958, "Kinematics of growing waves," *Phys. Rev.* **112**, 1488–1503.
- Symons, R. S., and H. R. Jory, 1981, "Cyclotron resonance devices," in *Advances in Electronics and Electron Physics*, edited by L. Marton and C. Marton (Academic, New York), Vol. 55, pp. 1–75.
- Symons, R. S., H. R. Jory, and S. J. Hegji, 1979, "An experimental gyro-TWT," in *Technical Digest International Electron Devices Meeting* (IEEE, New York), pp. 676–679.
- Symons, R. S., H. R. Jory, S. J. Hegji, and P. E. Ferguson, 1981, "An experimental gyro-TWT," *IEEE Trans. Microwave Theory Tech.* **29**, 181–184.
- Thumm, M. K., and W. Kasperek, 2002, "Passive high-power microwave components," *IEEE Trans. Plasma Sci.* **30**, 755–786.
- Timms, G. P., and G. F. Brand, 1996, "Millimeter-wave measurements of phase transitions in thiourea using a gyrotron," *Appl. Phys. Lett.* **68**, 2899–2901.
- Tolkachev, A. A., B. A. Levitan, G. K. Solovjev, V. V. Veytsel, and V. E. Farber, 2000, "A megawatt power millimeter-wave phased-array radar," *IEEE Aerosp. Electron. Syst. Mag.* **15** (7), 25–31.
- Twiss, R. Q., 1958, "Radiation transfer and the possibility of negative absorption in radio astronomy," *Aust. J. Phys.* **11**, 564–579.
- Vlasov, S. N., G. M. Zhislin, I. M. Orlova, M. I. Petelin, and G. G. Rogacheva, 1969, "Irregular wave guide as open resonator," *Radiophys. Quantum Electron.* **12**, 972–978.
- Wachtel, J. M., and E. J. Wachtel, 1980, "Backward-wave oscillation in gyrotron," *Appl. Phys. Lett.* **37**, 1059–1061.
- Wang, Ch., Y. S. Yeh, T. T. Yang, H. Y. Chen, S. H. Chen, Y. C. Tsai, L. R. Barnett, and K. R. Chu, 1997, "A mechanically tunable magnetron injection gun," *Rev. Sci. Instrum.* **68**, 3031–3035.
- Wang, Q. S., C. S. Kou, D. B. McDermott, A. T. Lin, K. R. Chu, and N. C. Luhmann, Jr., 1992, "High-power harmonic gyro-TWTs—Part II: Nonlinear theory and design," *IEEE Trans. Plasma Sci.* **20**, 163–169.
- Wang, Q. S., D. B. McDermott, and N. C. Luhmann, Jr., 1995, "Demonstration of marginal stability theory by a 200-kW second-harmonic gyro-TWT amplifier," *Phys. Rev. Lett.* **75**, 4322–4325.
- Wang, Q. S., D. B. McDermott, and N. C. Luhmann, Jr., 1996, "Operation of a stable 200-kW second-harmonic gyro-TWT amplifier," *IEEE Trans. Plasma Sci.* **24**, 700–706.
- Walter, M. T., R. M. Gilgenbach, J. W. Luginsland, J. M. Hochman, J. I. Rintamaki, R. L. Jaynes, Y. Y. Lau, and T. A. Spencer, 1996, "Effects of tapering on gyrotron backward wave oscillators," *IEEE Trans. Plasma Sci.* **24**, 636–647.
- Weibel, E. S., 1959, "Spontaneous growing transverse waves in a plasma due to an anisotropic velocity distribution," *Phys. Rev. Lett.* **2**, 83–84.
- Wu, C. S., and L. C. Lee, 1979, "A theory of the terrestrial kilometric radiation," *Astrophys. J.* **230**, 621–626.
- Yovchev, I. G., W. G. Lawson, G. S. Nusinovich, V. L. Granatstein, and M. Castle, 2000, "Present status of a 17.1-GHz four-cavity frequency-doubling coaxial gyrokystron design," *IEEE Trans. Plasma Sci.* **28**, 523–528.
- Zaytsev, N. I., T. B. Pankratova, M. I. Petelin, and V. A. Flyagin, 1974, "Millimeter- and submillimeter-wave gyrotrons," *Radio Eng. Electron. Phys.* **21**, 103–107.
- Zhao, J., G. S. Nusinovich, H. Guo, J. C. Rogers, and V. L. Granatstein, 2000, "Axial mode locking in a harmonic-multiplying inverted gyrotwystron," *IEEE Trans. Plasma Sci.* **28**, 597–605.